INFLOW ANALYSIS FOR MULTI-ROTORS AND THE IMPACT ON SENSOR PLACEMENT

By

JAMES BRENNER

Bachelor of Science in Mechanical Engineering
Oklahoma State University
Stillwater, Oklahoma
2019

Bachelor of Science in Aerospace Engineering
Oklahoma State University
Stillwater, Oklahoma
2019

Submitted to the Faculty of the
Graduate College of the
Oklahoma State University
in partial fulfillment of
the requirements for
the Degree of
MASTER OF SCIENCE
July, 2021

INFLOW ANALYSIS FOR MULTI-ROTORS AND THE IMPACT ON SENSOR PLACEMENT

Thesis Approved:

Dr. Jamey D. Jacob

Thesis Advisor

Dr. He Bai

Dr. Brain R. Elbing

ACKNOWLEDGMENTS

I would like to thank the following people for their help and support throughout the thesis process. First, I would like to thank Andrew Quinton for helping me navigate PIV experiments in the water tunnel. I'd also like to thank Kyle Hickman, my research partner and fellow "Wind Boi" for the last two years, for the countless hours spent flight testing the wind sensors and aircraft together. It was a great experience to work together on our papers. Their knowledge and willingness to help were greatly appreciated. Next, I would like to thank my committee members, Dr. Brain Elbing and Dr. Ha Bai, for their insight and guidance throughout this process and for providing me with very helpful feedback on my work. I would especially like to thank Dr. Jacob for his instruction throughout this extensive process. He was always there to give me advice and guidance on how to carry out experiments and keep me focused on the overall goal. Next, I would like to thank my family for being such a wonderful support system throughout this ordeal. First, I would like to thank My mother, Dianna Brenner, for always giving me encouragement. I would also like to thank my nephew, Kaleb Brenner, for always being there to play a round of video games with me for some much-needed thesis breaks. Finally, I would like to thank my wife, Tiffany Brenner, for being my greatest supporter and always pushing me to do more. No matter what task I was undertaking she was there for me through it all, whether it was bringing me pizza to the lab at midnight during some late-night testing or reviewing and editing my papers to catch the numerous of mistakes I had written. I owe so much to her and I would not have finished this thesis without her support.

Funding is provided in part by the NASA University Leadership Initiative under Grant Number 80NSSC20M0162 (WINDMAP), the National Science Foundation, under Grant Number 1925147 (NRI: INT: Safe Wind-Aware Navigation for Collaborative Autonomous Aircraft in Low Altitude Airspace), and the Oklahoma State University Tier 1 Initiative (Drones for Good). Additionally, this work is supported in part by the National Science Foundation under Grant No. 1539070, *Collaboration Leading Operational UAS Development for Meteorology and Atmospheric Physics (CLOUD-MAP)*, and Grant No. 1925147, *NRI: Safe Wind-Aware Navigation for Collaborative Autonomous Aircraft in Low Altitude Airspace*, and by NASA under the University Leadership Initiative. Additional support provided by the OSU Unmanned Systems Research Institute. I appreciate the assistance of many USRI staff and students.

Acknowledgments reflect the views of the author and are not endorsed by committee members or Oklahoma State University.

Name: JAMES BRENNER

Date of Degree: JULY, 2021

Title of Study: INFLOW ANALYSIS FOR MULTI-ROTORS AND THE IMPACT ON SENSOR PLACEMENT

Major Field: MECHANICAL AND AEROSPACE ENGINEERING

Abstract: As the usage of small multi-rotor unmanned aircraft systems (sUAS) continues to grow there is a need to understand the complex flow-field and its interactions with the propellers and the sUAS airframe. It is particularly important to understand the interactions of the inflow and downwash with sensors mounted on the structure, such as chemical, thermodynamic, or wind sensors where interactions may contaminate the measurements. This effort maps the in-flow around a multi-rotor using experimental techniques of PIV and flow visualization. These experiments determine the effectiveness of sensors onboard multi-UAVs for atmospheric measurements. The study includes a dual and quad rotor systems to analyze the effect of multiple rotors. The rotors are placed in a water tunnel to allow for the flow visualization and PIV data collection. Then the inflow velocities of a single rotor were mapped out using a large rotor in controlled experiment. Finally, an ultra-sonic anemometer was mounted in several different locations on a heavy-lift quad-copter and the performance of each position was evaluated to determine the optimal location for the sensor.

TABLE OF CONTENTS

LIST OF TABLES

Table Page

LIST OF FIGURES

Figure Page

Figure Page

CHAPTER I

INTRODUCTION

1.1 Motivation

With the advancements of UAV technology in recent years, the industry is continuing to expand. UAVs have promise to transform several industries such as delivery, transportation, and surveillance in the US. One field that UAVs are rapidly expanding in is atmospheric data collection. By outfitting multi-rotor UAVs systems with sensors such as wind, temperature, and humidity, researchers can gather detailed atmospheric data in places that were previously difficult by normal methods.

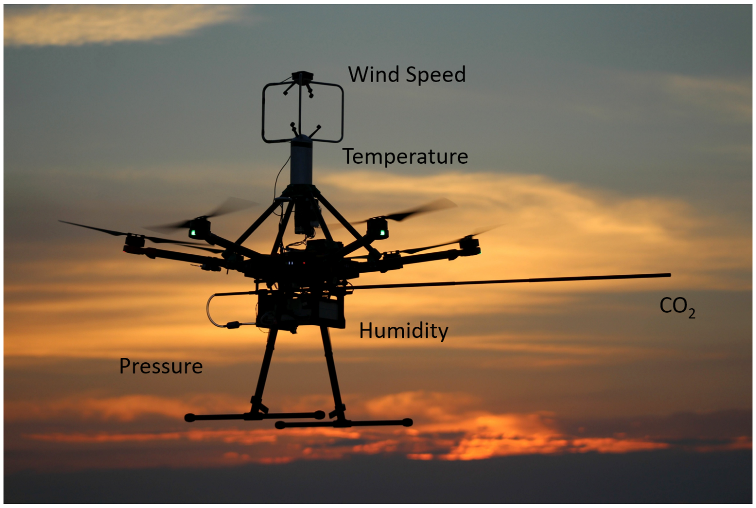

Figure 1: URSI Multi-Rotor Sensor System

Wind sensors such ultra-sonic anemometers and multi-hole probes have shown great promise in being able to capture the complex characteristics of the atmospheric boundary layer. These types of sensors can be greatly affected by the flow-field from the rotors. Several researchers have already created their own various UAV weather systems. [17], [1], and [12] and they all ran into the same question. What is the optimal placement for the sensitive wind sensors in order prevent rotor flow from impacting the measurements? While single rotor systems such as helicopters have been around since 1939 [16] and their respective flow fields are well understood, little work has been done over the flow field for multi-rotor systems. By gaining a better understanding of the fluid dynamics of these multi-rotor systems researchers will be able to determine the optimal sensor placement. This research aims to observe the fluid dynamics of multi-rotor systems using experimental methods and provide general guidance for future researcher's wind sensor placement to avoid the flow-field from impacting the measurements. The main goal of this research is the analysis of the multi-rotor flow-field and determining its impact on wind sensors. By using experimental methods, the researcher can provide general guidance for optimal wind sensor placement for future researchers. This will include determining the velocity and direction of the flow. To understand the intricate fluid dynamics of multi-rotors an experiment was conducted using Particle Image Velocimetry (PIV). Then an experiment examining the single rotor inflow velocities will be conducted. This experiment gives an idea of the distances and size of the inflow velocities for a single rotor. Finally, by mounting an ultra-sonic anemometer to heavy-lift quad-copter, several flights tests were conducted. These tests compared the data gathered from the quad-copter mounted anemometer to a tower with a similar ultra-sonic anemometer mounted to it. These flights examined several different mounting positions on-top of the quad-copter and determined the best position for the anemometer.

1.2 Background

The lowest portion of the Earth's atmosphere, known as the atmospheric boundary layer (ABL), plays an important role in the formation of weather events [14]. Most of the modern weather forecasting is focused on the upper atmosphere using weather balloons and doppler radar. Because of this, there is a data gap that small multi-rotor Unmanned Vehicle (sUAV) can fill. Multi-rotors UAV's are small aerial vehicles that use more than two lift-generating rotors. By equipping these systems with weather sensors, they can take off and land vertical (VTOL) and fly to a location and hover in place to collect data. Careful consideration must be given to the wind sensor's placement as the rotors from the sUAV create a flow-field that can easily interfere with the sensitive wind sensors. A flow-field is the distribution of the density and velocity of a fluid over a space and time [6]. For a spinning rotor the flow-field is generated as the rotors spins and pulls the air in from the surroundings and pushes it downward to produce thrust. For a single rotor system these dynamics are relatively well understood, [11] but by adding multiple rotors to the system the flow-field becomes more complex. As each rotor creates its own flow-field that interacts with the others rotor's flow-field due to proximity with each other. From previous research it was determine that optimal location is generally located above the rotors of the sUAV [4], because the inflow velocities are much smaller than down-wash velocities for the multi-rotor flow-field. What is not well understood is the exact location and distances above the rotors.

1.3 Goals and Objectives

The main goal of this thesis is the analysis of the multi-rotor flow-field and determining its impact on wind sensors. By using experimental methods, the researcher can provide general guidance for optimal wind sensor placement for future researchers. This research will attempt to obtain the total volume of air affected for varying sizes of multi-rotor systems. Additionally, it will analyze the complex fluid dynamics of multi-rotor flow. This will include determining the velocity, direction and voracity of the flow. This research will then determine the optimal wind sensor location. Once this location is determined this thesis will provide guidance on exact distances and mounting configurations for a range of multi-rotor sizes.

1.4 Thesis Outline

This paper will start with a brief background on multi-rotor UAV's in Chapter II. It will also provide a brief overview of wind sensors and the importance of the ABL. This section will cover the previous work done in using UAVs as weather data collectors. Chapter III will cover the experimental methods used to meet the goals of this thesis. To understand the fluid dynamics, a PIV experiment will be conducted in a water tunnel. The experiment will test two and four rotor configurations. This experiment will provide the detailed dynamics of the rotor flow-field. The PIV experiment was used to determine the optimal location for wind sensors. Next, the single rotor experiment determined the average distances for inflow velocities for single large rotor. Uses the results from this several flight tests were conducted to examine different mounting positions for ultra-sonic anemometer on to a quad-copter. Chapter V will discuss the conclusion of this research and provide guidance and recommended methods for wind sensors integration.

CHAPTER II

BACKGROUND

2.1 Multi-Rotors

This section focuses on the history and development of the small electric multi-rotor UAVs as well as a brief introduction on the components that make up a multi-rotor UAV.

2.1.1 Multi-Rotor History

The first manned multi-rotor aircraft was designed and built by the Brequet brother in 1907[33], seen below. It was called “Rotor Craft One” but due to technical constraints of the time the pilot could not control the aircraft. Balancing the aircraft was extremely difficult and required constant adjustment of the motors RPM to keep the aircraft stable. After that the industry moved on from multi-rotor systems and instead focused on the development of single rotor systems “Helicopters”. Helicopters utilize a main large rotor on top of the system to provide lift and a smaller tail rotor to balance out the moment and keep the system stable [15]. The helicopter was able to take off and land vertically (VTOL)

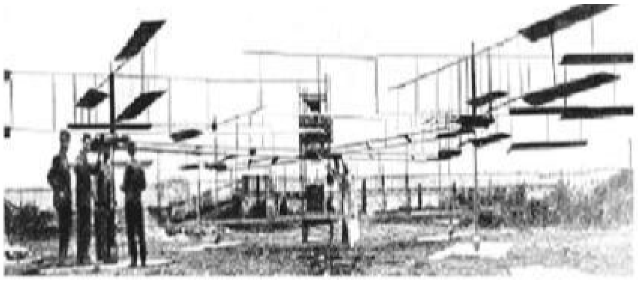

Fig.1 Breguet-Richet's "Gyroplane No1" oil move multi-rotor unmanned aerial vehicle (multi-rotor UAV)

Figure 2: Rotor One

as opposed to fixed-wing aircrafts that required a large runway. This type of system was easier to control and thus took the place for the worlds VTOL needs. The development of multi-rotor systems was largely stagnate until the 1990s where the advancement of micro-electromechanical systems (MEMS) and brushless motors, brought multi-rotor systems back to the forefront of technology development. The MEMS were light enough to be carried on small unmanned battery-powered multi-rotor systems (multi-rotor UAVs). Leading industry companies like DJI, Innovations, and Parrot helped develop the small multi-rotor UAVs into what it is today, by producing small unmanned battery-powered multi-rotor UAVs that are used for aerial photographer and variety of other applications.

2.1.2 Multi-Rotor Overview

The basic definition of small unmanned battery-powered multi-rotors is any unmanned vehicle that has more than one main rotor providing thrust. The most common design configurations are 4, 6, 8 rotors. The 4-rotor system is the most popular and is more commonly known as a "quadcopter". This system consists of 4 motors that are mounted on four symmetrical arms, each arm is spaced 90 degrees apart. The arms consist of two pairs of motors that rotate counterclockwise and two pairs of motors that rotate clockwise, seen below. By doing this the motors torque balances out and the aircraft becomes stable. By varying the RPM of the motors the aircraft achieves six degrees of freedom with just the four control inputs. There are two general configurations for the quadcopter, a X-configuration and a plus-configuration, seen below [19]. The x-configuration is by the far the most popular,

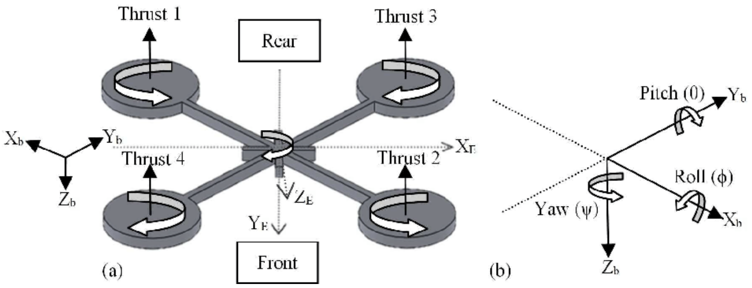

Figure 3: Quad-copter Diagram

as the front of the UAV provides a great space to mount a forward facing camera.

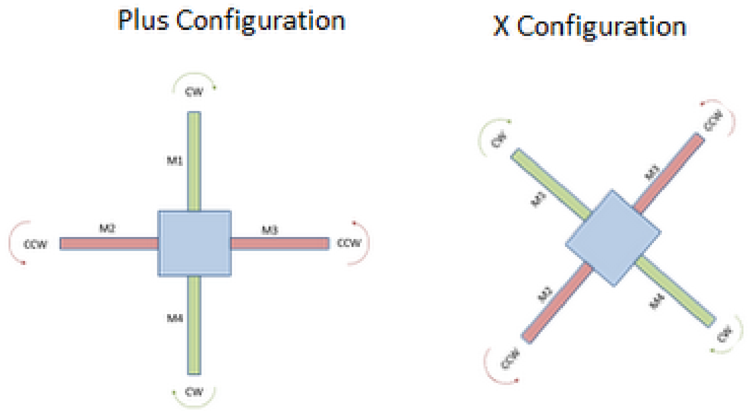

Figure 4: Quad-copter: Plus and X Configuration

Each multi-rotor uses the same basic five components. The components can vary in size and complexity, but they all perform the basic function. First, all multi-rotor UAVs use a frame, as the skeleton of the aircraft the frame holds all the other components together. Frames are typical, made from light and strong materials such as carbon fiber [20]. The size of the frame varies depending on the size of the aircraft, number of motors, and size of propellers, but typically sizes can range from 5-52 inches. Next, electric speed controllers (ESCs) are the components that interpret the signals from the flight controller and translates them into electrical pulses to each motor. The size again varies depending on the size of motors and batteries on-board the aircraft. Each motor on the aircraft requires its own ESC. Next, brushless motors provide the motion for the propellers spin and create thrust for the aircraft. The motors are rated by kilovolt (kV). Generally, the lower the kV the greater thrust the motor can provide and higher the kV the faster the motor can spin. The propellers create the lift for the aircraft. Propellers come in two main types: dual and tri blade. They are typically made from injected mold plastics. The electric battery powers the aircraft. The most popular type is lithium polymer (lipo), because of their high energy density and high discharge rate. The capacity of the battery is measured in milliampere hour (mAh). Typically, higher (mAh) means longer endurance for the aircraft. Finally, the flight controller is the brain of the system. It contains the inertial measurement unit (IMU).

The IMU is electronic device that measures and reports a body's specific force, angular rate, and orientation. This allows aircraft to understand how it is moving in 3D space. The flight controller uses algorithms to calculate how fast each motor should spin as the pilot is commanding inputs with a controller or from an autopilot [22].

2.2 Rotor Basics

The fundamentals of rotor follows the traditionally finite wing theory [32] in that the rotor acts as rotating wing, by transferring rotational power into thrust. The rotor accomplishes this by displacing the air surrounding the blade and pushing it below itself. This movement of air results in pressure difference with low pressure zone above the rotor and a high pressure zone below the rotor [7]. This pressure pushes the rotor up creating thrust to lift the multirotor.

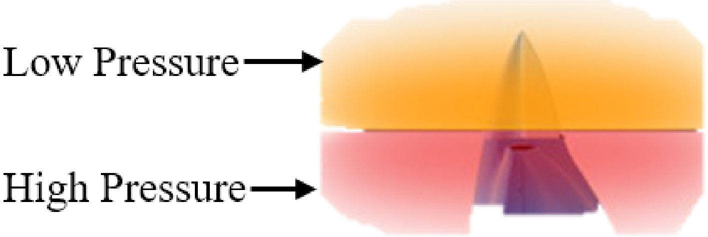

Figure 5: Rotor Pressure Zones [7]

The basic terms of rotors that determine the properties of the rotor are as follows. Chord length is the imaginary line drawn from the center point (hub) of the rotor's leading edge to the trailing edge. The pitch is the twist or angle of the rotor-blade. It essentially measures how far the rotor would move forward in one revolution. The pitch controls the speed of the air leaving the bottom of the rotor. The pitch angle changes as it moves down the blade with the steepest twist angle at the hub and the shallowest angle at the tip.

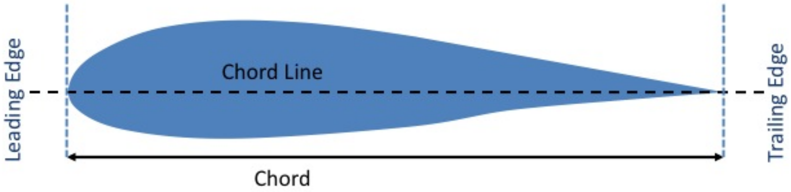

Figure 6: Rotor Pressure Zones

2.3 Rotor Flow

This section will cover the basics of rotor flow. The flow-field will be divided into three main regions. The inflow, the region above the rotors, the blade-flow, the region on the in-plane, and the outflow, the region below the rotors. As stated in chapter 1 the flow-field dynamics for single rotors is fairly understood but that is not the same for multi-rotors systems. Previous research will be covered to give the basic understanding of the flow-field.

2.3.1 Rotor Outflow

First, the outflow or down-wash is the flow-field region below the rotors. Researcher Yoon S, performed computational studies [35] "High-Fidelity Computational Aerodynamics of Multi-Rotor Unmanned Aerial Vehicles" investigated the inherently unsteady nonlinear and complex flow for small multi-rotor vehicles. The study conducted their tests over the popular consumer UAV DJI Phantom 3 in a full version and "simplified" version removing the landing gear and camera.

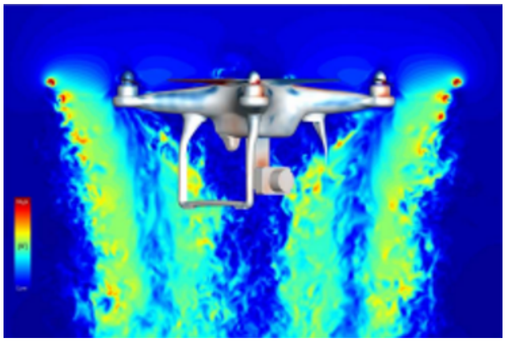

Figure 7: DJI Phantom 3

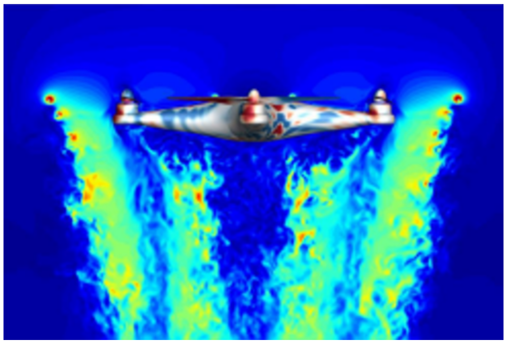

Figure 8: Simplified Phantom 3

The software they used was the OVERFLOW CFD solver that is finite-difference, overset, high-order accurate Navier-Stokes flow solver. The researchers determined that presence of the air-frame produces a download but reduces the interaction between the down-wash, therefor the four rotors generates less thrust without the air-frame than with it.

Another CFD study conducted over the downwash of multi-rotors was done by [28] Zheng Y. “The computational fluid dynamics modeling of downwash flow field for a six-rotor UAV”. The goal of this research was to create a CFD that simulates the downwash of a multi-rotor to better understand the downwash influence has on droplets for agriculture pesticides. The flow field surrounding the UAV were established in UG software, the physical model and flow fields were meshed using ANSYS software. The study was done over a hexa-copter multi-rotor that is commonly used in agriculture fields. The study varied different hover heights in the CFD and observed how the different heights changed the flow-field. The researchers concluded that the current speeds and streamline distributions of the UAV are relatively complex. As hovering height increased, the minimum current velocity increased then decrease, as well as the pressure around the UAV and ground effect decreased.

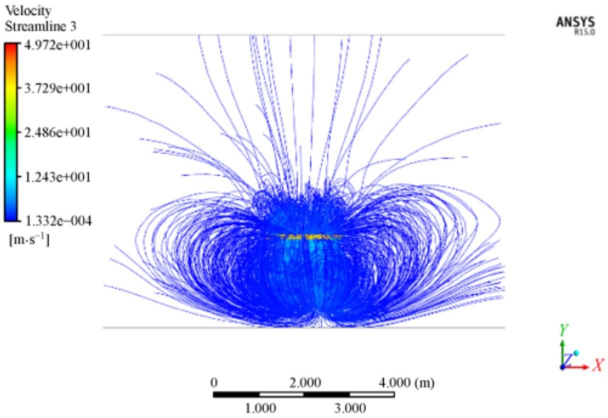

Figure 9: CFD model of downwash airflow of a UAV

Finally, researcher Whyte examined the down-wash of a single rotor in ambient conditions using PIV [34]. The goal of the research was to determine the optimal locations for wind sensors on multi-rotor UAVs by isolating the effect of a single rotor from the entire system. The experiment observed a significant dead region below the rotors directly beneath the rotor hub as well as beneath the boom. The greatest vertical velocities occurred beneath the rotor along the mid-point of the rotor.

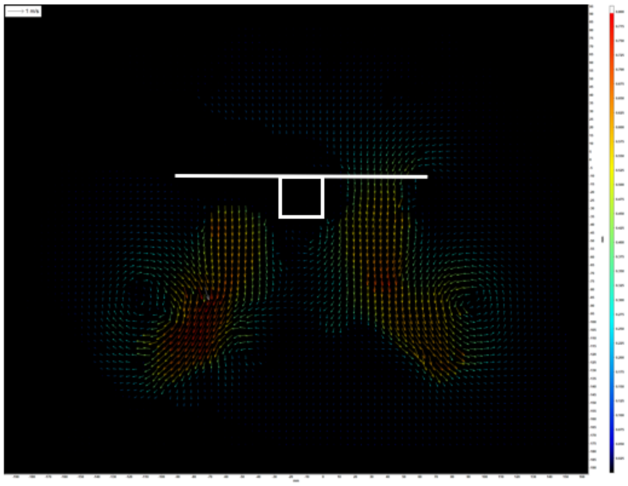

Figure 10: CFD model of downwash airflow of a UAV

From this research it is assumed the velocities of the outflow region are significantly greater then the velocities of the inflow region, with only a minimal small region of dead space beneath motor hubs. This makes the outflow region a poor candidate for sensor placement.

2.3.2 Rotor In-plane flow

The in-plane flow region, is the region on the rotor blade plane. Donnel's [12] research conducted a PIV experiment with the goal analyzing this region for senor mounting locations. The testing was performed indoors and the aircraft was fixed in a stationary position and fixed to a stand in a hover configuration. Three regions on the quad air-frame were examined, open rotor, rotor-airframe interaction, and rotor-rotor interaction, see blow.

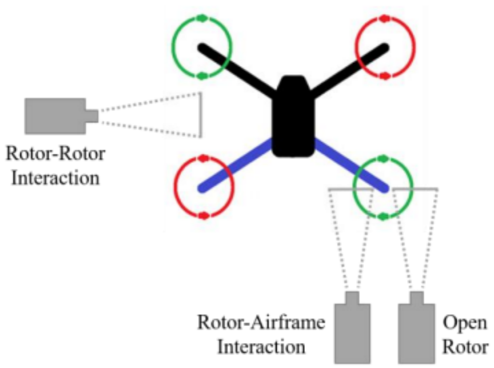

Figure 11: Camera Orientation with Respect to Aircraft

The experiment showed the rotor-airframe interaction tests the tip vortices are functioning the same as open rotor but the downwash is interrupted by the airframe creating turbulence and velocity variations. For the rotor-rotor interaction test, tip vortices exist for each rotor and there clear are interactions between the tip vortices creating a significant turbulent region. The conclusion from this study was to place the sensor away from the downwash on the fuselage centerline furthest away from the rotors as possible. The tests showed for the rotor-airframe interaction the tip vortices function the same as the open rotor test but the downwash is interrupted by the airframe creating turbulence and velocity variations.

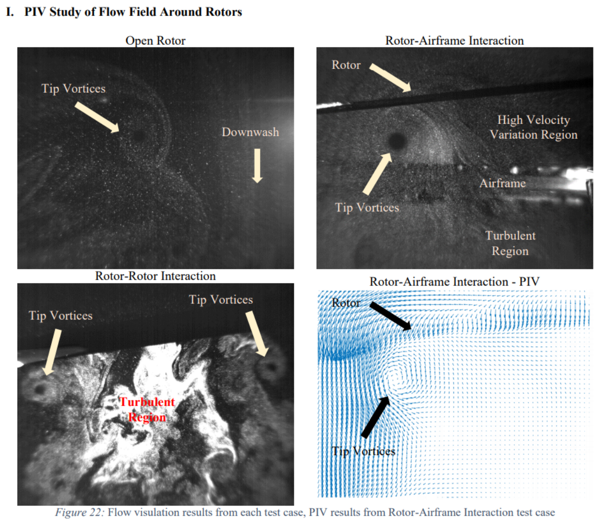

Figure 12: PIV Study of Flow Flow Field Around Rotors

Additionally, Yoon [35] also examined the in-plane flow of multi-rotors with CFD experiments. Yoon concluded that the blade-tip vortices in the front and back two vortices are created as reverse flow comes from below the quad-copter to answer the need of more air to feed the rotors. These vortices are stronger when more components are added to the air-frame. This study provides a detail computational over multi-rotors and the interactions on the system.

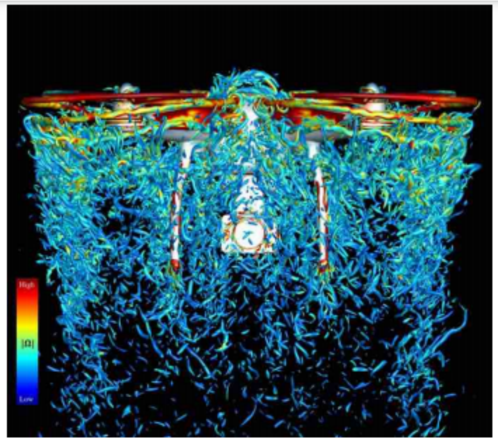

Figure 13: DJI Phantom 3

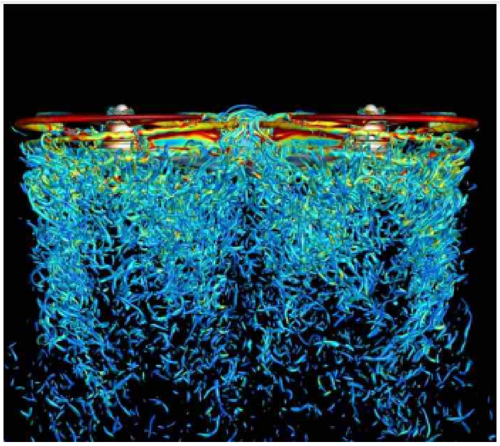

Figure 14: Simplified Phantom 3

In conclusion, these studies observe that the in-plane flow is turbulent and has significant variations in velocity. Each rotors creates tip vortices that can interact with the other rotors and these vortices will become stronger with more compents added to the airframe. This makes the in-plane region a poor choice for wind sensor placement.

2.3.3 Rotor Inflow

Next the inflow region above the rotors. Researcher Gerrit performed experiments to investigate the inflow affects on wind sensors in [24] “Two New Technologies to Measure the Turbulent Wind Vector Abroad Small Research UA”. The goal of the research is to evaluate the ability of two sensors to accurately measure the turbulence above a multi-rotor based UAV. Two different tests were conducted, a indoor and outdoor test in ambient conditions. In both tests the quad-copter was placed 1 meter above ground with sonic anemometer 1 meter above the quad.

Figure 15: Multi-Rotor UAV Platform

In both test the induced velocity of the quadcopter inflow could be seen. The indoor vertical wind component was -0.3 m/s and the outdoor was 0.36 m/s. Interestingly, the researcher also found the air is affected by inflow of the rotors up to at least 1.40 m around the quad system. Gerrit's research shows that inflow does effect wind sensors but significantly lower then the outflow region.

Another study that investigated the inflow for small multi-rotors was by researcher P. Bruschia. They investigated the inflow for small multi-rotors on anemometers [9] "Wind speed and direction detection by means of solid-state anemometers embedded on small quad-copters". The goal of this research effort was to design and build a small quad-copter that uses a 2D anemometer to provide local wind speed estimates.

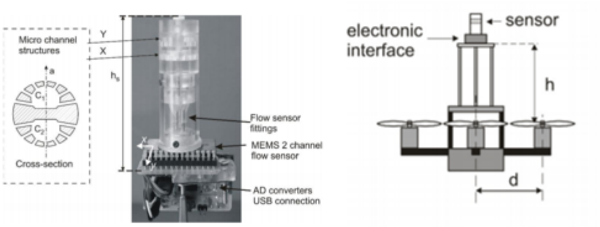

Figure 16: Multi-Rotor

The system was a small quadcopter, that mounted a 2D anemometer 22 cm above the rotors on fuselage centerline. The researchers ran experiments to investigate the inflow effects on the flow measurements. The tests were conducted by placing the system inside a wind tunnel at two specific yaw angles 0 and 45 degrees and tested at speeds from (0-20+) m/s.

The results suggest that the propellers only have a significant effect on the estimated speed below 10 m/s, while angle measurement remains practically unaffected for the whole test.

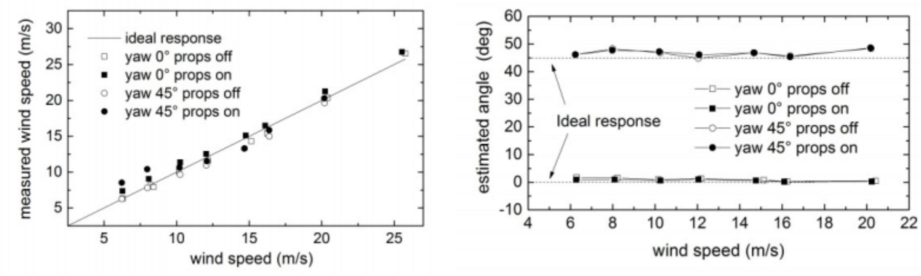

Figure 17: Measured wind velocity (left) and direction (right) as a function of the ground truth wind speed with the sensor mounted on the quad-copter

In conclusion, the inflow region has much smaller velocities than the outflow. These velocities are mainly in the negative z-direction as the flow gets pulled down into the rotors. This makes the inflow the optimal region to place wind sensors in. Further investigation is required to understand the flow-field of multi-rotor UAvs. Additionally, the optimal distance needs to be determined for small multi-rotors UAVs.

2.4 Atmospheric Boundary Layer

A boundary layer is a thin layer of viscous fluid close to a solid surface in contact with a moving fluid, the flow velocity varies from zero at the surface up to free-stream velocity at the boundary [26]. The ABL is the bottom layer of the troposphere that contacts the earth's surface [27]. It is roughly 1 km thick and it is often turbulent and capped by a stable layer of air or inversion cap. There are two main surface-to-air interactions, mechanical and thermal. The mechanical interaction comes from the friction exerted by the wind against the ground surface, this friction causes the wind to be sheared and creates turbulence. The thermal interaction is caused by the sun's solar radiation shining through the ABL and heating the surface. The surface then in turn radiates this heat upward through the ABL. During fair weather over land, the ABL has a marked diurnal cycle. During the daytime, mixed layer of turbulence increases, capped by a stable entrainment zone of intermittent turbulence.

During the evening, the turbulence decreases, leaving a residual layer in place of the mixed layer. During the nighttime the bottom of the residual layer is transformed into a stable boundary layer by radioactively cooled surface [27].

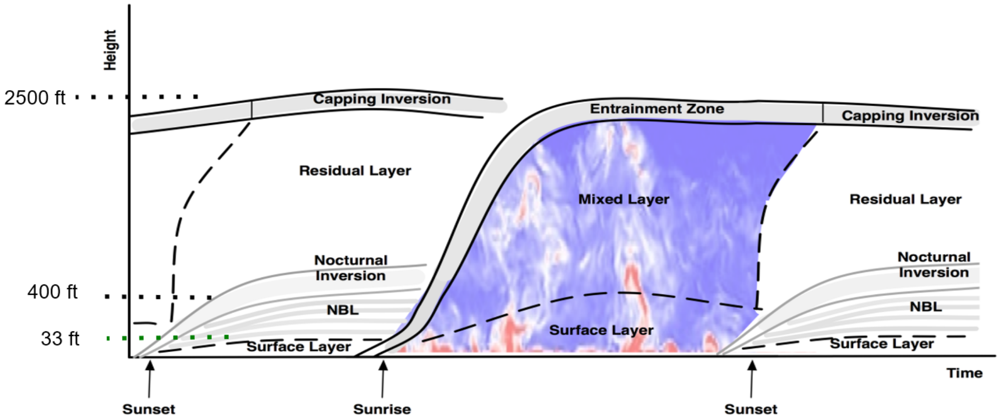

Figure 18: Atmospheric Boundary layer

2.5 Anemometer Overview

The word anemometer or wind meter is any device used for measuring wind speed. [18]. The term is derived from the Greek word anemos, meaning wind and is used to describe any air speed measurement used in meteorology or aerodynamics. The first known description of anemometer was given by Leon Battista Alberti around 1450 [2]. Since then there have been a variety of anemometers developed.

2.5.1 Cup Anemometer

The cup anemometer consists of three or four empty conical/hemispherical cups. The hollow cup shells are mounted to a bracket and the whole cross-arm bracket is fixed on a vertical rotating axis. The wind speed then causes the cups to rotate and the wind speed is determined from the number of revolutions and the circumference.

$$v = \frac{RPM}{min} \cdot C \tag{2.5.1}$$

The benefits of the sensor is that they are low cost and easy to construct. The sensor does not tell wind direction and requires a minimum amount of wind 0.9-.1 m/s to work properly [23].

Figure 19: Cup Anemometer

2.5.2 Propeller Anemometer

The propeller anemometer works on the principle that blade system of the quasi-airflow is affected by wind pressure, which produces torque and makes the blades rotate. The propeller speed sensor measures the wind speed by rotating a group of three to four propellers around a horizontal axis. The propeller is usually installed in front of the wind vane which rotates to face the wind. The sensor can accurately measure wind speed up to 90-100m/s[29]. The propeller anemometer is similar to the cup anemometer but with the added benefit of measuring wind direction.

Figure 20: Propeller Anemometer

2.5.3 Hot Wire Anemometer

The hot-wire anemometer sensor works by backing out wind speed through thermal dissipation [10]. This sensor consists of the a hot wire, usually tungsten or platinum, it can also be a hot film constructed of either platinum and tungsten. This wire or film is exposed to the air and connected to what is called a Whiston Bridge. This wire is heated up to a set temperature, as air moves over the heated wire and it is cooled.

Figure 21: Hot Wire Anemometer

The energy dissipation equation determines the heat loss from the heated wire is

$$I^2R = a(vp + b)^{1/2} \tag{2.5.2}$$

and the velocity equation is

$$v = \frac{I^2R/a^2 - b}{\rho} \tag{2.5.3}$$

The larger the flow speed of the air the larger the corresponding heat release coefficient and vice versa. In summary, the sensor is a thermal wind sensor that is a function of current and resistance. The benefits of this sensor is that it is a small volume, has no moving parts and has a high frequency response (1MHz). The downsides are that the sensor is it not very accurate and is difficult to calibrate.

2.5.4 Pitot Tube

This sensor is very common in the aerospace industry. The pitot probe also knows as "airspeed tube" or "wind speed tube" is a tubular device for measuring total pressure of airflow to determine the airflow speed.

Figure 22: Pitot Tube

It was first invented by H. Pitot of France. This device is used mainly to determine the airspeed of an aircraft. It functions by measuring the differential pressure and using Bernoulli's theory to determine the velocity of the air [5]. The equation that determines the velocity from the differential pressure is defined as,

$$v = \sqrt{\frac{2(P_0 - P_\infty)}{\rho}} \tag{2.5.4}$$

This sensor is accurate, cheap and has no moving parts. The downside of this sensor is that it can not determine the wind direction.

2.5.5 Multi-Hole Probe

Next, the multi-hole probe (MHPs). This sensor is similar to the pitot probe but instead of having one center hole the sensor has multiple holes at the tip. Commonly, multi-hole probes come in five or seven hole configurations. These extra holes allow the probe back out [5]. Calibrating the probes by sweeping them through a known flow-field allows the wind speed and direction to be derived. The key to calibrating MHPs are the coefficient

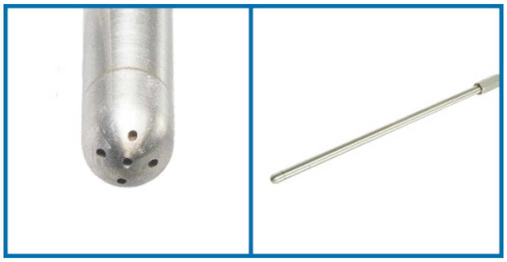

Figure 23: Multi-Hole Probe

of pressures. The pressure coefficient is a non-dimensional feature that is defined by the pressure difference over the dynamic pressure. The dynamic pressure is defined as,

$$q = p_a - p_\infty = \frac{1}{2} \cdot \rho_\infty \cdot U_\infty^2 \tag{2.5.5}$$

For the pitch angle, this is

$$C_{p\theta} = \frac{P_2 - P_4}{P_1 - P_a} \tag{2.5.6}$$

and for the yaw angle, the equation is

$$C_{p\phi} = \frac{P_3 - P_5}{P_1 - P_a} \tag{2.5.7}$$

and for pitot coefficient of pressure

$$C_{pPitot} = \frac{U_{pitot}}{U_\infty} \tag{2.5.8}$$

The benefits of this sensors is that requires no moving parts and is accurate. The downsides are the sensor is expensive and difficult to calibrate.

2.5.6 Ultra-Sonic Anemometer

Finally the ultra-sonic anemometer. The ultra-sonic's uses the ultrasonic time difference method to measure the wind speed. The speed that sound travels in air superimposes the velocity of the wind onto it.

Figure 24: Ultra-Sonic Anemometer

The sensor applies this method by having four ultra-sonic transducers emit an ultra sonic sound that is recorded by the opposing transducer. Normally, the velocity of this sound is the same for both directions. It is equal to the speed of sound, which depends mainly on the air temperature. The equation for the speed of sound is defined as,

$$v_p = 331.82(1 + 1.83 * 10^{-3} * T) \tag{2.5.9}$$

The time for the sound to travel to and from the opposing transducers will be affected by the wind speed and direction of the flow-field [3]. The equations for the altered velocity of the sound wave that is propagating in direction parallel to the wind is,

$$v_{12} = v_p + v_w \tag{2.5.10}$$

$$v_{21} = v_p - v_w \tag{2.5.11}$$

$$v_{34} = v_p + v_w \tag{2.5.12}$$

$$v_{43} = v_p - v_w \tag{2.5.13}$$

With the distance between the transducers, the velocity of sound is,

$$v = \frac{d}{t} \tag{2.5.14}$$

by substituting the Eq. 2.11 into the previous equations the wind velocities and direction can be determined as,

$$v_{w1} = \frac{d}{2}(\frac{1}{t_{12}} - \frac{1}{t_{21}}) \tag{2.5.15}$$

$$v_{p1} = \frac{d}{2}(\frac{1}{t_{12}} + \frac{1}{t_{21}}) \tag{2.5.16}$$

$$v_{w2} = \frac{d}{2}(\frac{1}{t_{34}} - \frac{1}{t_{43}}) \tag{2.5.17}$$

$$v_{p2} = \frac{d}{2}(\frac{1}{t_{34}} + \frac{1}{t_{43}}) \tag{2.5.18}$$

The benefit of this sensor is that it has no moving parts, high accuracy, and can determine wind direction. The downsides is that they are expensive compared to the other sensors.

2.6 Previous Work in Weather Sensing UAS

Over the years there have been numerous research projects that have developed atmospheric sensing UAV's. Research teams have experimented with different types of UAVs such as fixed-wing, multi-rotor, and VTOL aircraft. Each team showed progression and refinements of using mobile UAVs as atmospheric weather instruments. This section will cover the most applicable research efforts and lessons they learned.

2.6.1 Fixed-Wing UAS

One of the first successful projects was the “M2AV Carlo” [17].

Figure 25: Fixed-Wing UAV Carlo

The goal of the Carlo was to acquire vertical profiles of temperature, humidity, and wind up to 1500m a.g.l. These vertical profiles are important to characterize the vertical structure of the low troposphere. The vertical variation of wind speed and direction leads to wind shear which produces turbulence and thus turbulent fluxes in atmospheric boundary layer. For the sensor package they used a 5-hole probe for wind speed and direction, a thermocouple for temperature readings, and the "Vaisala HMP 50" for humidity recordings. The sensor package had a response time of 30 Hz and with the UAV having climbing rate of 3 m/s which enables vertical resolutions of 10 cm for temperature, humidity, and wind speed and direction. The Carlo flew in the LITFASS-2009 campaign on July 21, 2009. The UAV flew four vertical profiles at Lindenberg Germany. That day central Europe was influenced by a low pressure system over the eastern Atlantic. The figure below shows the comparison between Carlo collected data and the radiosonde.

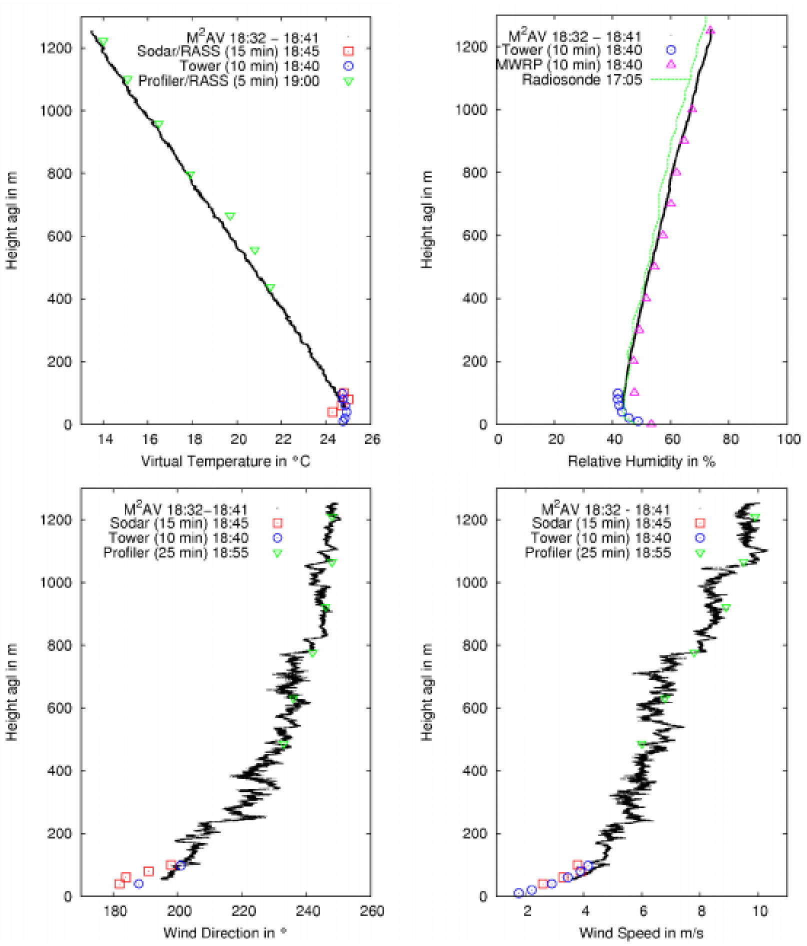

Figure 26: Carlo Atmospheric Collected Data and Radiosonde Comparison

The results of the Carlo show very well in line with other ground based measuring systems. The Carlo system show that fixed-wing UAVS are capable of taking accurate atmospheric data at a faster frequency then what current weather systems (ballons) can currently do. While Carlo was successful, by using a fixed-wing the aircraft is unable to hover in place to collect data. By using a multi-rotor UAV this provides the ability to VTOL and hover in place.

2.6.2 Multi-Rotor UAS

Researcher Fernando Carbajo Fuertes demonstrated the ability multi-rotor weather sensing UAV is his work [13] “Multirotor UAV- Based Platform for the measurement of Atmospheric Turbulence. Instead of using fixed-wing UAVs, Fernando's team used a multi-rotor octocopter to take measurements.

Figure 27: Multi-Rotor UAV Platform

The goal of the project was to develop a technique for the measurement of atmospheric turbulence and temperature at specific point in space. To accomplish this the sensor package required a sensor that had high refresh rate and is capable of recording wind speed and direction. The team decided on a fast-response multi-hole probe. Shown below the probe had a response rate 600 Hz and has measurement range of 2-30 m/s. The probe itself is 10cm long cylindrical body with a 5cm long and 2 mm diameter head. By using IMU and GPS data they were able to reconstruct the velocity vector. Mounting the probe outside the rotor effects proved to be a challenge. The probe was mounted with carbon fiber booms that extended 115 cm upstream of the system. They stated that this was outside the rotor wash but did not provide any verifying data. Once the system was constructed it was validated by flying the UAV near a meteorological tower equipped with ultra-sonic anemometer.The height of the tower was 25m well above any ground effect that could occur from the rotor wash. There were four flight tests completed, each test's data was collected for 500 seconds. Below is shown the data collected and compared to the anemometer

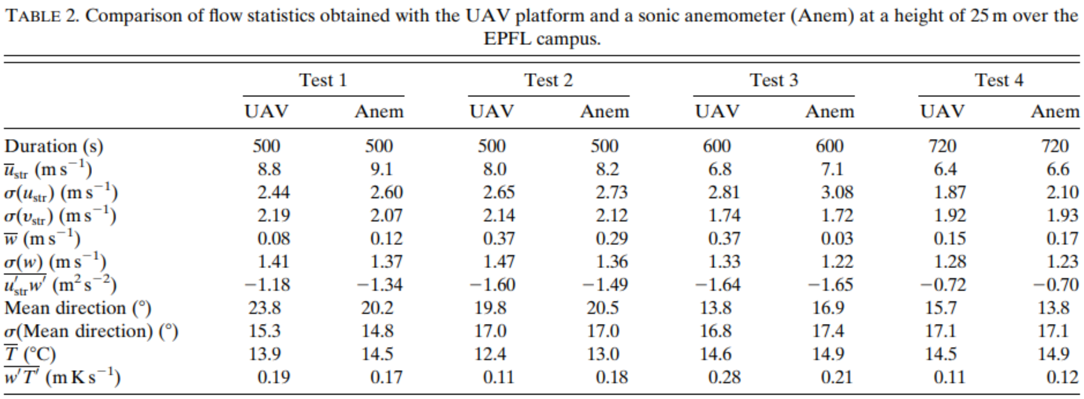

TABLE 2. Comparison of flow statistics obtained with the UAV platform and a sonic anemometer (Anem) at a height of 25 m over the EPFL campus.

	Test 1		Test 2		Test 3		Test 4	
	UAV	Anem	UAV	Anem	UAV	Anem	UAV	Anem
Duration (s)	500	500	500	500	600	600	720	720
$\overline{u}_{\mathrm{str}}$ ($\mathrm{m\,s^{-1}}$)	8.8	9.1	8.0	8.2	6.8	7.1	6.4	6.6
$\sigma(u_{\mathrm{str}})$ ($\mathrm{m\,s^{-1}}$)	2.44	2.60	2.65	2.73	2.81	3.08	1.87	2.10
$\sigma(v_{\mathrm{str}})$ ($\mathrm{m\,s^{-1}}$)	2.19	2.07	2.14	2.12	1.74	1.72	1.92	1.93
$\overline{w}$ ($\mathrm{m\,s^{-1}}$)	0.08	0.12	0.37	0.29	0.37	0.03	0.15	0.17
$\sigma(w)$ ($\mathrm{m\,s^{-1}}$)	1.41	1.37	1.47	1.36	1.33	1.22	1.28	1.23
$\overline{u'_{\mathrm{str}}w'}$ ($\mathrm{m^2\,s^{-2}}$)	−1.18	−1.34	−1.60	−1.49	−1.64	−1.65	−0.72	−0.70
Mean direction (°)	23.8	20.2	19.8	20.5	13.8	16.9	15.7	13.8
σ(Mean direction) (°)	15.3	14.8	17.0	17.0	16.8	17.4	17.1	17.1
$\overline{T}$ (°C)	13.9	14.5	12.4	13.0	14.6	14.9	14.5	14.9
$\overline{w'T'}$ ($\mathrm{m\,K\,s^{-1}}$)	0.19	0.17	0.11	0.18	0.28	0.21	0.11	0.12

Figure 28: UAV Data Collected and Tower Data

The UAV measurements are in good agreement with the tower. Averaged wind speeds were between a 3-10 percent standard deviation. The temperature was always within 0.5 C which lies within the accuracy -+2C given by the manufacturer of the sonic anemometer. The results of the project show that it possible to use multi-rotor to accurately take atmospheric measurements from a multi-rotor using MHPs. This research shows the benefit of using multi-rotor for the hovering and VTOL ability allowing the UAV system to consistently record data at a specific point for extended periods of time. The downsides this system is using a MHP that is only able to take wind direction within a 45 degrees and required a 2 m/s minimum wind speed. Using a higher resolution sensor that is capable of 3D wind detection such as a ultra-sonic anemometer would be able to provide more accurate ABL data.

Researcher Kevin A. Adkins demonstrated this by mounting ultra-sonic anemometers to multi-rotor [1] "Development of a sensor suite for atmospheric boundary layer measurement with a small multi-rotor unmanned aerial system". The goal of this research effort was to develop a multi-rotor that is capable of taking atmospheric boundary layer measurements at point to point basis with 3D wind vectors. The team used a DJI S1000 shown below and two FT Ultra Sonic Anemometers, that each had a refresh rate of 30 Hz.

Figure 29: Multi-Rotor UAV Platform

Again, the mounting poised a challenge to the team. The sensors were mounted on the same plane as the rotors. The sensors were supported by carbon fiber booms. To avoid any type of support structure shadowing effecting the data, the anemometer measuring the vertical component of velocity (w) is mounted at the end of extension boom and for the anemometer measuring the horizontal components of velocities (u,v) was mounted vertically. The study did not present any data demonstrating that the sensors were unaffected. The downside to this system is both anemometers had to be placed far away from the UAV. This greatly increased the foot print of the UAV while also unbalancing the aircraft.

Researcher Ryan Thorpe developed a similar system to Adkins' but chose to mount the sensor above the rotors [30] "Measurement of Unsteady Gusts in an Urban Wind Field using a UAV-based Anemometer". The goal of the research was the development a UAV that is equipped with a 3-axis sonic anemometer and is capable of taking sample rate up to 200 Hz to measure turbulent wind gust in an urban environment. This was done by using a DJI S1000 and ultra-sonic anemometer created by Applied Technologies, that can measure U, V, and W components.

Figure 30: Multi-Rotor UAV Platform

The researchers mounted the sensor directly above the multi-rotor UAV via a four strut mount. The sensor was placed on the center of gravity (CG) of the UAV for better balance, while also keeping the sensor away from the downwash of the rotors. The researchers stated the inflow did not have any effect on anemometer measurements but did not provide any verifying results. The researchers were unable to find a testing location where the wind values were known. In conclusion, the team was able to take wind measurements at 200 Hz while also only using one sensor and not unbalancing the UAV. From this experiment it appears the most optimal location for sensors is above the rotors where the inflow velocities are much less then the downwash velocities below the rotors.

This hypothesis is reinforced by research efforts from Geoffrey W. Donnell “Wind Characterization” [12] and Ross T. Palomaki ”Wind Estimation in the Lower Atmosphere Using Multirotor Aircraft” [21]. The goal of these efforts were to validate and demonstrate field use of small multi-rotor UAV’s that can measure wind in 2 and 3 dimensions. Both researchers mounted ultra-sonic anemometers above the UAVs. The teams used three different anemometers Tri-sonica, Young Model 81000, and Decagon-2. All the sensors were mounted above the rotor plane, the Tri-sonica was mounted 250mm above, the Young was mounted

520mm above, and the Decagon-2 300mm above.

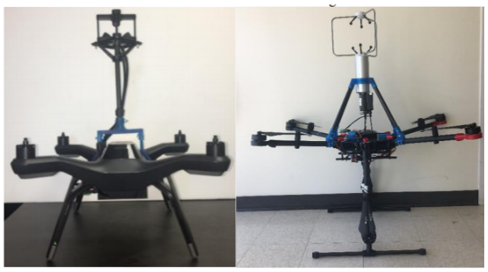

Figure 31: Multi-Rotor UAV Tri-sonica and Young

Figure 32: Multi-Rotor UAV Decagon-2

Donnell's systems were tested at the OSU flight field. Below are the results corrected for the aircraft flight dynamics and compared ground sensor measurements. There is a good agreement of the overall trend of wind behavior for the Tri-sonica measurements, but not as good for the Young measurements. The Young appeared to be out of phase of the sinusoidal wind pattern. Palomaki's conducted indoor testing system to investigate the effect of the rotors on wind measurements taken 300 mm above the copter. They concluded that the mean increase of wind speed measured by the copter anemometer was 0.5 ms-1. This bias was subtracted from the wind speed measurements in further analyses. Palomaki's also conducted flight testing outdoors and compared to tower measurements. Their results are shown below, the measurements showed good agreement with each other with only a average 0.5 ms difference.

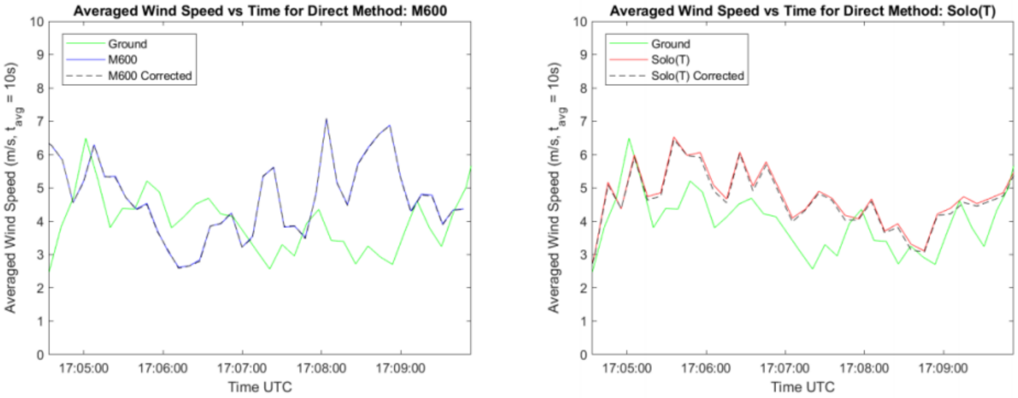

Figure 33: Comparison of Young and Tri-Sonica Wind Speed Senors with Ground Data

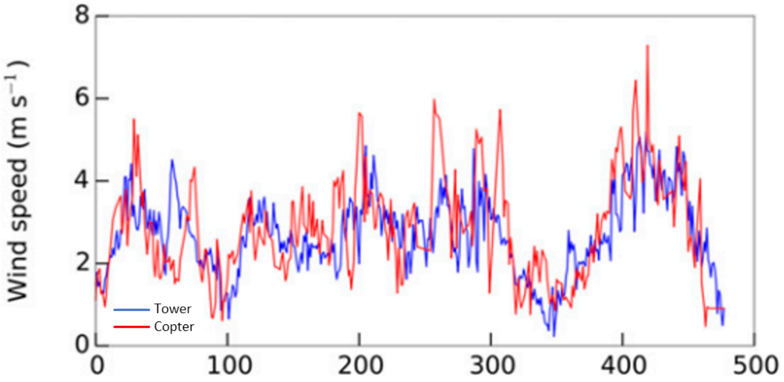

Figure 34: Decagon-2 Comparison of Wind Speed Senors with Ground Data

From these research efforts it can be hypothesized the most optimal location for the wind sensors is above the rotors on the CG of the aircraft. In this location the wind sensors are only subjected to the inflow disturbances from the rotors, as opposed to the much higher velocities of the down-wash located beneath the rotors. While this is the hypothesis for the optimal location it still needs to be verified. What is also not clear is the optimal distance for the sensors to be placed and that how that distance changes on different multi-rotors UAVs.

CHAPTER III

EXPERIMENTAL METHODS

This chapter discusses the equipment, methodology and experimental setups that are used to analyze the flow-field of multi-rotors. The first section will cover the multi-rotor fluid dynamics analyzed by from PIV experiment with the small rotors in a water tunnel. The following section will cover an experiment analyzed a single large rotor effect on ultra sonic on anemometers in ambient conditions was conducted. The last experiment analyzed the effect of a full life-size quad-copter by placing the ultra-sonic anemometer in various locations in the inflow.

3.1 PIV Experiment

The goal of this experiment is to observe the intricate fluid dynamics of multi-rotor systems. By utilizing PIV and a water-tunnel, the experiment began by analyzing a two rotor setup and then increasing it to a four rotor systems.

Equipment

A list of the electrical equipment used for the rotor system is shown below.

1. Experimental Equipment
    - Exmax MT2213-935 Kv 2212 Brushless motors
    - RC Electric Parts ESCs 30A
    - RMRC Lipo 3c Batteries 4200 maH

- Arduino Uno
- Three-Blade 3-inch Propellers
- High-Speed MotionPro Camera
- Big Sky laser

The testing apparatus that was used is the Oklahoma State University low-speed water-tunnel. The water-tunnel has a cross-sectional test area of 30x30 cm and a testing section of 1m. With a minimum operating speed of 0.009 m/s and a maximum testing speed of 1.1 m/s that is achieved by two centrifugal pumps controlled by independent variable frequency drives.

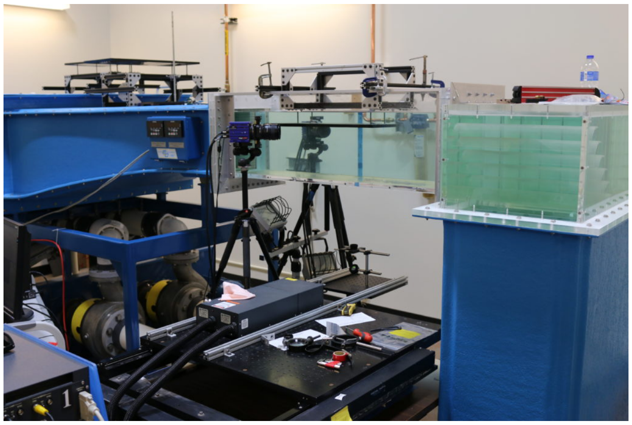

Figure 35: Rotor System

PIV Setup

The PIV setup consisted of a high-speed camera facing the test section and the rotor system. The laser generator was fasten onto a table that was located underneath along with the glass to focus the laser plane on the rotors.

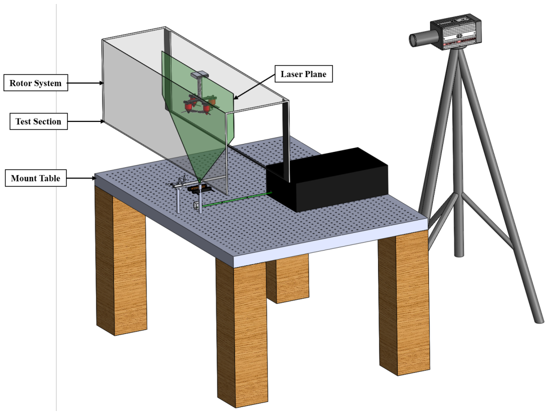

Figure 36: PIV Setup Iso-View

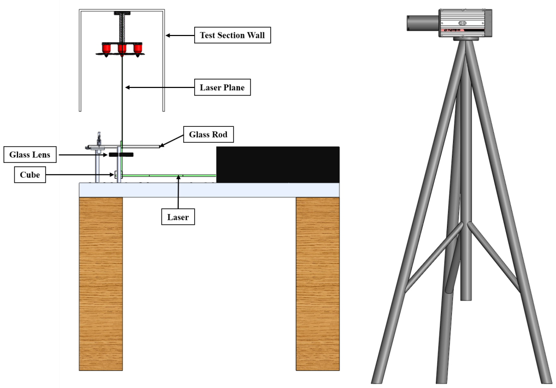

Figure 37: PIV Setup Side-View

For each test case five hundred images were captured with a 1000us exposure in double exposure mode at 1000 Hz. The frame sync is set to external mode that is triggered by the camera. The camera settings are displayed below.

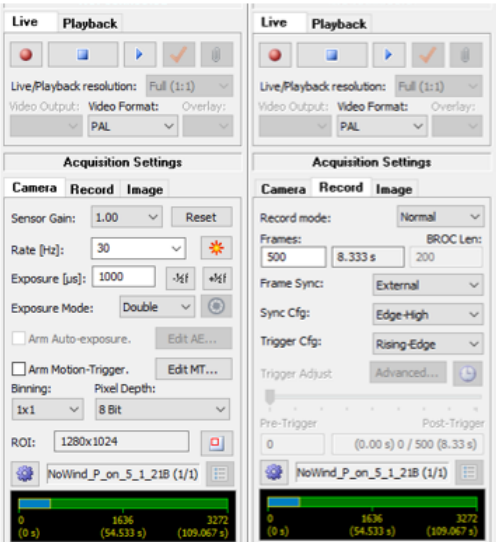

Live/Playback resolution: Full (1:1)
Video Output:
Video Format: PAL
Overlay:
Sensor Gain: 1.00
Rate [Hz]: 30
Exposure [µs]: 1000
Exposure Mode: Double
☐ Arm Auto-exposure.
☐ Arm Motion-Trigger.
Binning: 1x1
Pixel Depth: 8 Bit
ROI: 1280x1024
NoWind_P_on_5_1_21B (1/1)
0 (0 s) 1636 (54.533 s) 3272 (109.067 s)

Record mode: Normal
Frames: 500 8.333 s
BROC Len: 200
Frame Sync: External
Sync Cfg: Edge-High
Trigger Cfg: Rising-Edge
0 (0.00 s) 0 / 500 (8.33 s)
NoWind_P_on_5_1_21B (1/1)
0 (0 s) 1636 (54.533 s) 3272 (109.067 s)

Figure 38: Camera Setting

Rotor System

The rotor system is shown below. It starts with the motors being mounted upside down in the water-tunnel with the the wires ran through the top lid of the water-tunnel. The wires connect to the ESCs that are powered by the battery and controlled with a Arduino Uno. Then a computer sends a pwm signal to the Arduino that spins the motors.

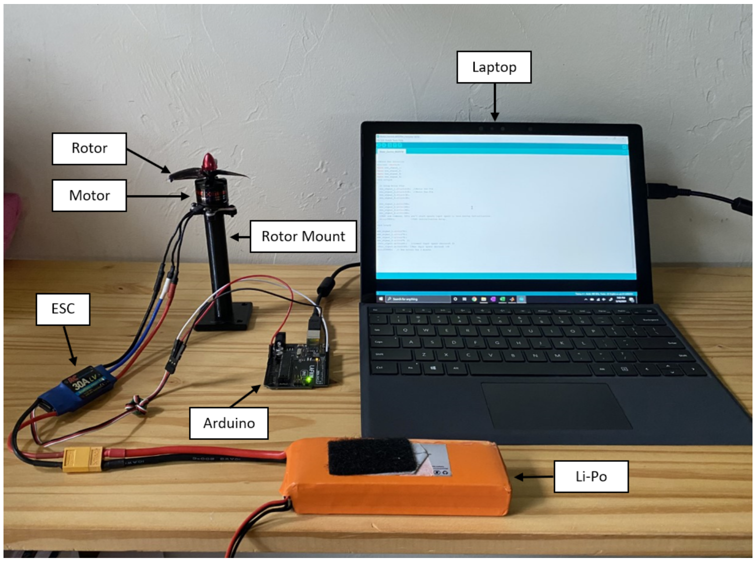

Figure 39: Rotor System

```
//Motor Run Intialize
#include <Servo.h>
Servo esc_signal_1;
Servo esc_signal_2;
Servo esc_signal_3;
Servo esc_signal_4;

void setup()
{
  // Setup Motor Pins
  esc_signal_1.attach(12);  //Motor One Pin
  esc_signal_2.attach(13);  //Motor Two Pin
  esc_signal_3.attach(4);   //Motor Three Pin
  esc_signal_4.attach(3);   //Motor Four Pin

  delay(3000);            //ESC initialization delay.
}
void loop()
{
//Send PWM to Motors
esc_signal_1.write(75);
esc_signal_2.write(75);
esc_signal_3.write(75);
esc_signal_4.write(75);
}
```

Figure 40: Arduino Motor Code

The rotors used are the 3052 3-blade propellers by Gemfan. These rotors were chosen because of their size and strength that allowed them to be smallest rotors able to be used to in the water tunnel. Smaller rotors of two, one and half inch diameter were experimented with but they were to fragile for extensive use in the water tunnel and broke after a few uses.

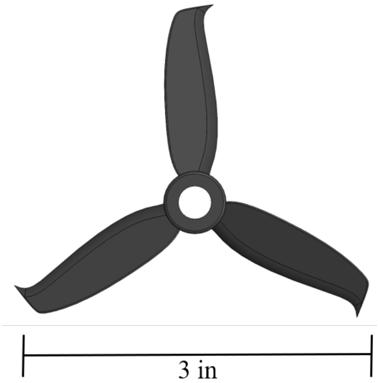

Figure 41: Three-Blade Propellor

Rotor Test Configurations

Each rotor test configurations consisted of a 3d-printed mount. The base of each mount was 4in and 3/4in, this plus the added 2in from the motor, places the rotor in the middle of the test section. Each rotor mount consists of 2x2in base. The brushless motors attach to the top of the mounts. There were eleven mounts in total. Each mount is fastened to the top lid of the water-tunnel by sliding them into a bracket that was adhered to the acrylic lid of the water tunnel with adhesive tape. This setup results in the motor system being upside down. This is allows the ESCs wires connecting the motors to be kept out of the inflow of the motors. The mounting bracket makes it easier to change from one mount to the next during testing.

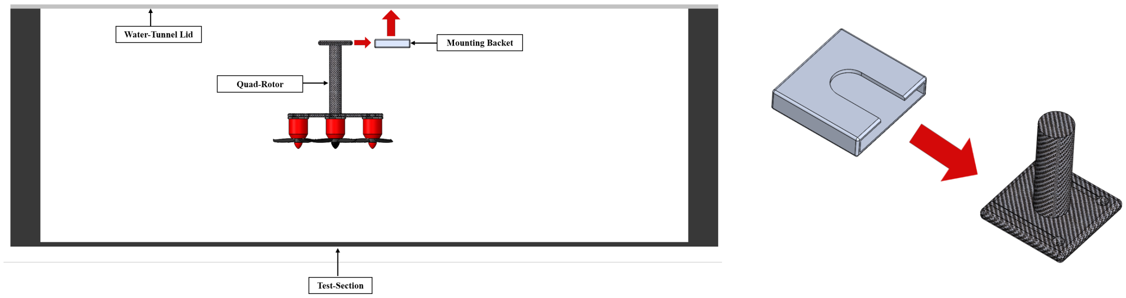

Figure 42: Left.) Test Section, Right.) Mounting Bracket

There are four main sets of rotor configurations, dual-rotor perpendicular, dual-rotor parallel, quad-rotor plus-configuration, quad-rotor x-configuration. Each rotor configurations was selected to observe different characteristics of multiple rotor systems. The dual rotor parallel configurations has its two rotor positioned parallel with the test section of the water-tunnel this allows the interactions in-between the two rotors to be observed. The dual rotor perpendicular configurations has it two rotor positioned perpendicular with the test of the water tunnel this allows a single rotor to be observed at time. Moving up the to the quad-rotor systems the x and plus configuration were chosen because these are the these be the most popular configurations for quad copter systems.

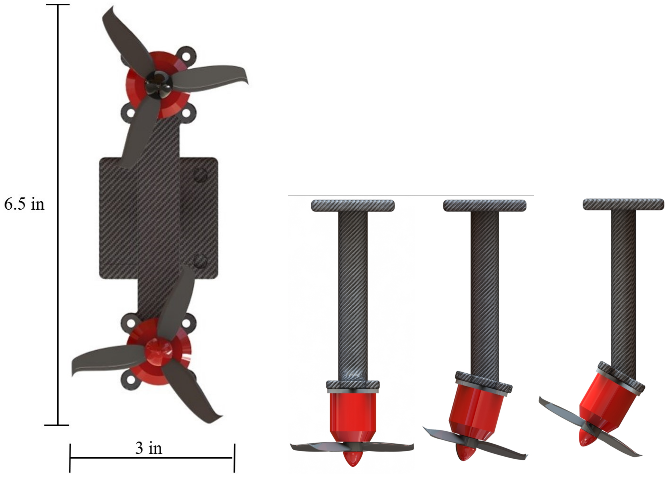

Figure 43: Left.) Dual Perpendicular Top View, Right.) Dual Perpendicular Front View

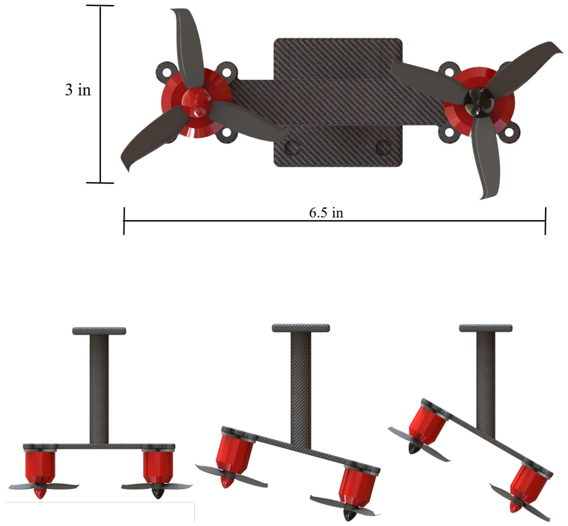

Figure 44: Top.) Dual Parallel Top View, Bottom.) Dual Parallel Front View

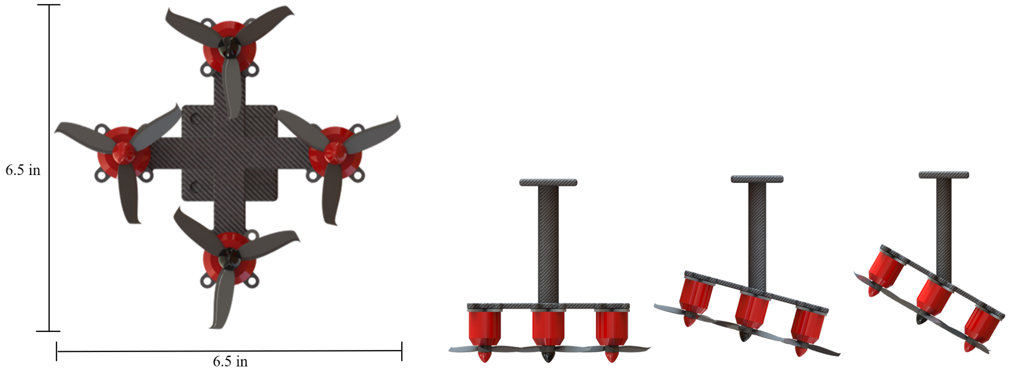

Figure 45: Left.) Quad Plus Top View, Right.) Quad Plus Front View

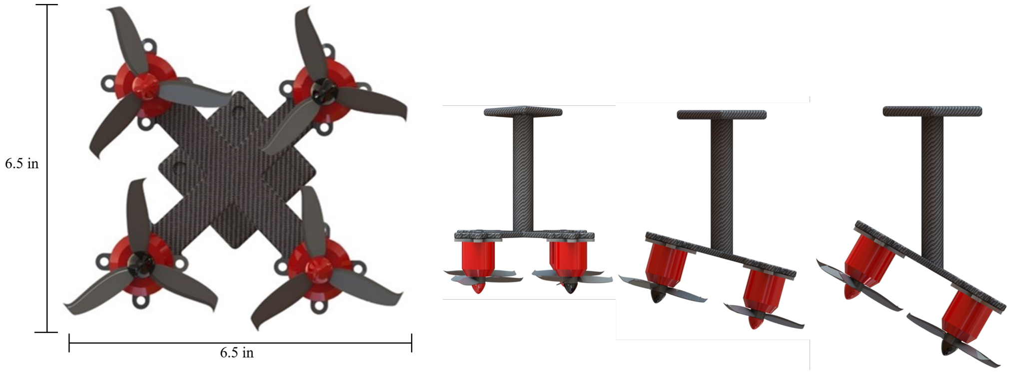

Figure 46: Left.) Quad X Top View, Right.) Quad X Front View

Laser Plane Locations

To examine the rotor flow, the laser was positioned underneath the test section and parallel with the water-tunnel. As the flow-field is dynamic and changes depending on the location of the length of the blade. The laser plane was positioned on different locations along the rotor system. For the dual rotor test there are two testing configurations. One with the rotors parallel to the flow and one with the them perpendicular to the flow. These tests were conducted to be compared to the quad rotor tests. For the perpendicular dual rotor tests the laser positions are: tip, hub, and mid-plane. For parallel rotor the laser positions are: tip, mid-blade, and hub. For the quad rotor tests the laser positions: tip, hub, and mid-plane. The laser is positioned only on one side of each test configuration as each system is symmetrically the rotor flow should mirror the other. By only observing one side of the system cuts down on the number of laser positions required reducing the testing time.

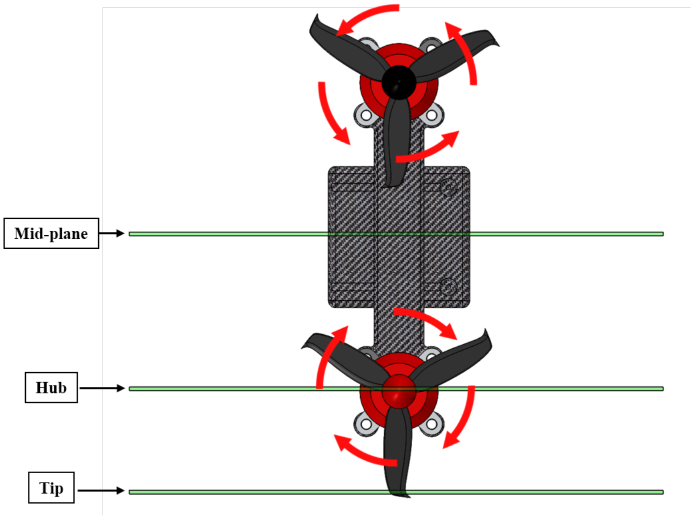

Figure 47: Dual Perpendicular Laser Positions

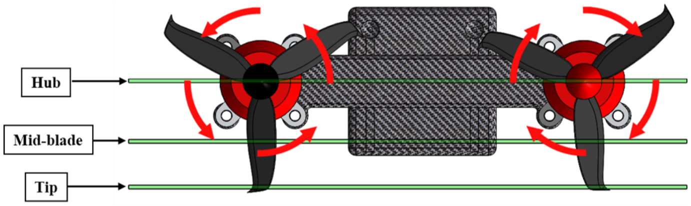

Figure 48: Dual Parallel Laser Positions

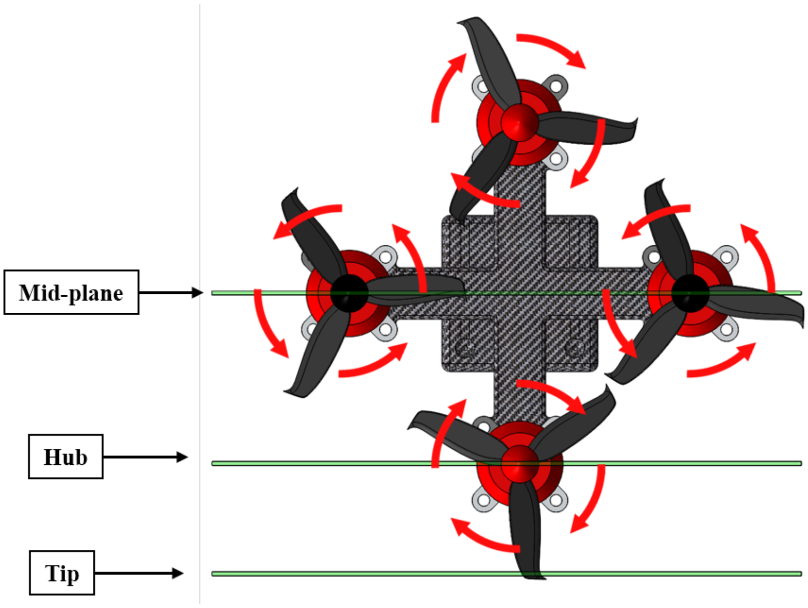

Figure 49: Quad Plus Laser Positions

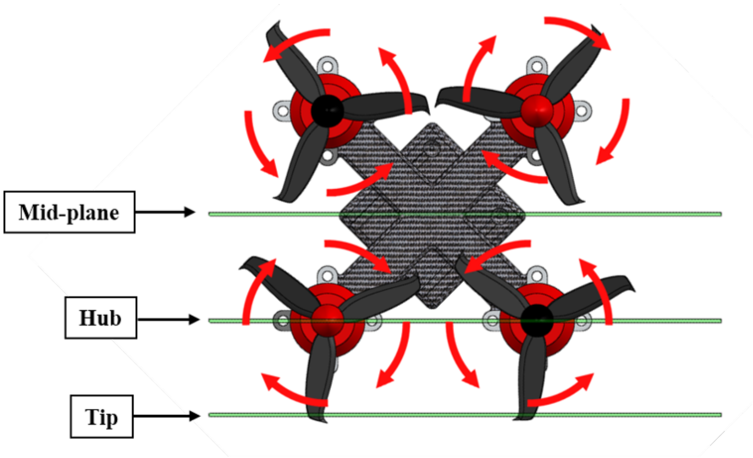

Figure 50: Quad X Laser Positions

Testing Matrix and Parameters

For the test matrix, the goal was to examine the effects of the number of rotors, rotor angle, and cross-flow speed. Besides testing the different number of rotors, there are two main parameters that were varied to observe their changing effects on the inflow. The first parameter varied is the flow-speed of the water tunnel. Flow speed was set at both ambient (0 m/s) and 0.5 m/ to simulate rotors flying through a cross-wind. By setting the water tunnel to (0.5 m/s) this is equal to a Reynolds number [25] of 150,000 which is roughly equal to a multi-rotor traveling (10 m/s) though the air. This is average speed that can be achieved by most multi-rotors on the market. [31]

$$Re = \frac{\rho \cdot L}{\mu} \tag{3.1.1}$$

The second parameter varied is the angle of the rotor system. To simulate a multi-rotor in hover the rotor system was set 0°. As explained in the chapter 2 to move forward through the air the multi-rotor is titled forward at two different angle of 15°and 30°

The rotor RPM were kept constant throughout the tests. The rotor RPM the system was able to achieve speeds of 0-1000RPM. By using the Reynolds number equation for propellers an RPM of 900 was selected. This is equal to a Reynolds number [8] of 3,500 in water. This value is equal to the rotors rotating at roughly 10,000 RPM in air which the average velocity of these motors. The equations used for Reynolds and motor RPM are shown below.

$$Re = \frac{r \cdot \frac{RPM \cdot 2\pi}{60} \cdot D \cdot C}{\mu} \tag{3.1.2}$$

$$UnloadedRpm = Kv \cdot V \tag{3.1.3}$$

With those set parameters in place, a testing matrix was created shown below. In total there are 72 cases in all. The testing was completed over several weeks in the water-tunnel.

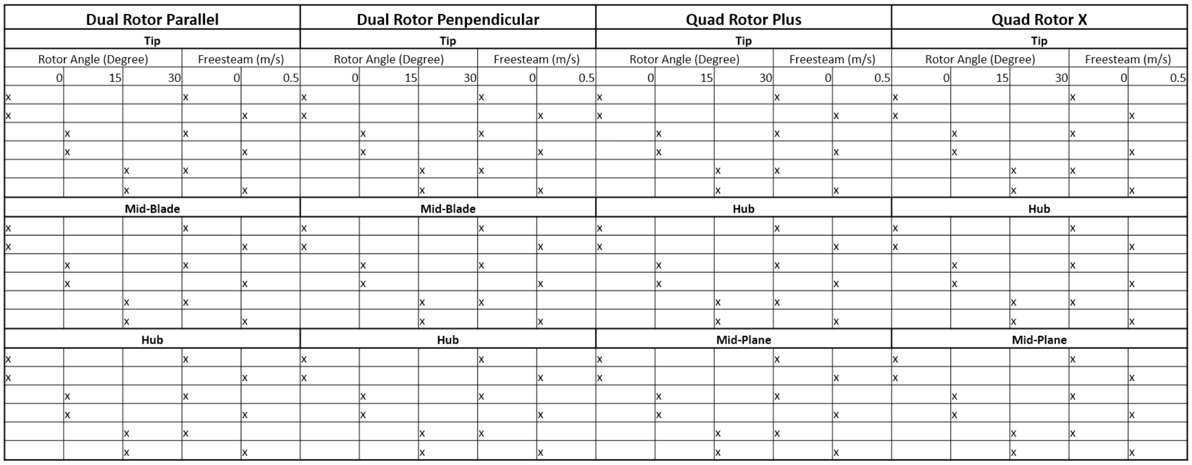

Dual Rotor Parallel					Dual Rotor Penpendicular					Quad Rotor Plus					Quad Rotor X				
Tip					Tip					Tip					Tip				
Rotor Angle (Degree)			Freesteam (m/s)		Rotor Angle (Degree)			Freesteam (m/s)		Rotor Angle (Degree)			Freesteam (m/s)		Rotor Angle (Degree)			Freesteam (m/s)	
0	15	30	0	0.5	0	15	30	0	0.5	0	15	30	0	0.5	0	15	30	0	0.5
x			x		x			x		x			x		x			x	
x				x	x				x	x				x	x				x
	x		x			x		x			x		x			x		x	
	x			x		x			x		x			x		x			x
		x	x				x	x				x	x				x	x	
		x		x			x		x			x		x			x		x
Mid-Blade					Mid-Blade					Hub					Hub				
x			x		x			x		x			x		x			x	
x				x	x				x	x				x	x				x
	x		x			x		x			x		x			x		x	
	x			x		x			x		x			x		x			x
		x	x				x	x				x	x				x	x	
		x		x			x		x			x		x			x		x
Hub					Hub					Mid-Plane					Mid-Plane				
x			x		x			x		x			x		x			x	
x				x	x				x	x				x	x				x
	x		x			x		x			x		x			x		x	
	x			x		x			x		x			x		x			x
		x	x				x	x				x	x				x	x	
		x		x			x		x			x		x			x		x

Figure 51: Test Cases

Data Processing and Procedures

The procedures of the experiment are relatively straightforward. The rotor system setup was mounted to water-tunnel lid, the laser system was turned on to fire in time with the camera and double exposure mode, the camera was turned on, and set to record 500 frames in 8 seconds. The tunnel was turned on and ran up to speed and allowed to reach steady-state for five minutes. The motors wwere ran for 60 seconds to reach steady-state and then the camera will record the data. The footage was reviewed before moving onto the next test case.

Once the tests were completed, the data was processed in DaVis. The raw 500 images are imported into DaVis. A subtract average is used to remove similar particles in each image. Then the a mask is put over the rotor system. The average and standard deviation was calculated of each test case. Finally, the data was imported into matlab and the U and V velocities are extracted and plotted.

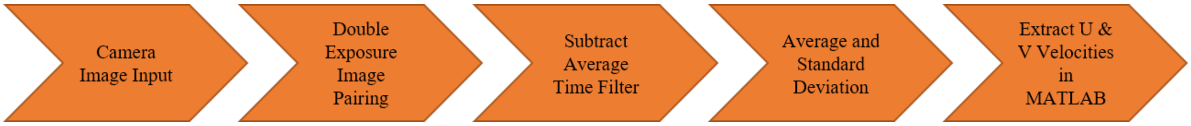

Figure 52: PIV post-processing flow chart

Uncertainty Sources

Throughout this PIV experiment several sources of uncertainty were discovered. First, the motor controller, the arduino uno that pushed the pmw signals to the brushless motors has standard deviation in the voltage signals of $\pm 1\%$. Experimental uncertainties can come from many places in the PIV. The seeding particles in the water tunneling could have not been evenly distributed causing some data sets to turn out poorly. Reflections from the spinning rotor blades themselves may have blinded the camera on certain frames. The propellers were painted black to help prevent this but the reflection still occurred on some tests runs. The testing took place over a course of two weeks where the brushless motors were continuously placed in water. While the motors could still run in water, corrosion can still set in slowing the rpm of the motors. The motor rpm was routinely examined with the high-speed camera, it was determine motor rpm had a standard deviation 5-10 rpm. The optics and glassed pieces used to focus and spread the laser plane can slowly become clouded and dirty from use which also may have impacted the results. There is also the wall effects from the water tunnel side walls. This was avoid as much as possible by reducing the size rotor system size to half of the test section. There are also certain algorithmic uncertainties that exist due to DAVIS calculating velocities from pixels conversion. Overall each data set's correlation coefficient was examined to ensure the accurate data acquisition from the PIV system and to show how accurate the PIV was tracking the seeded particles. An example image of the correlation coefficient for a test is shown below. Keep in mind this is image only shows the values for a single frame for each test set and test set has 500 frames . Another indication of the quality of the data can be observed by looking at the cross-stream average velocity. Because the water-tunnel is ran at constant 0.5 m/s all of the cross-stream tests should have an average velocity of 0.5 m/s, especially around the outside edges of the frame away from the influence of the rotors.

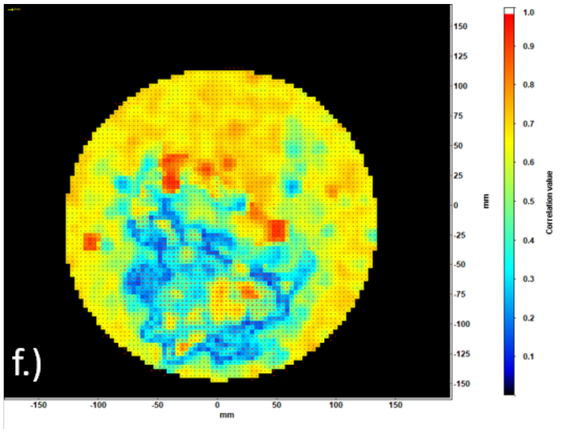

Figure 53: Correlation Coefficient Dual Parallel Hub

Davis was unable to average the values down to a single frame and of correlation coefficients. As this tests were conducted over steady-state system the correlation coefficients values stay relatively the same for each test, a correlation coefficient image for each test can be found in the appendix.

3.1.1 Single Rotor Test

After investigating the multi-rotor in the water tunnel, experiments were conducted to examine the effect of rotors on wind sensors directly. The first experiment was over a single m600 rotor in controlled ambient conditions. The goal of this study was see how far an ultra sonic anemometer would have to be placed above rotor before it is no longer effected by the rotor inflow. The equipment used for this experiment is the “FT205 Sonic Anemometer” and m600 rotor. The specifications are shown below.

Figure 54: FT205 Anemometer

Table 1: FT205 Sensor Specifications

Range	0-75 m/s
Resolution	0.1 m/s
Accuracy	± 0.3 m/s
Direction Range	0°- 360°

A single DJI m600 arm was mounted statically in a high ceiling chamber. Then the FT was mounted on a movable boom arm and used to sample the flow. The rotor system itself consisted of DJI's 2170 carbon fiber folding propeller, 2200 mah 3c li-po battery, and servo tester. The samples were taken horizontally and vertically centered above the rotor.

Figure 55: DJI 2170 Rotor

The rotor was chosen become it is a common size for most heavy lift multi-rotors. Establishing a base of idea of the inflow velocities for a single rotor would give a good indication of what the inflow for a typical multi-rotor system would look like. The diagram below shows the experimental setup. The rotor was extended out from a evaluated work table on an arm. The table was used to move the system around and keep the rotor away from its own wash from the floor.

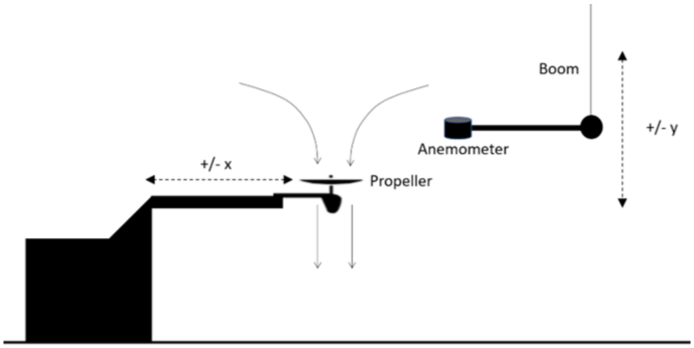

Figure 56: Single Rotor Experiment Diagram

Below is a picture of the experiment. The sensor was mounted to a hanging boom by PVC pipe and tape. The metal boom can lift itself up and down by a pulley system on the ceiling. The m600 arm was mounted to the work table by an 80/20 frame. The carbon frame pole was then attached to the 80/20 frame by metal brackets. The batteries and motor wires were strung along the mounting pole with the battery, motor, and servo controller fastened to the table.

Figure 57: Single Rotor Experiment

The rotor was moved along x axis and started at 1 meter away from the sensor. The rotor was then turned on via pmw controller at 1300 pwm and the velocities was recorded. Once the test was done the sensor moved 0.1 m closer to the sensor and the test was repeated again, until the rotor was 1 meter on the other side of the sensor. Once this was completed the sensor boom was moved up several cm and the tests were repeated again. The vertical heights tested were 20 through 48 cm.

Uncertainty Sources

For this experiments a couple of sources of uncertainty should be mentioned. First, the sensor itself has ± accuracy of the 0.3m/s. The pmw controller that pushed the voltage signals has a standard deviation of 1±% which result in small rpm changes from each test to the next.

3.1.2 Flight Tests

The single rotor test examined the inflow of single rotor in static ambient conditions. The next experiment examines the effect of the inflow of a heavy lift multi-rotor quadcopter on a ultra-sonic anemometer in a real environment. By mounting a wind sensor to a custom built quad and flying the system next to a meteorology tower and comparing the wind data from the system to the tower sensor the effect of the inflow can be determine. Using information gained from the previous experiments nine mounting locations were chosen. By evaluating the data from nine positions the optimal placement for heavy lift multi-rotors was determine.

Sensors

The sensors chosen for this experiment were the Trisonica mini mounted to the quadcopter and a Young 9200. The sensor were chosen due their similarity in resolution and ease of use.

Figure 58: Trisonica Mini

Table 2: Trisonica Mini Specifications

Weight	50 g
Range	0 - 50 m/s
Resolution	0.1 m/s
Direction Dimensions	2D
Frequency	4 Hz

Figure 59: Young 9200

Table 3: Young 9200 Specifications

Weight	700 g
Range	0 - 70 m/s
Resolution	0.01 m/s
Direction Dimensions	2D
Frequency	4 Hz

To ensure the systems were in good agreement with each other the sensors were setup outside next to each other and allowed to collect data for one minute. Three tests were conducted, one with the sensors enclosed by a building to simulate mostly ambient conditions, the second test was conducted in the open with a slow steady cross stream of wind, and the third test was conducted at the Oklahoma State University airfield in higher wind speed. The range of wind speeds tested ensured that the sensors remained consistent over a range of speeds for testing.

Figure 60: Sensor Comparison Test 1

Figure 61: Sensor Comparison Test 2

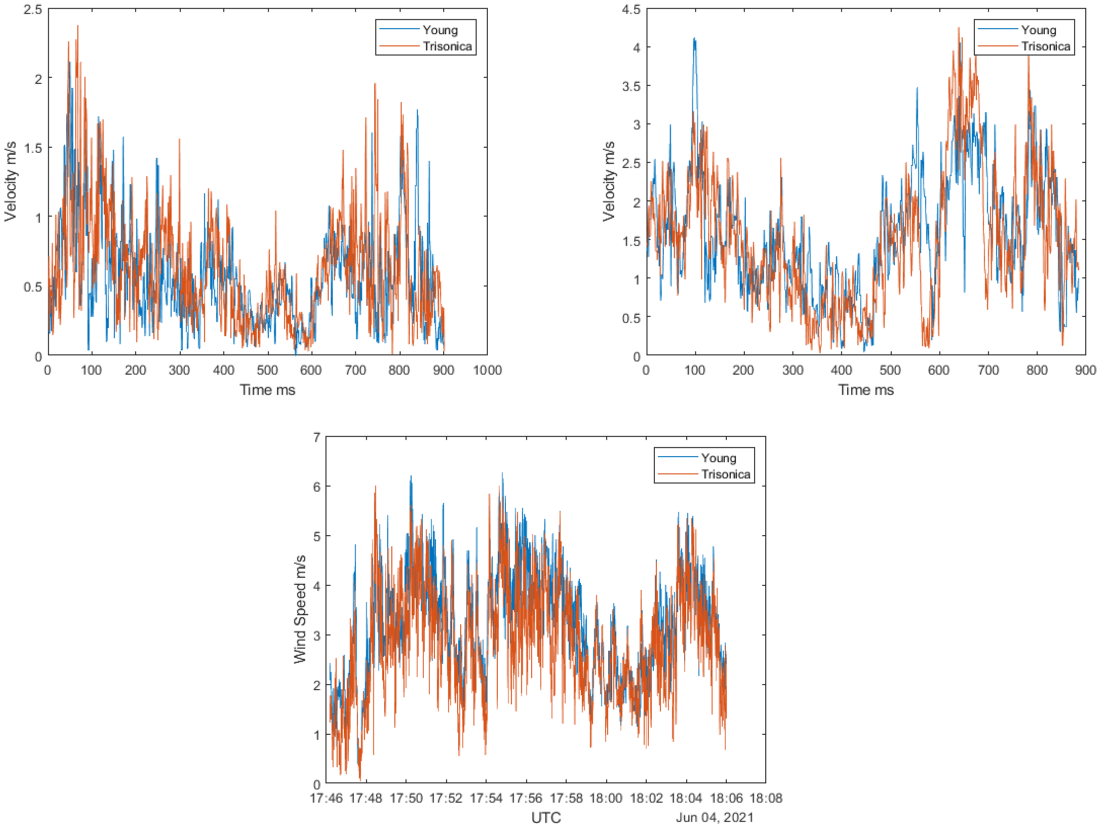

Figure 62: Left: Test 1 Right: Test 2 Bottom: Test 3

Table 4: Comparison Test Results

Statistics	Test 1	Test 2	Test 3
Young Avg. m/s	0.57	1.58	3.23
Trisonica Avg. m/s	0.63	1.52	2.83
Avg. Diff	0.06	0.06	0.40
RMSE	0.42	0.68	0.68
Correlation Coefficient	0.42	0.66	0.75

The results show the sensors are in fairly good agreement with each other. With a root mean squared error of less then 0.7 m/s and fairly strong correlation coefficient for each test.

Multi-Rotor System

The multi-rotor system used is the SKB-1000 an electric powered quad-copter in the H - configuration. That was custom built at USRI out carbon fiber and plywood. Designed to carry heavy sensitive payloads, the system was chosen for this research due to its lift capabilities and it ease of mounting and integration's.

Figure 63: SKB-1000

Table 5: SKB-1000 Specifications

Battery	6c 22,000 Mah
Motors	320 kV
Propellers	20in
Flight Time	20 mins
Payload Capacity	6 lb
ESCs	80A

The payload can be mounted atop of the SKB. The payload consisted of the Trisonica mini, a lipo battery to power it, a Pixhawk flight controller to get GPS time stamp. The data acquisition system consisted of Arudino Teenzy that was connected to the Trisonica sensor. The data was logged on a micro SD card and the data was pulled. The code for both the Trisonica and Young are shown in the appendix.

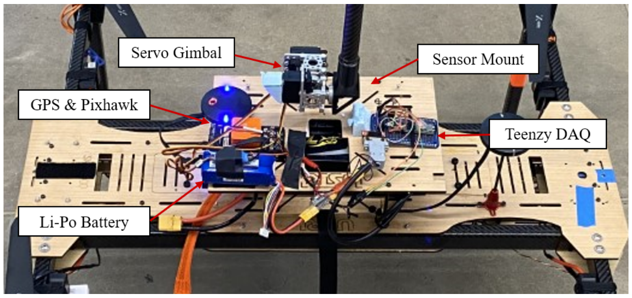

Figure 64: SKB Payload Diagram

Finally the Trisonica is mounted to a 2-axis gimbal. The gimbal system is located on top of the SKB platform composed of the 9g two servo motors. The servo motors were controlled by a pix-hawk orange cube and by using the mission planner ”camera gimbal” plugin the system balances the movement of the SKB-1000 to keep the sensor level during flight.

Figure 65: SKB Gimbal

Test Cases

Using the data from the previous experiments three locations were chosen for the sensor placement. Front, middle and back, along the center line of the SKB.

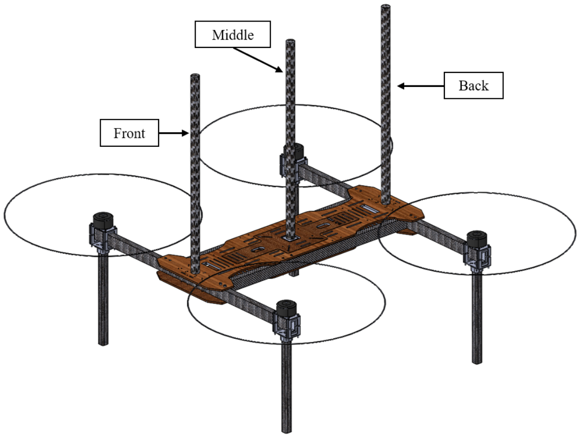

Figure 66: Sensor Positions

With the three positions chosen each position was tested at three vertical heights, 24 in, 20in, 16in. The heights were chosen from knowledge gained from previous experiments and recommendations of the ultra-sonic sensor manufactures. The mounts were made using 1 in diameter carbon fiber tubing and a 3d printed mount to fasten to the gimbal.

Figure 67: Mounting Poles

With those parameters there are nine tests cases in total.

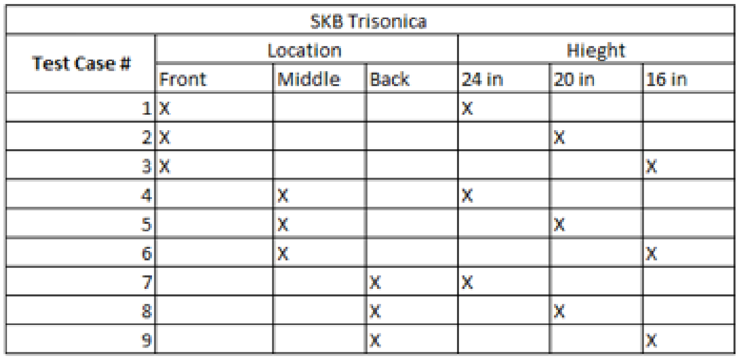

SKB Trisonica						
Test Case #	Location			Hieght		
	Front	Middle	Back	24 in	20 in	16 in
1	X			X		
2	X				X	
3	X					X
4		X		X		
5		X			X	
6		X				X
7			X	X		
8			X		X	
9			X			X

Figure 68: Mounting Poles

Experiment Setup

With the SKB setup the experiment took place outside next the URSI lab. Using a 30ft tower, the Blue Sky Mast the Young 9200 was mounted to the top of 30 ft tower. The SKB was flown up to level with the sensor and about 30 ft away from sensor and positioned in the same direction as the tower sensor. Data was collected for three minutes for each test case then the SKB was down and the next test was setup.

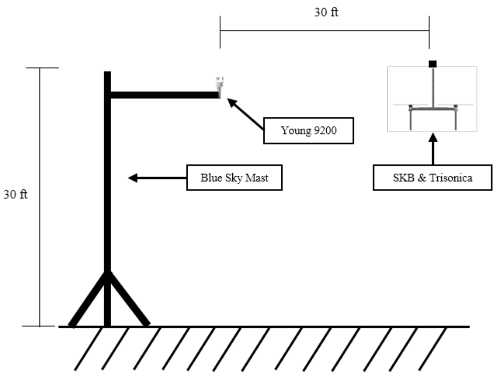

Figure 69: Tower Comparison Test

Data Processing

The data was captured on microSD card and imported to Matlab for data processing. As the data for each sensor was recorded differently there were a few steps to the processing. First the Young time was converted from UTC time to unix time to match the Trisonica time. Then the because the Trisonica data was recorded faster, the missing time points are interpolated. Finally, because the two data are slightly different sizes the Trisonica times are matched to their nearest Young time to make each data set the same size. There is only a slight offset in time between the two data sets. This offset was calculated to be on average 0.1 seconds.

Figure 70: Sensor Data Processing

Uncertainty Sources

There are several sources of uncertainty for this experiment that should be mentioned. First, the sensors are not completely the same as each even though comparison proved the sensors are very similar to each other. Also, the two-axis gimbal system used to balance the trisonica mounted to SKB also could introduce errors in the recorded data. Especially, during fast gusts of wind that system has to react to. There are also inherit errors that are introduced in MATLAB during the data processing, such as interpolating the time values for the Trisonica sensor. Additionally, when matching the time values of the sensors together there is an average 1ms difference between each data points. Furthermore, while the SKB was in qloiter mode to hover in place during the tests but there it has unavoidable drift that causes the SKB to move several inches during the duration of the tests. There is the variability of the wind as the test were conducted over the three days and so wind speed was not consistent as it would be in controlled environment. Finally, there is the mounting arm that is holding the Young sensor. It is not fastened in place and allows for small movements witch will also introduced errors into the sensor.

CHAPTER IV

RESULTS

This chapter will go through results from each of the experiments. Starting with the PIV experiment then moving onto single rotor test and finishing with the flight test experiment.

4.1 PIV Experiment

4.1.1 Inflow Velocities

Starting the inflow velocities with the dual parallel tests 0 degree, the hub position showed the highest velocity of the tests. From the images the inflow can be observed above the rotors getting pulled down in the the spinning blades. In between the two rotors there is a small dead region. Additionally, it can be observed in the cross-stream data sets that average velocity is around 0.5 m/s. This speed matches with the set velocity of the water tunnel and indicts that the data is accurate. This indicator can be observed in almost every data set in the cross-stream tests.

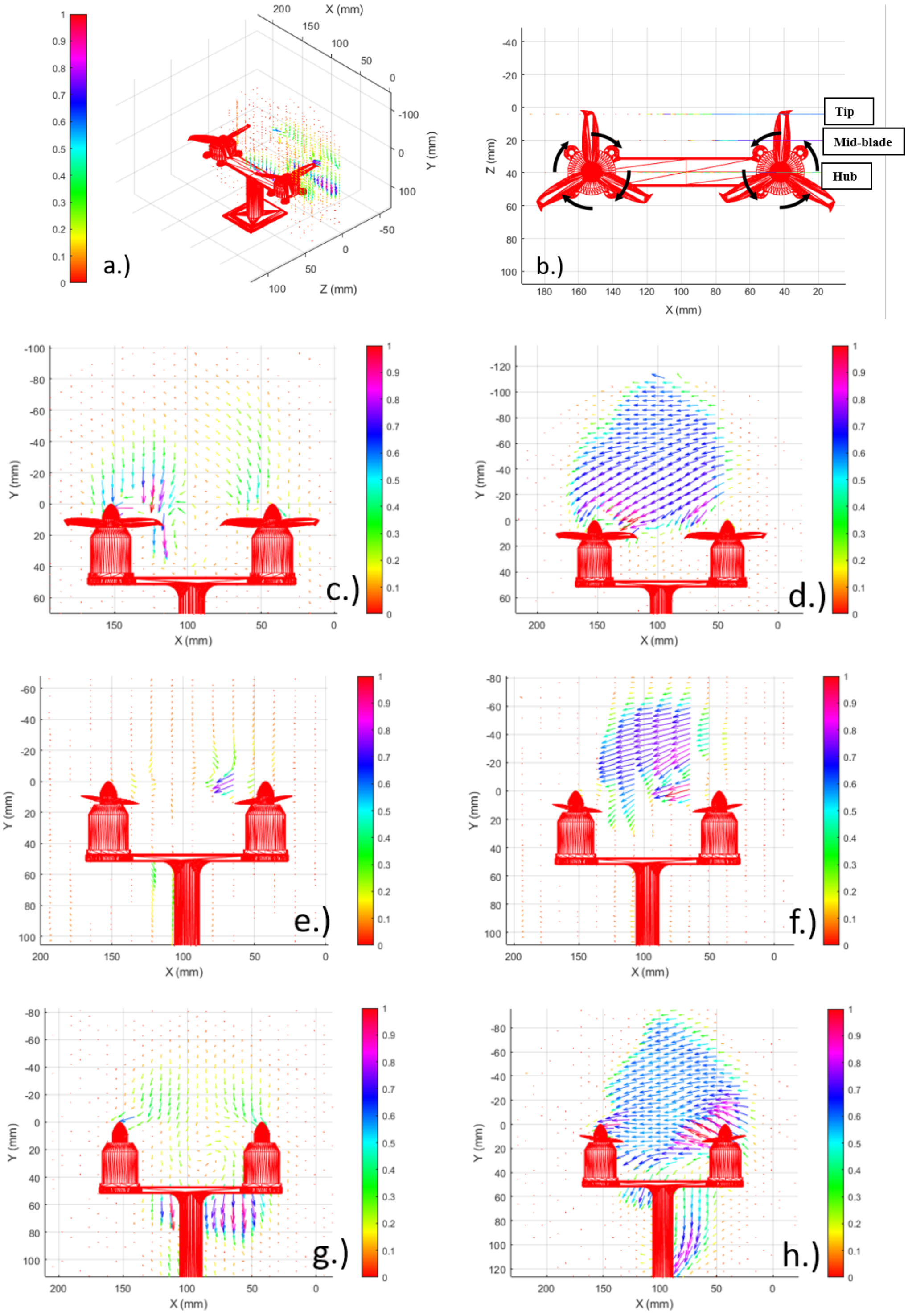

Figure 71: Inflow Velocity Field: Dual Parallel 0°: a.) 3D-View b.) Top-View c.) 0m/s Hub d.) 0.5m/s Hub, e.) 0m/s Midblade f.) 0.5m/s Midblade g.) 0m/s Tip h.) 0.5m/s Tip

For the 15 degree tests the inflow characteristics stay relatively the same as the 0 degree tests but the inflow tests are shifted slightly upwards.

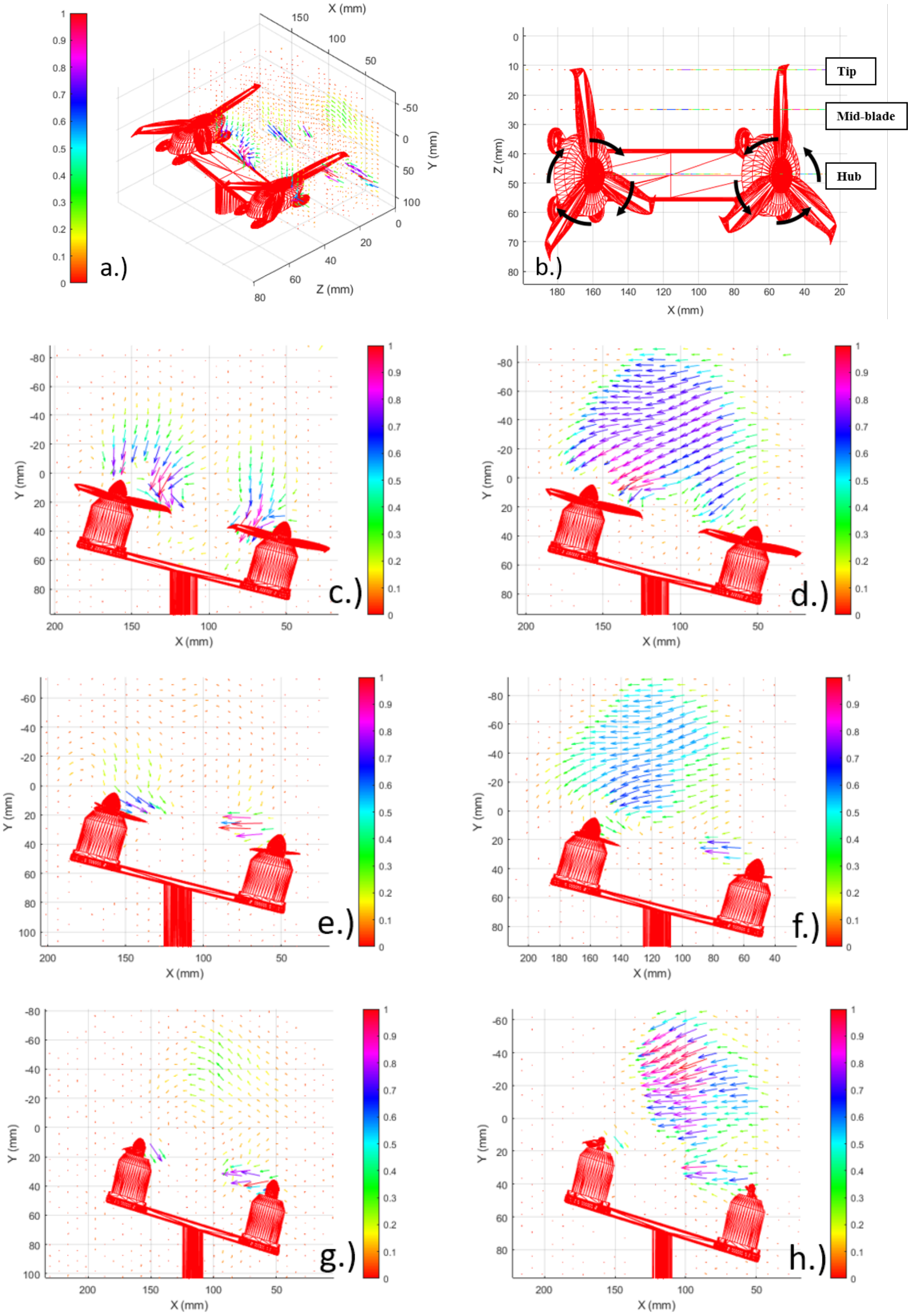

Figure 72: Inflow Velocity Field: Dual Parallel 15°: a.) 3D-View b.) Top-View c.) 0m/s Hub d.) 0.5m/s Hub, e.) 0m/s Midblade f.) 0.5m/s Midblade g.) 0m/s Tip h.) 0.5m/s Tip

For the 30 degree tests the flow characteristics showed similar patterns to the 15 degrees tests but with the increased angle the angle of the flow increases.

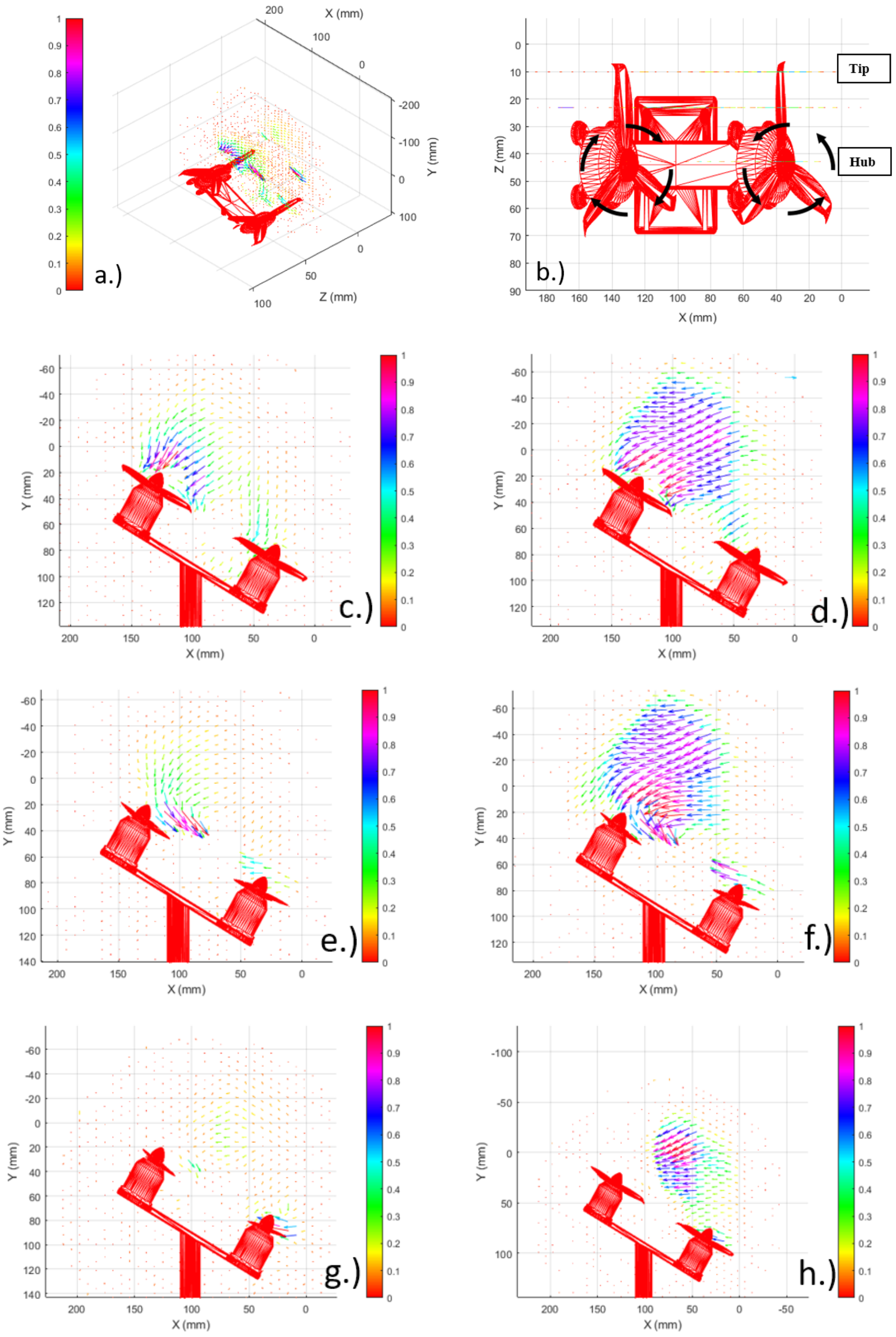

Figure 73: Inflow Velocity Field: Dual Parallel 30°: a.) 3D-View b.) Top-View c.) 0m/s Hub d.) 0.5m/s Hub, e.) 0m/s Midblade f.) 0.5m/s Midblade g.) 0m/s Tip h.) 0.5m/s Tip

Moving onto the dual perpendicular tests the midplane tests showed the lowest velocities, this makes sense as the midplane position is in-between the two rotors confirming the hypothesis of the velocities decreasing between rotors.

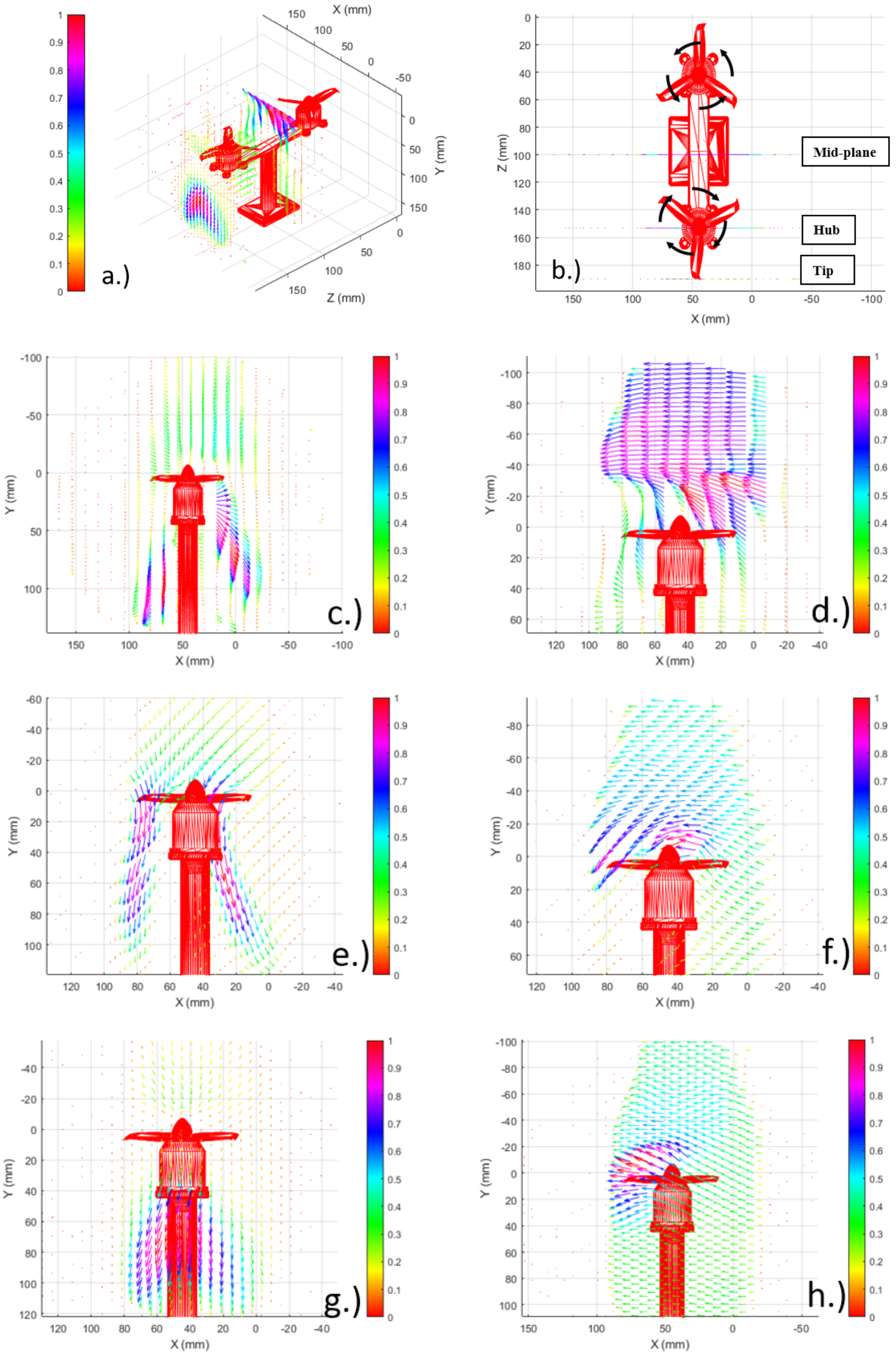

Figure 74: Inflow Velocity Field: Dual Perpendicular 0°: a.) 3D-View b.) Top-View c.) 0m/s Midplane d.) 0.5m/s Midplane, e.) 0m/s Hub f.) 0.5m/s Hub g.) 0m/s Tip h.) 0.5m/s Tip

The 15 degree showed, followed the same patterns as the 0 degree tests but with flow angle 15 degrees with the motor.

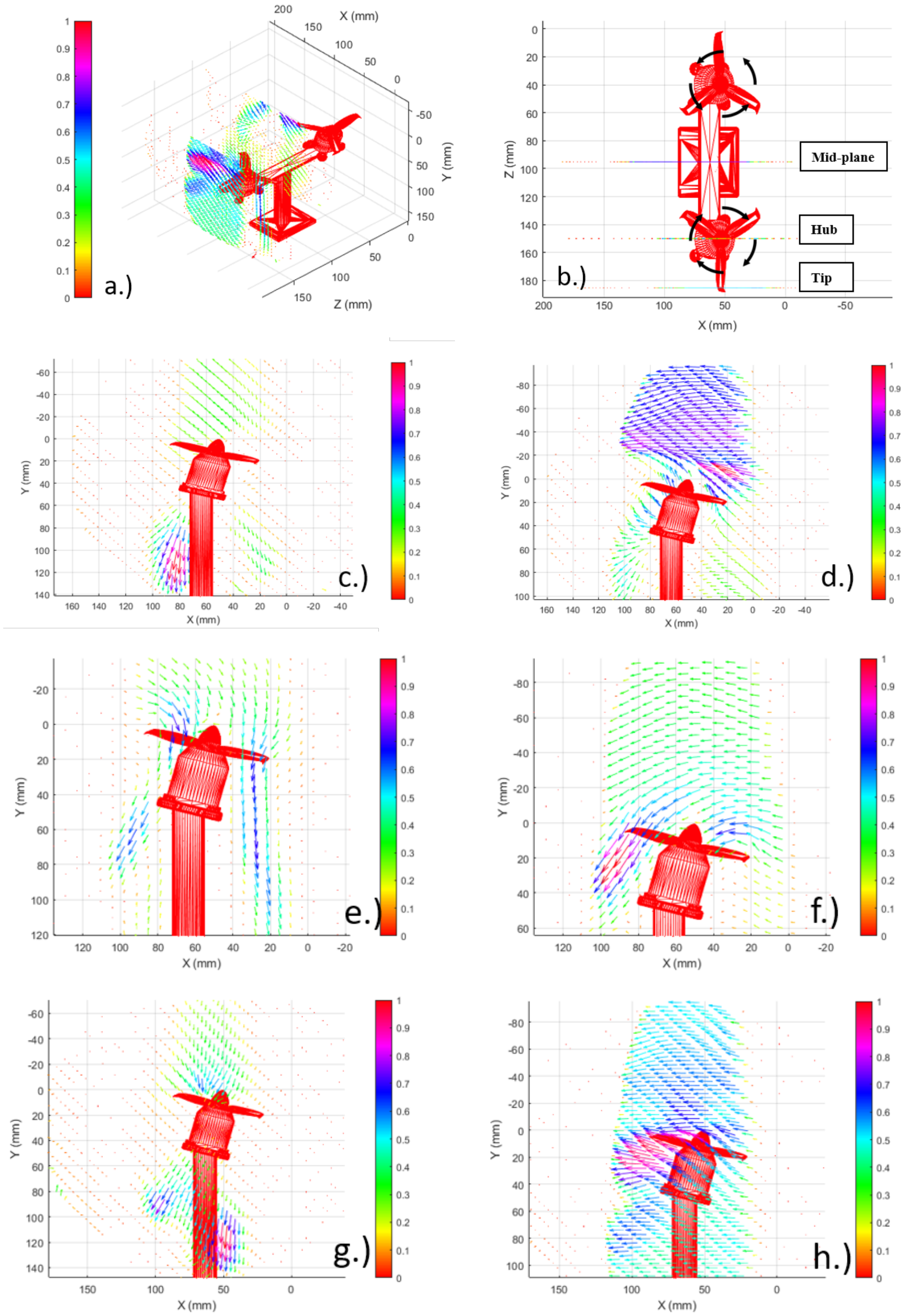

Figure 75: Inflow Velocity Field: Dual Perpendicular 15°: a.) 3D-View b.) Top-View c.) 0m/s Midplane d.) 0.5m/s Midplane, e.) 0m/s Hub f.) 0.5m/s Hub g.) 0m/s Tip h.) 0.5m/s Tip

Again the 30 degree followed the same patterns as the previous tests but with more increased in flow angle.

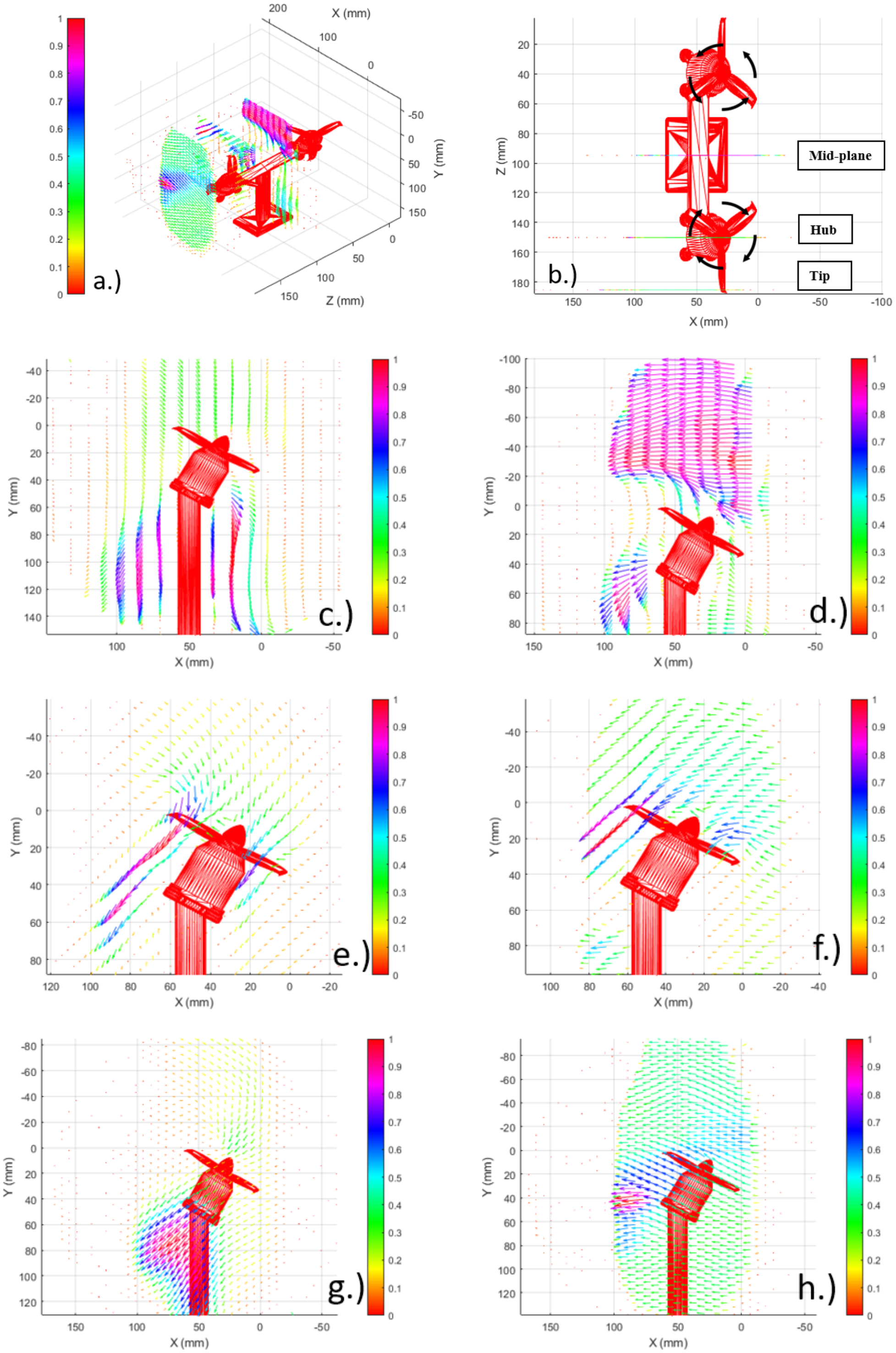

Figure 76: Inflow Velocity Field: Dual Perpendicular 30°: a.) 3D-View b.) Top-View c.) 0m/s Midplane d.) 0.5m/s Midplane, e.) 0m/s Hub f.) 0.5m/s Hub g.) 0m/s Tip h.) 0.5m/s Tip

For the Quad rotor X-configuration in hover placement the mid-plane position shows very little inflow velocity as it is similar to the midplane position from the perpedicular tests. The hub tests shows the greatest inflow induction in the center of the system. The tip cases show the inflow affected at the hub of the trailing motor where the flow reverses backwards.

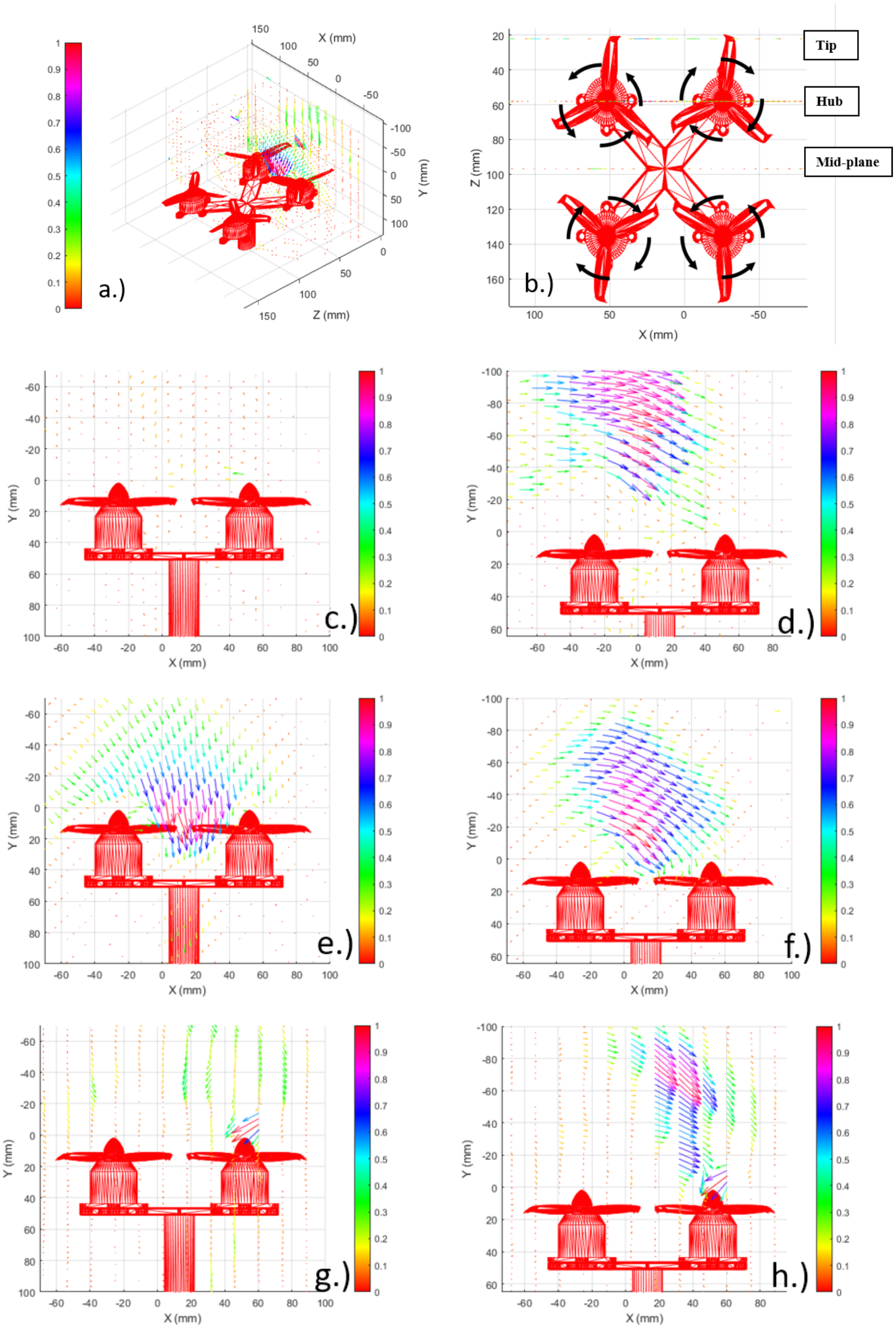

Figure 77: Inflow Velocity Field: Quad Rotor X 0°: a.) 3D-View b.) Top-View c.) 0m/s Midplane d.) 0.5m/s Midplane, e.) 0m/s Hub f.) 0.5m/s Hub g.) 0m/s Tip h.) 0.5m/s Tip

For the Quad rotor X-configuration in 15 degrees the mid-plane again showed very little inflow velocity. The hub inflow was again greatest at the center. The tip however showed almost no effect on the inflow.

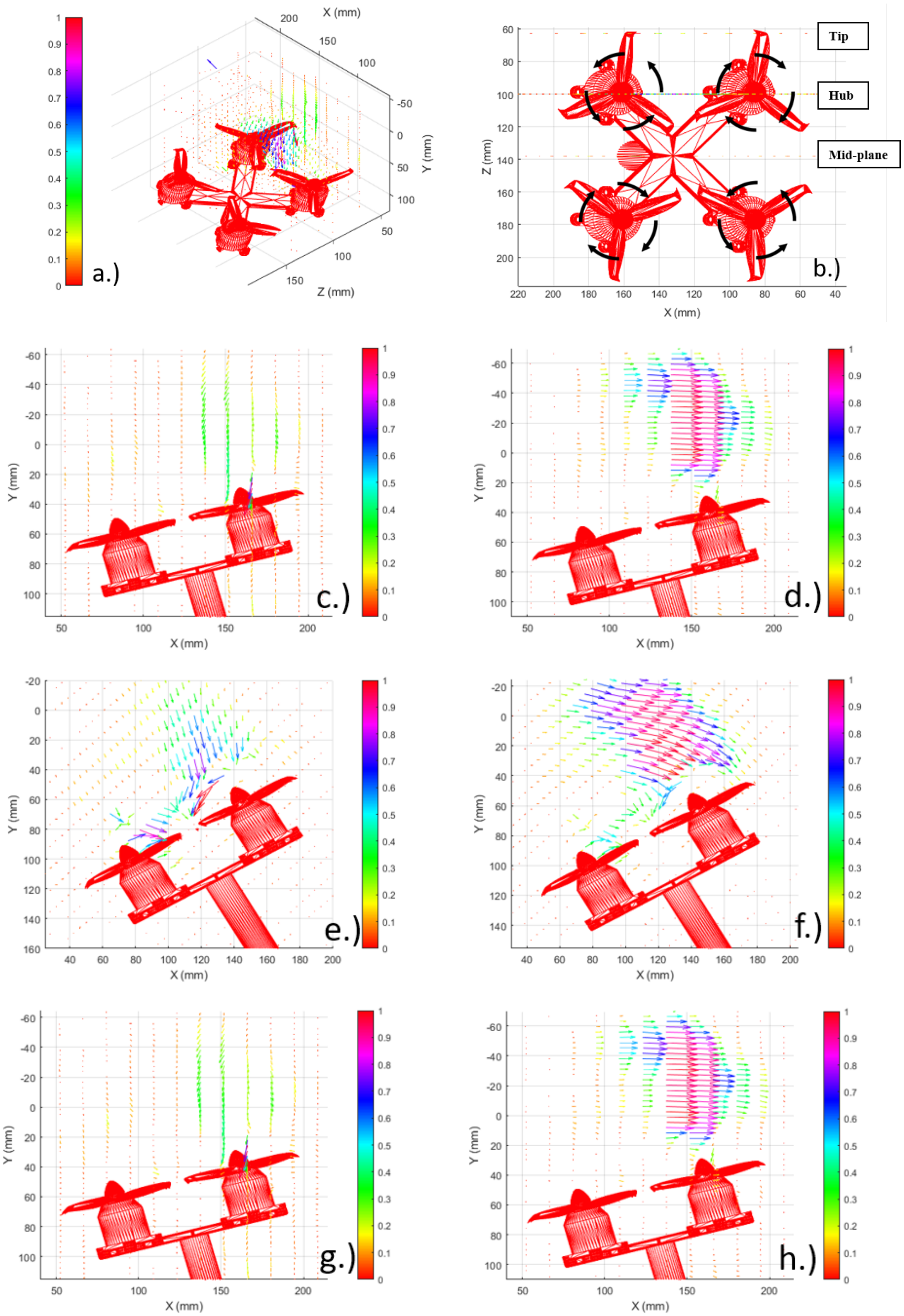

Figure 78: Inflow Velocity Field: Quad Rotor X 15°: a.) 3D-View b.) Top-View c.) 0m/s Midplane d.) 0.5m/s Midplane, e.) 0m/s Hub f.) 0.5m/s Hub g.) 0m/s Tip h.) 0.5m/s Tip

The Quad rotor X-configuration in 30 degrees for both the mid-plane and tip showed small inflow velocities. The hub test case again show the highest inflow velocities however the 30 degree test case the flow-field is shifted sightly downstream past the rotors. Additionally, the mid-plane 0.5m/s and the tip 0.5m/s data do not show the average velocity of the cross-stream. This indicts that the data for those tests is poor quality and should be redone.

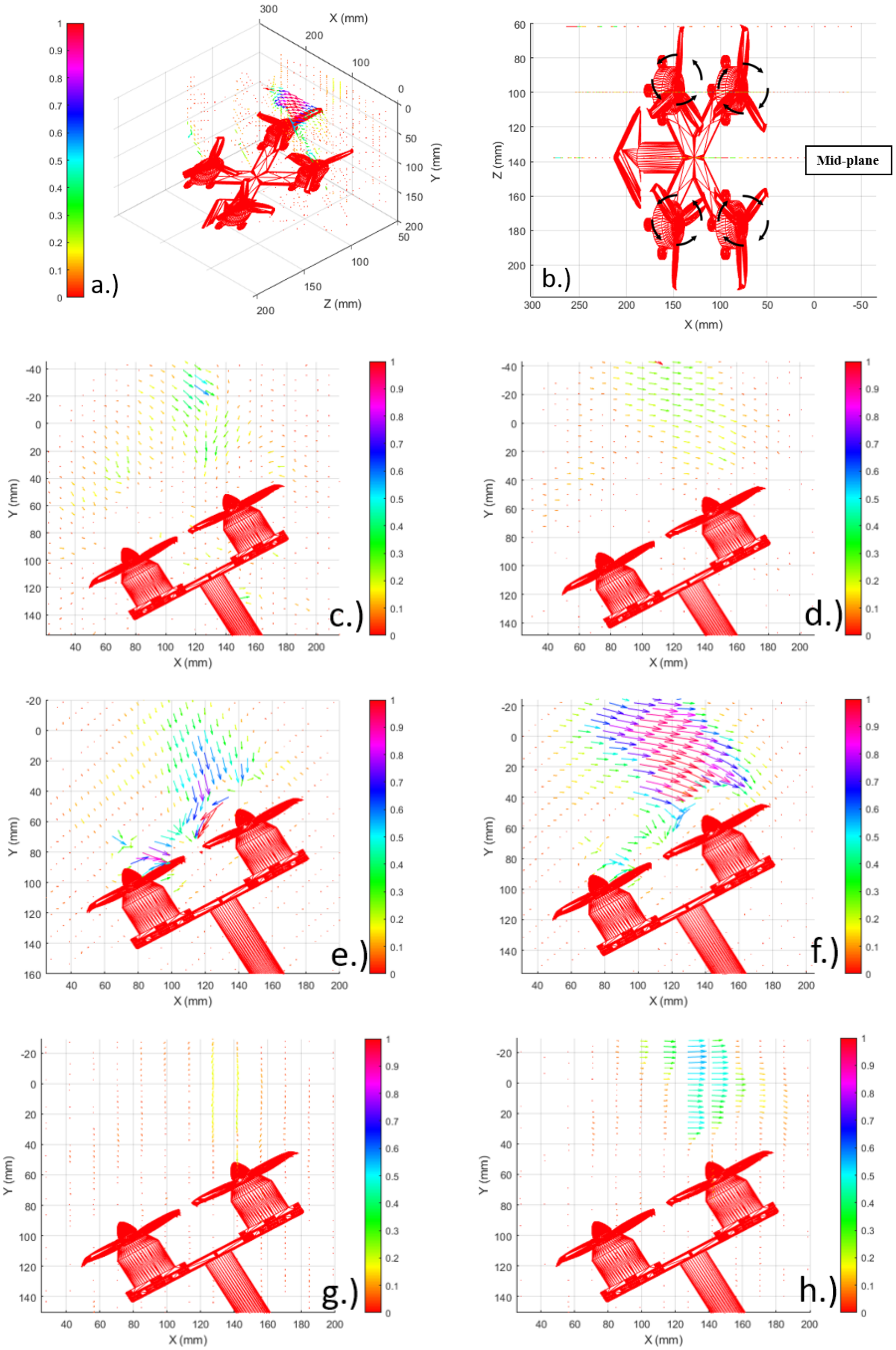

Figure 79: Inflow Velocity Field: Quad Rotor X 30°: a.) 3D-View b.) Top-View c.) 0m/s Midplane d.) 0.5m/s Midplane, e.) 0m/s Hub f.) 0.5m/s Hub g.) 0m/s Tip h.) 0.5m/s Tip

For the Quad plus in the hover, the mid-plane passes over the leading and trailing motor.

It shows the greatest velocity moving over the leading motor. For the hub case there is a significant void in the center. The tip shows the least amount of flow effect.

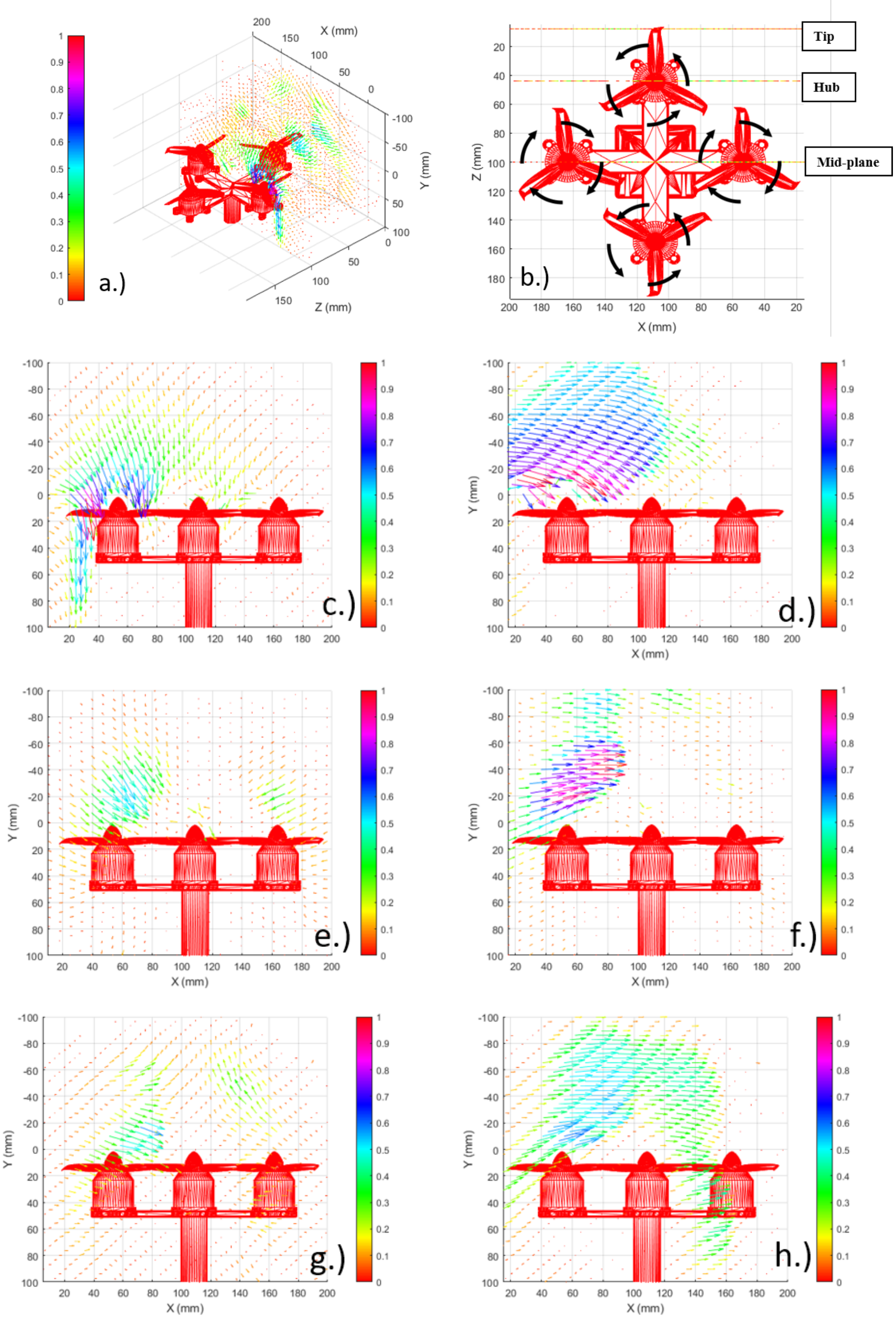

Figure 80: Inflow Velocity Field: Quad Rotor Plus 0°: a.) 3D-View b.) Top-View c.) 0m/s Midplane d.) 0.5m/s Midplane, e.) 0m/s Hub f.) 0.5m/s Hub g.) 0m/s Tip h.) 0.5m/s Tip

For 15 degree test the hub voids are shifted downstream slightly for 0.5m/s tests.

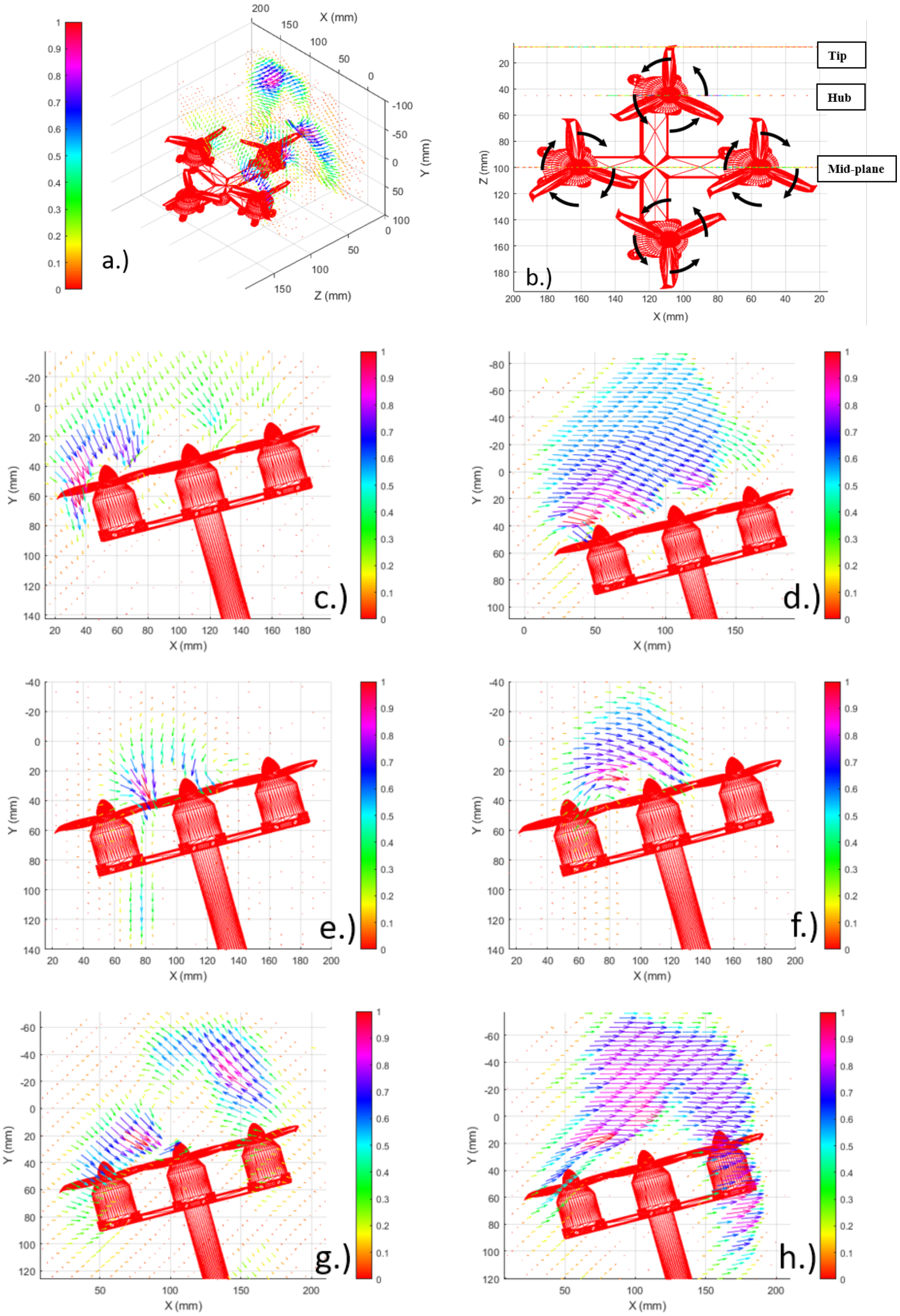

Figure 81: Inflow Velocity Field: Quad Rotor Plus 15°: a.) 3D-View b.) Top-View c.) 0m/s Midplane d.) 0.5m/s Midplane, e.) 0m/s Hub f.) 0.5m/s Hub g.) 0m/s Tip h.) 0.5m/s Tip

For the 30 degree test the hub voids are again shifted downstream slightly for the 0.5m/s tests and the dead-spots are enlarged.

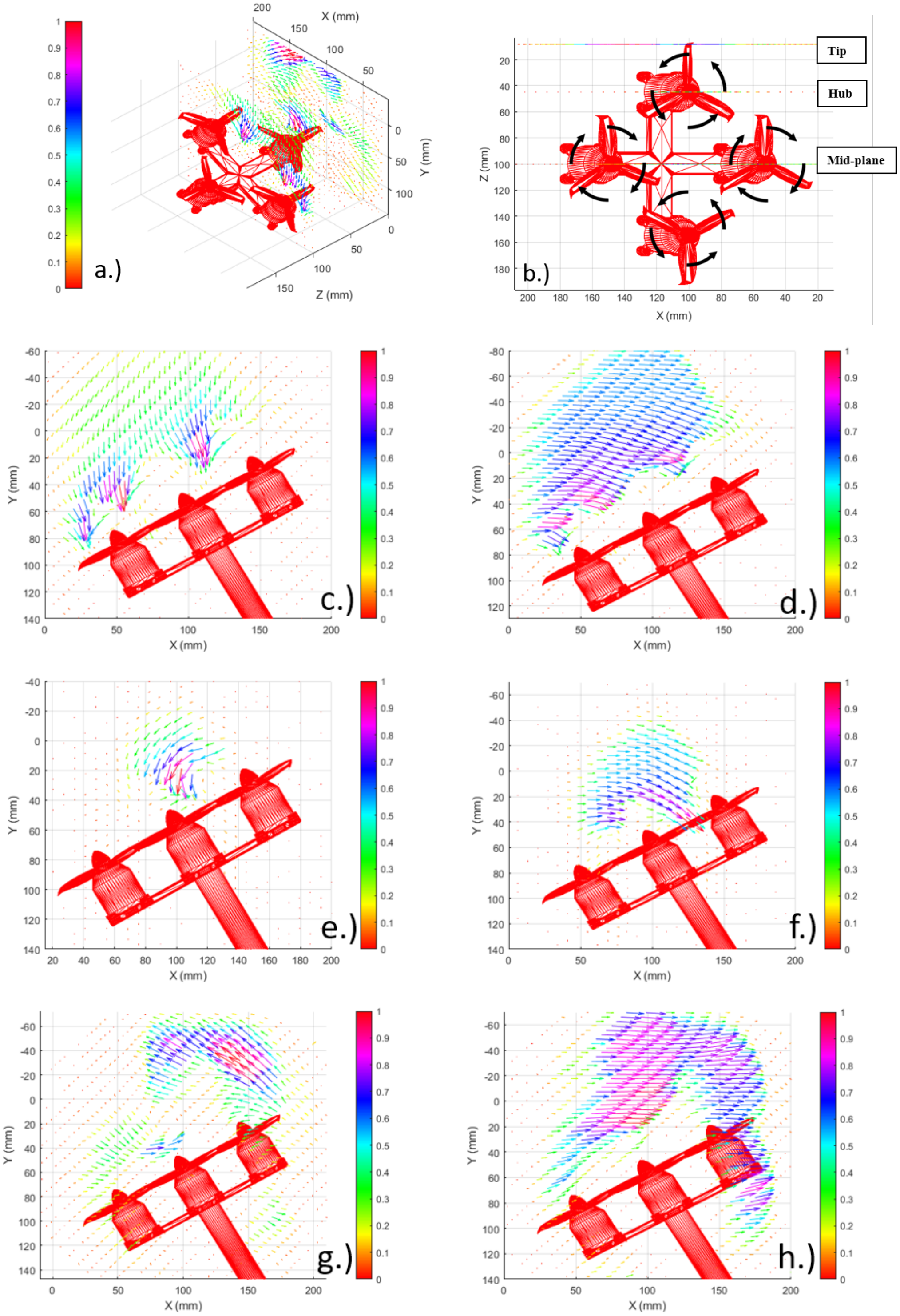

Figure 82: Inflow Velocity Field: Quad Rotor Plus 30°: a.) 3D-View b.) Top-View c.) 0m/s Midplane d.) 0.5m/s Midplane, e.) 0m/s Hub f.) 0.5m/s Hub g.) 0m/s Tip h.) 0.5m/s Tip

Next, the U and V velocities were separated out and plotted against each other so the velocity profiles could be observed. For these results only the velocities in the vertical direction will be examined. The graphs show the velocity for each test case plotted along the x distance of the test section.

4.1.2 Vertical Velocity Profiles

Starting with the dual parallel tests again. The midblade and hub have the greatest vertical velocities. With hub having a dead region in the center of the hub and the midplane usually have a solid spike of vertical velocity this spike is shifted to the left on the 30 degree tests. On 15 degree 0m/s the velocity drop-off for the leading, trailing rotor hub and center of the multi-rotor is observed. Additionally the horizontal position of the vertical velocity peaks stayed the same during cross-stream tests as they were during the ambient tests.

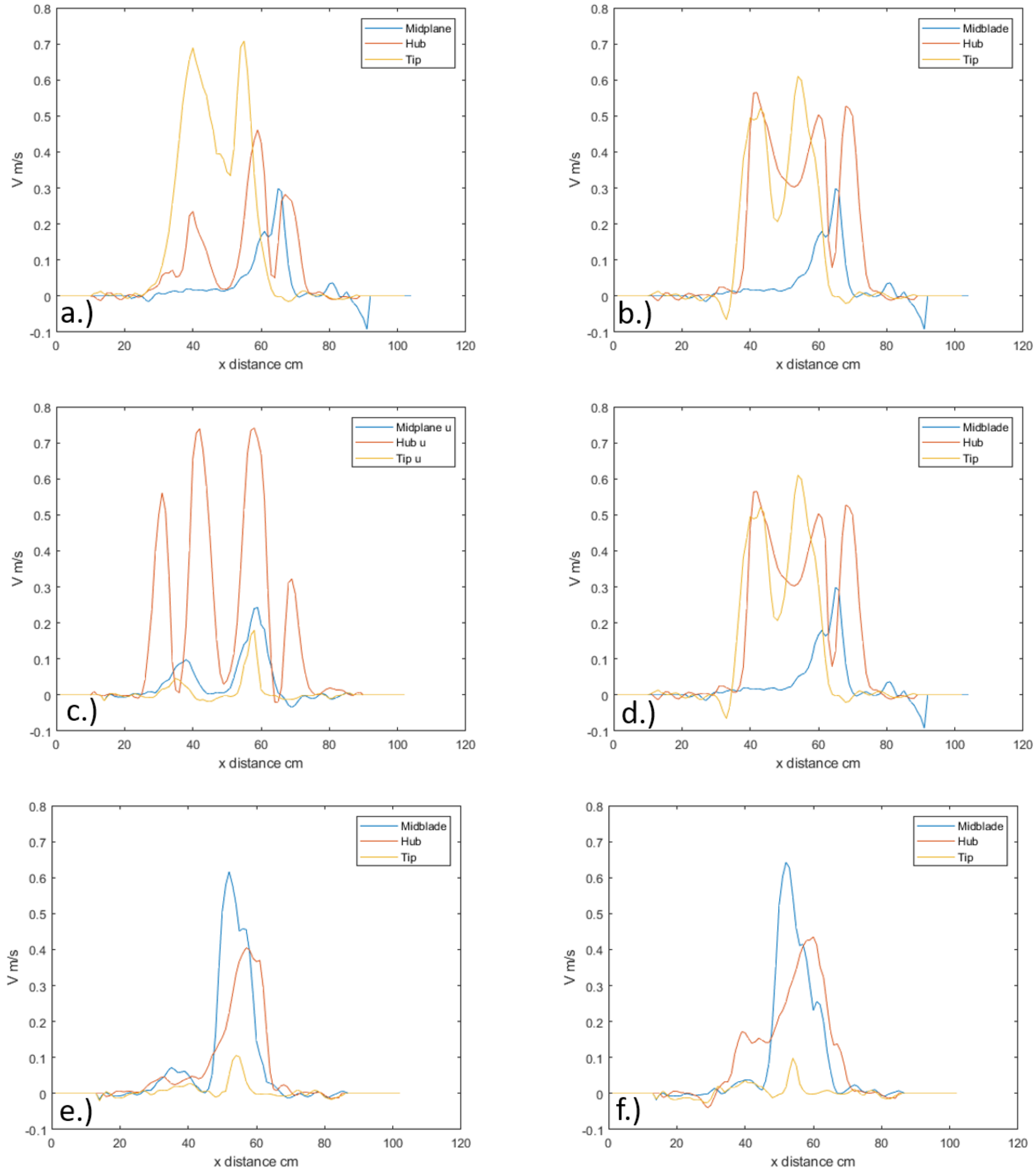

Figure 83: Vertical Profile Dual Parallel: a.) (0m/s, 0°), b.) (0.5m/s, 0°), c.) (0m/s, 15°), d.) (0.5m/s, 15°), e.) (0m/s, 30°), f.) (0.5m/s, 30°)

For the perpendicular tests the tip velocities again show as single spike of increase in velocity. As the midplane is positioned between the rotors for these test. There is an observed dead-spot in the center of the rotors for the ambient tests. This dead region was not observed in the 0.5m/s tests. The hub tests again show single drop-off in velocity directly over the rotor hub as there is only one rotor hub for these tests.

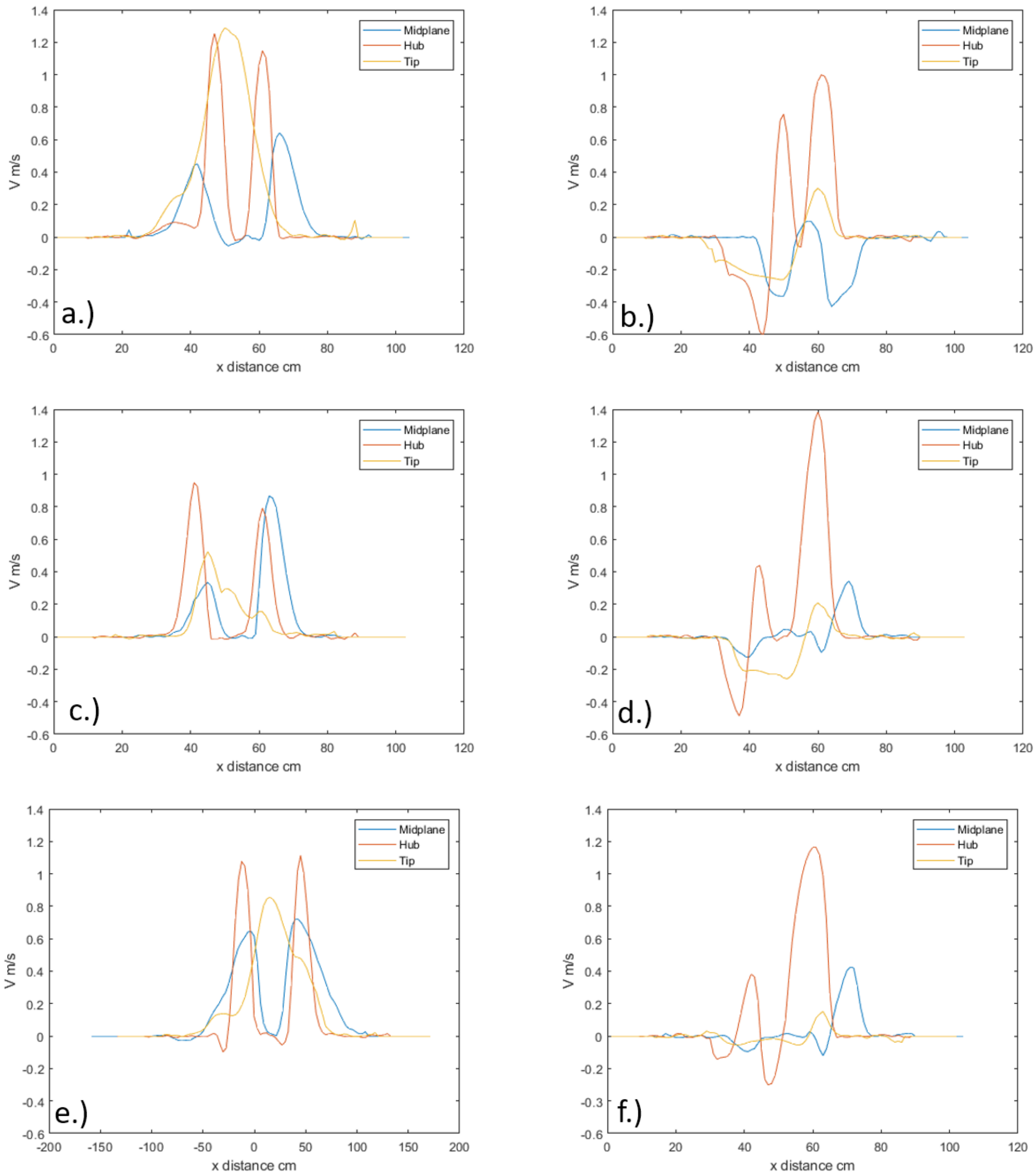

Figure 84: Vertical Profile Dual Perpendicular: a.) (0m/s, 0°), b.) (0.5m/s, 0°), c.) (0m/s, 15°), d.) (0.5m/s, 15°), e.) (0m/s, 30°), f.) (0.5m/s, 30°)

Next Quad X tests, the midplane or center of the multi-rotor shows the smallest velocities for the Quad X tests. The overall maximum velocities stayed relatively the same as the dual rotor test despite the two extra rotors involved. The hub had the greatest velocities for these tests but the dead-region was not observed in any of these tests.

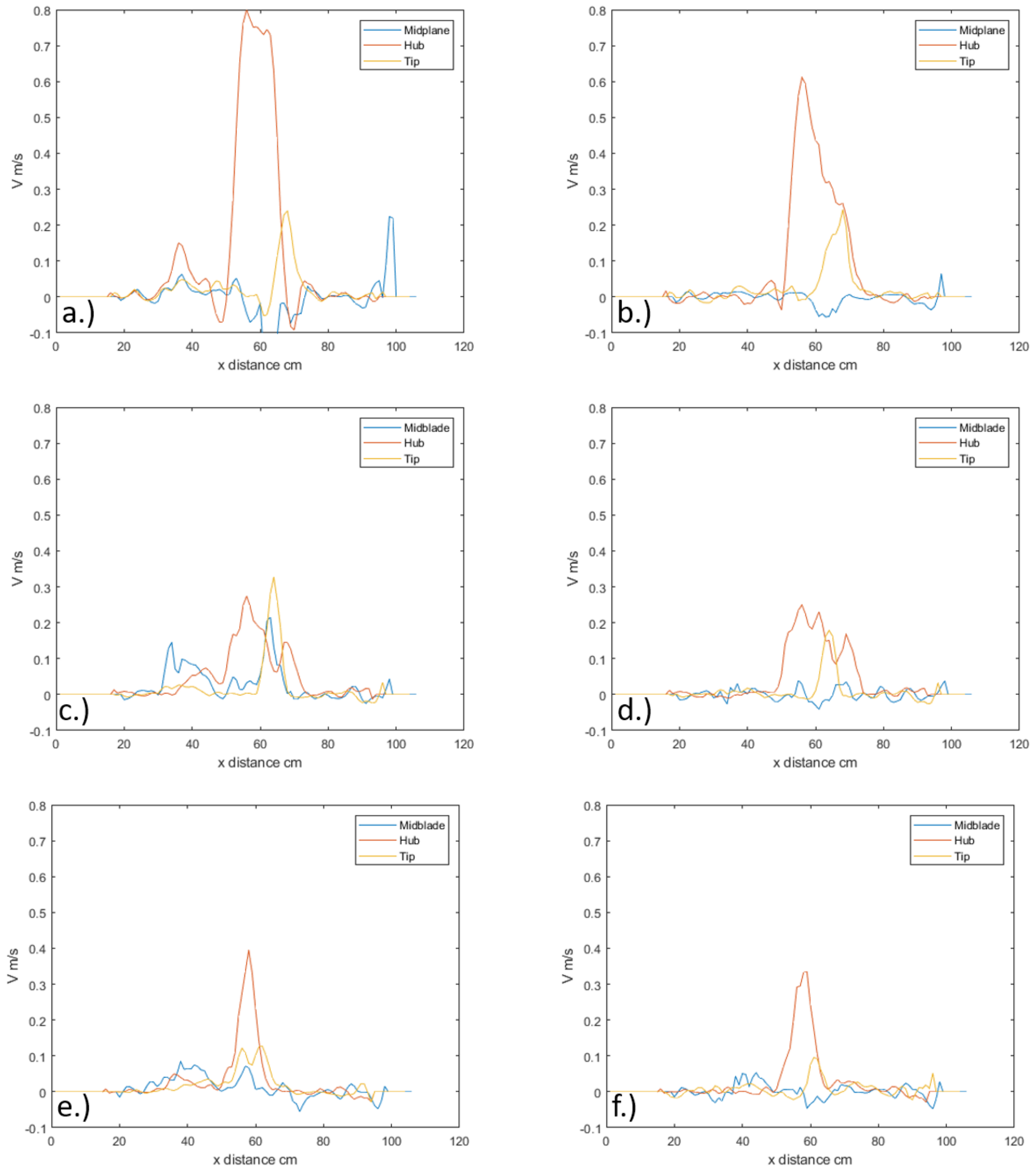

Figure 85: Vertical Profile Quad X: a.) (0m/s, 0°), b.) (0.5m/s, 0°), c.) (0m/s, 15°), d.) (0.5m/s, 15°), e.) (0m/s, 30°), f.) (0.5m/s, 30°)

The quad plus tests show the mid-plane with the highest velocities where the leading and trailing rotor hubs are. The dead-region in mid-plane tests for the two rotor hubs tests is observed in the first three tests but not the last three. The tip tests showed the least velocity overall.

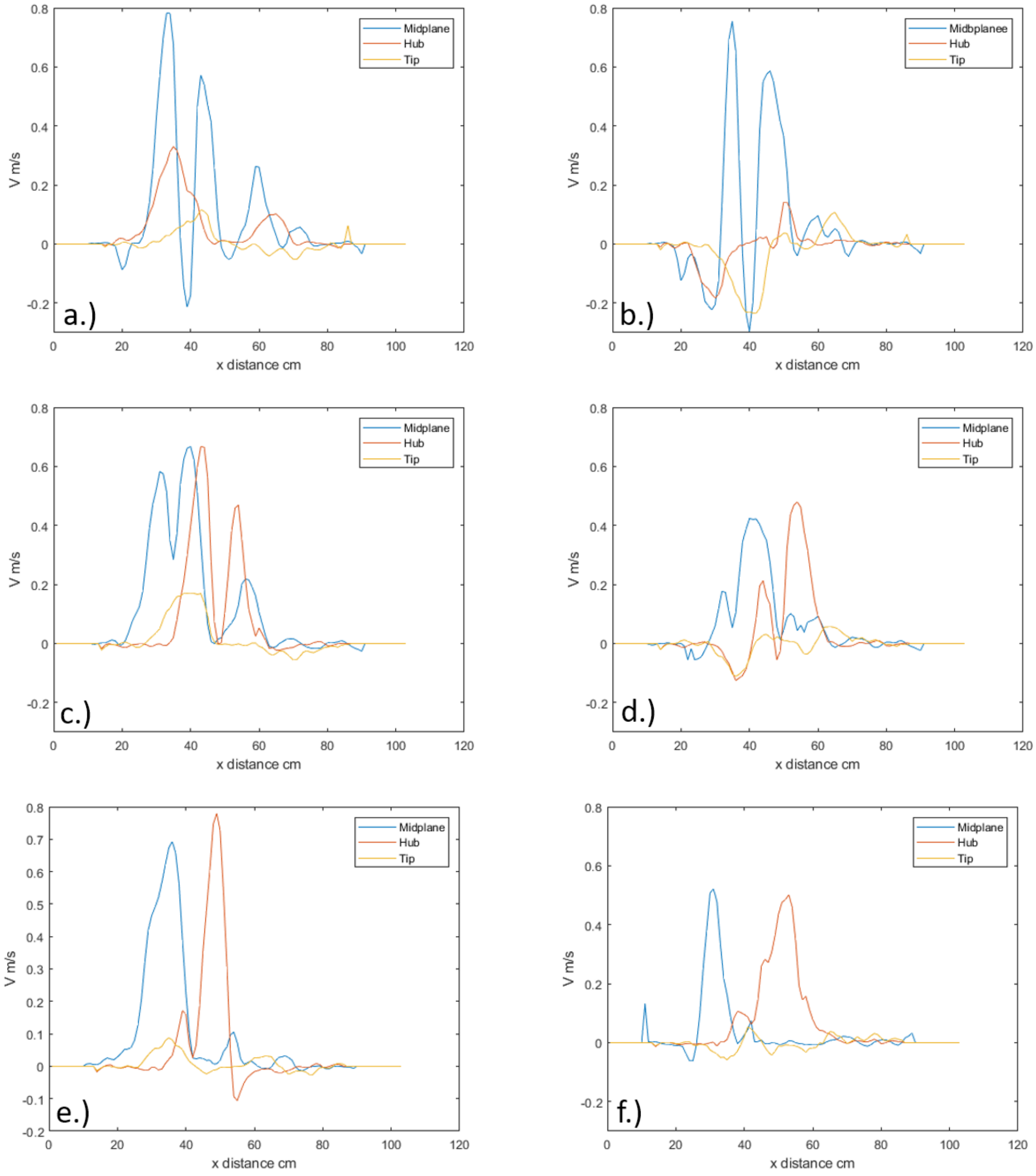

Figure 86: Vertical Profile Quad +: a.) (0m/s, 0°), b.) (0.5m/s, 0°), c.) (0m/s, 15°), d.) (0.5m/s, 15°), e.) (0m/s, 30°), f.) (0.5m/s, 30°)

4.2 Single Rotor Experiment

Moving onto the single rotor experiment in an ambient chamber. The results are shown below. The graphs below shows averaged velocities recorded by the FT anemometer. All of the graphs show that the highest recorded velocities happen directly above the rotor hub.

The graph recorded the highest velocity at 20cm height, the closest distance the sensor was tested at. This confirms what was observed in the PIV, the inflow will be stronger towards the center of the rotor. After though, moving the sensor just 8 cm more to the 28cm height there is sharp drop off in velocity recorded. After that the velocity seems to decrease at a much smaller and linear rate before stopping at out 0.2 m/s which is just above the maximum resolution of the FT (0.1 m/s). This study also confirms the hypothesis that the inflow velocities decreases when the sensor placement height increases.

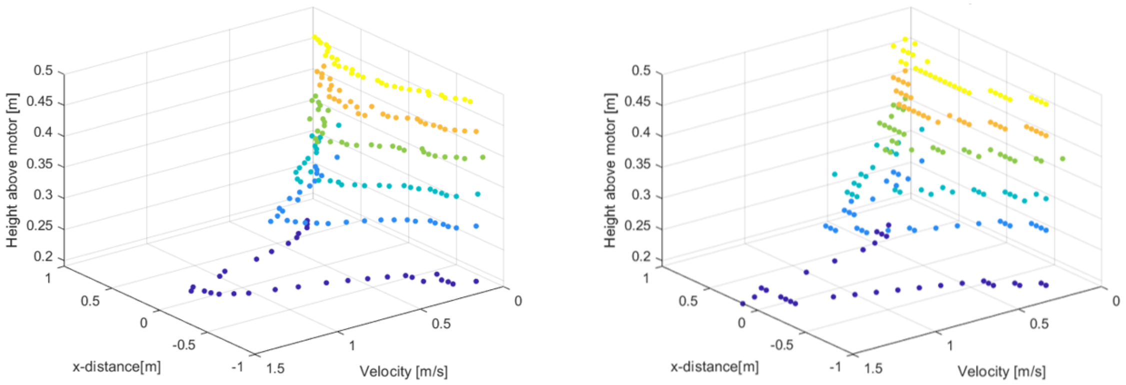

Figure 87: Left.) Average Velocities at Locations, Right.) Maximum Velocities at Locations

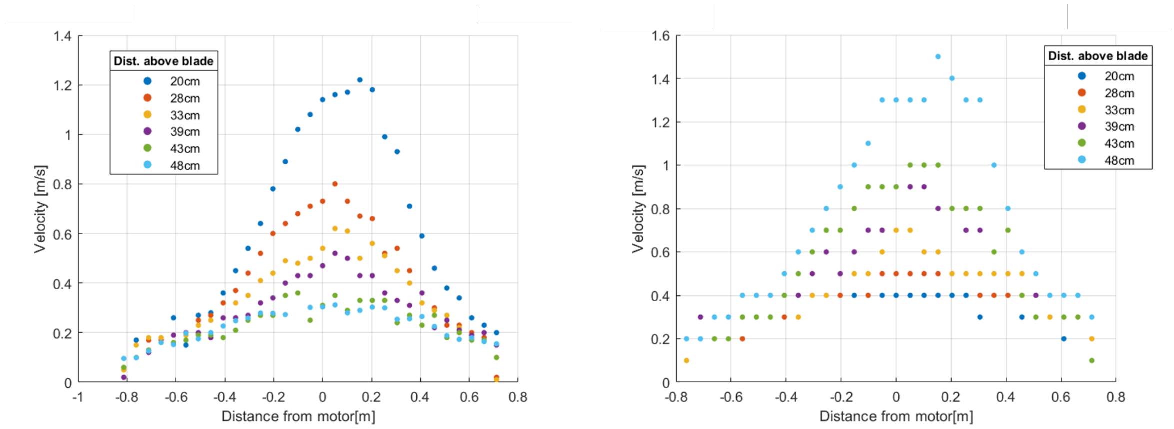

Figure 88: Left.) Average Velocities in wake, Right.) Maximum Velocities in Wake

4.3 Tower Comparison Experiment

Finally, the tower comparison experimental results. The velocities from each sensor are shown for each position tested, starting with the front position tests. The Trisonica sensor showed higher velocities then the tower sensor for all tests.

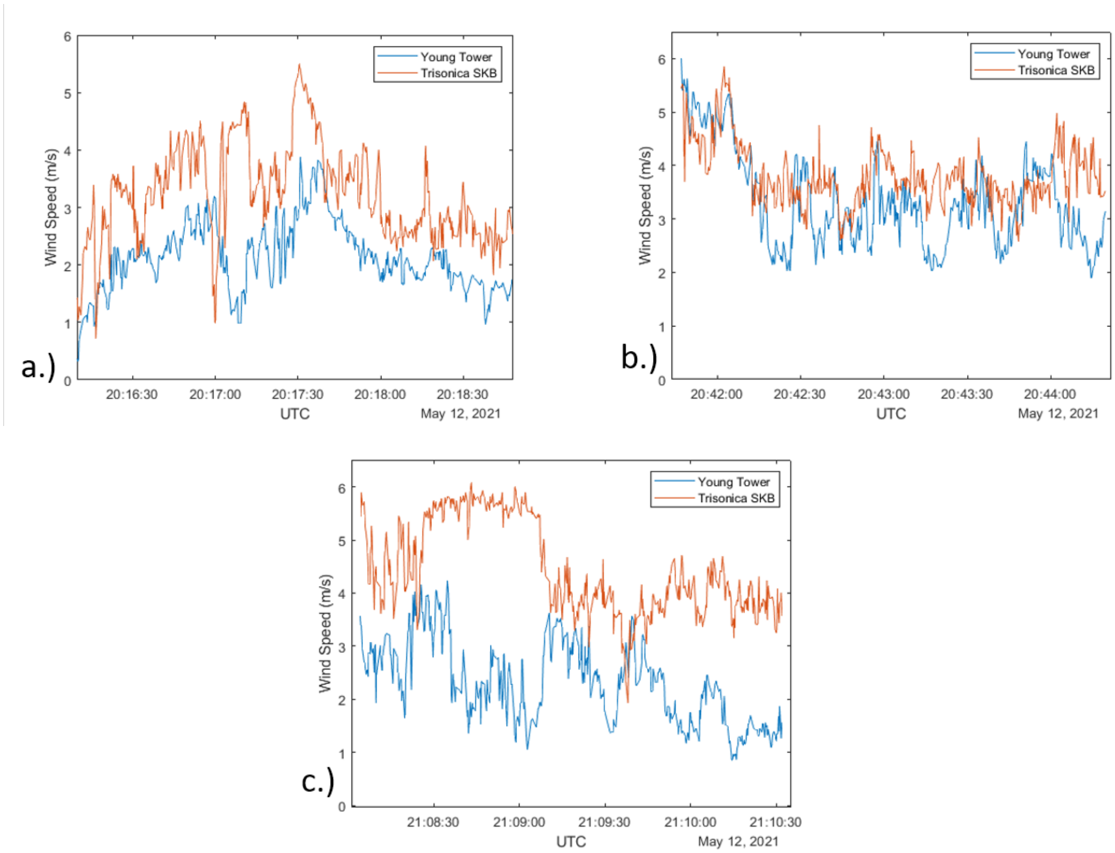

Figure 89: Front Position: a.) 24in b.) 20in c.) 16in

Next, the front position showed very similar results to the back position tests.

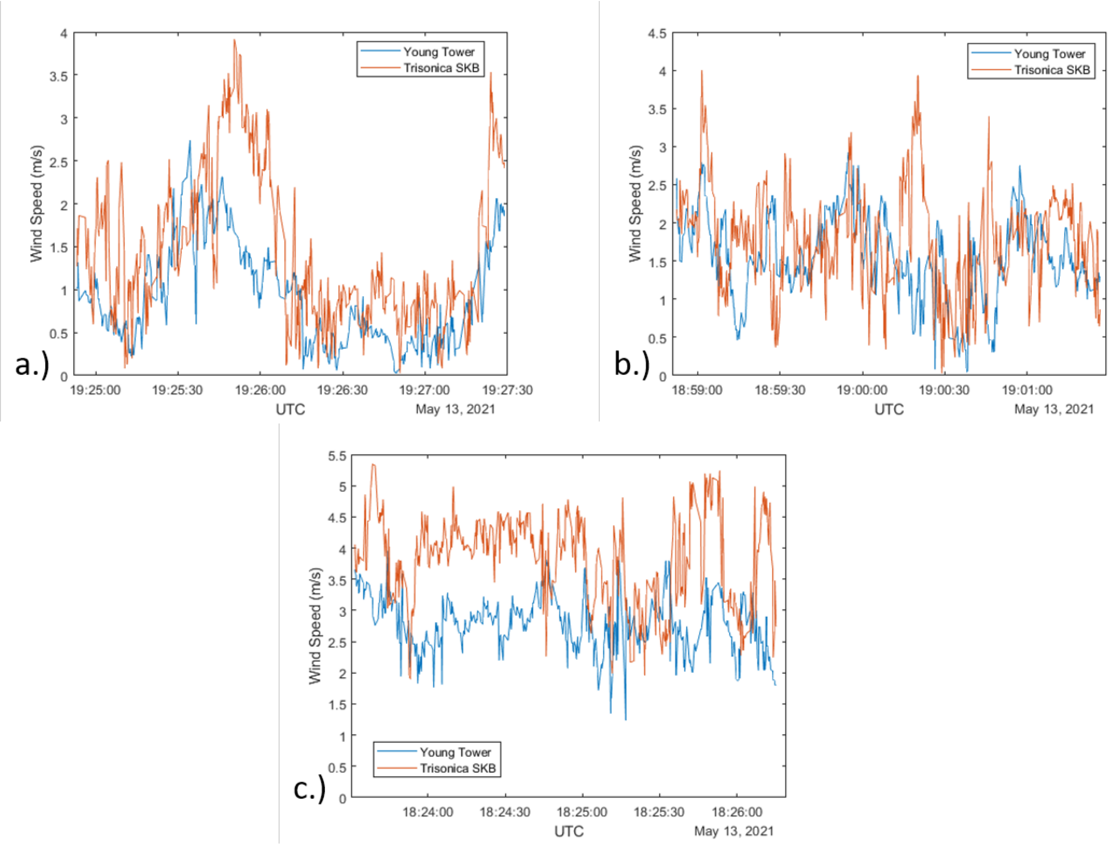

Figure 90: Back Position: a.) 24in b.) 20in c.) 16in

Finally, the middle position tests which on average showed the least amount of difference between the two sensors.

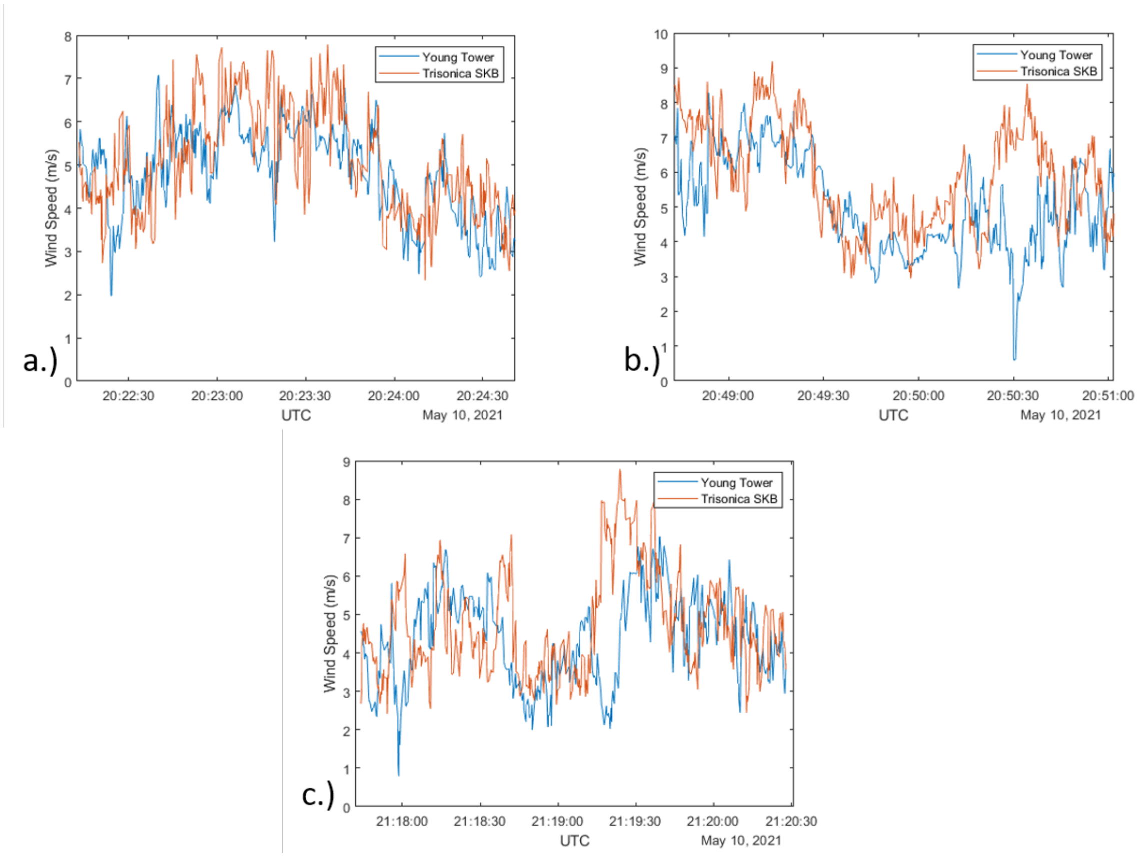

Figure 91: Middle Position: a.) 24in b.) 20in c.) 16in

The table below shows the average velocities for each sensor for each test and the average difference between the two. The tests were completed on three different days so wind speeds varied for each set of tests. The average velocities range from 1m/s to 5m/s.

Table 6: Multi-rotor Vs. Tower Comparison: Average Velocity

Position	Avg. Vel. Young (m/s)	Avg. Vel. Trisonica (m/s)	Avg. Difference
Back 24in	0.93	1.47	0.54
Front 24in	2.14	3.21	1.07
Middle 24in	4.80	5.05	0.25
Back 20in	1.54	1.78	0.24
Front 20in	3.32	3.806	0.49
Middle 20in	5.06	5.94	0.88
Back 16in	2.80	3.80	1.0
Front 16in	2.32	4.45	2.14
Middle 16in	4.31	4.66	0.35

The table below show the statistics analyzes over the test cases. The 24in mount height had the strongest correlation coefficient in all positions with the correlation coefficient decreasing as the mount height decreases. For several tests, the root mean squared error was less then or close 1 m/s. The error between the two sensors also increases with increase in wind speed. As the back 24in had a RMSE of 0.84m/s while the middle 24in test had RMSE of 1.08m/s but was tested on the day with higher wind speeds. This indicts that the higher wind speed slightly increases the error between the sensors.

Table 7: Multi-rotor Vs. Tower Comparison: RMSE, Bias, Correlation Coeff.

Position	RMSE (m/s)	Bias (m/s)	Correlation Coeff.
Back 24in	0.84	0.54	0.70
Front 24in	1.30	1.069	0.54
Middle 24in	1.08	0.267	0.60
Back 20in	0.89	0.231	0.60
Front 20in	0.90	0.489	0.52
Middle 20in	1.74	0.89	0.45
Back 16in	1.32	1.02	0.03
Front 16in	2.37	2.13	0.22
Middle 16in	1.65	0.354	0.16

Below the two tables shows the standard deviation and variance of both of the sensors for each test. The standard deviation for each sensor were similar to each for each most of the tests but with Young sensor consisly having a smaller standard deviation then the Trisonica. The on exception being the front 20in test.

Table 8: Multi-rotor Vs. Tower Comparison: Variance

Position	Variance Young	Variance Trisonica
Back 24in	0.35	0.82
Front 24in	0.36	0.74
Middle 24in	1.17	1.47
Back 20in	0.31	0.50
Front 20in	0.75	0.33
Middle 20in	1.87	2.17
Back 16in	0.22	0.52
Front 16in	0.61	0.74
Middle 16in	1.38	1.7

Table 9: Multi-rotor Vs. Tower Comparison: Standard Deviation

Position	STDV Young	STDV Trisonica
Back 24in	0.59	0.91
Front 24in	0.60	0.86
Middle 24in	1.08	1.21
Back 20in	0.56	0.71
Front 20in	0.87	0.58
Middle 20in	1.37	1.47
Back 16in	0.47	0.72
Front 16in	0.78	0.86
Middle 16in	1.17	1.30

Below the two tables show the skewness and kurtosis of both sensors for each test completed. Most of the tests have a skewness value in between the -0.5 and 0.5 meaning the data is fairly symmetrical. The few exceptions were the back 24in and 20in test and the trisonica middle 16in test, all which a had positive skewness of less then 1. All of the test have a kurtosis value of less then 3 indicting a normal distribution.

Table 10: Multi-rotor Vs. Tower Comparison: Skewness

Position	Skewness Young	Skewness Trisonica
Back 24in	0.58	0.64
Front 24in	0.13	0.09
Middle 24in	-0.36	0.23
Back 20in	-0.17	0.26
Front 20in	0.77	0.85
Middle 20in	0.038	0.05
Back 16in	-0.10	-0.38
Front 16in	0.25	0.29
Middle 16in	-0.12	0.78

Table 11: Multi-rotor Vs. Tower Comparison: Kurtosis

Position	Kurtosis Young	Kurtosis Trisonica
Back 24in	-0.65	-.64
Front 24in	0.55	0.22
Middle 24in	-0.73	-0.89
Back 20in	-0.13	0.21
Front 20in	0.015	1.03
Middle 20in	-0.51	-1.09
Back 16in	-0.09	-0.54
Front 16in	-0.86	-1.1
Middle 16in	-0.64	0.07

June 3 2021 Airfield Hover Test

To test the hypnosis that higher wind can effect the error of the sensor. The SKB-1000 was taken out to the Oklahoma State University airfield and fitted with the middle 24in position. That day the average wind speed of around 2(m/s), around 3 (m/s) slower then average of when the original middle 24 position was tested. The same hover test was conducted and the data was compared to the tower mounted sensors. The table and figure below go over the results of that day.

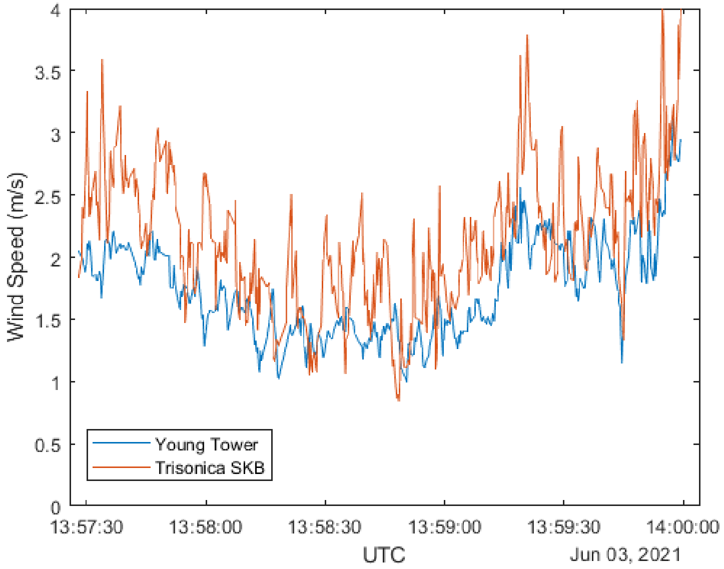

Figure 92: Middle 24in

Table 12: Middle 24in Calm Day

Statistics	Result
Avg. Vel. Young (m/s)	1.75
Avg. Vel. Trisonica (m/s)	2.14
Avg. Difference	0.39
RMSE (m/s)	0.57
Bias (m/s)	0.402
Correlation Coeff.	0.71
Variance Young	0.15
Variance Trisonica	0.33
Skewness Young	0.56
Skewness Trisonica	0.34
Kurtosis Young	0.01
Kurtosis Trisonica	0.18

The results show lower root mean squared error of 0.57 (m/s) and a higher correlation coefficient then the previous test. It is hard to draw conclusions with two data points but with this it can be assumed the higher winds can slightly increase the error rates of multi-rotor mounted sensors.

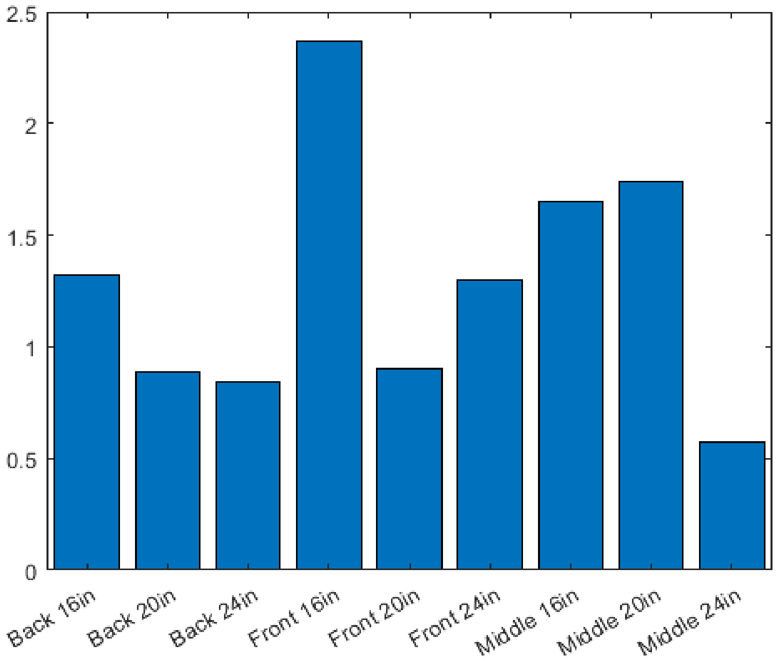

Figure 93: RMSE (m/s) Graph

More tests at various wind speeds should be conducted to confirm this hypothesis. Overall the middle 24in position performs the best reliably over the largest range of wind speeds as seen from the graph above.

Several wind gusts occurred during testing and were picked up by both sensors and analyzed. Shown below is a wind gust that occurred during the back 24in test. The gust lasted for about 30 seconds with a maximum velocity of 4 m/s. From the graph it can be observed that the young sensor lags behind the trisonica. This could be because both sensors were pointed into the wind, with the trisonica being about 30 feet in front of the young sensor.

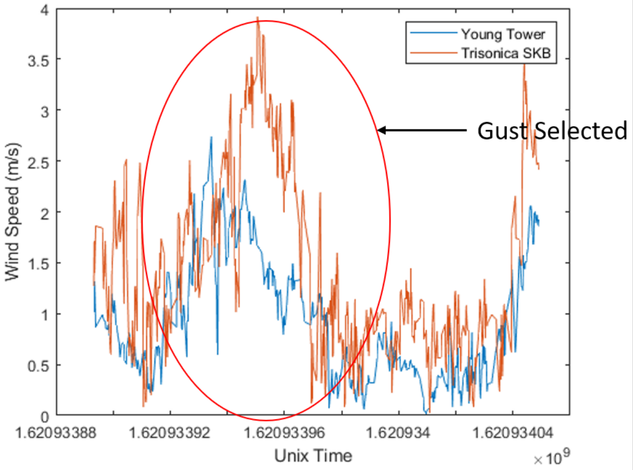

Figure 94: Gust Selected

The gust was parsed from the data selected and analyzed in matlab using the cross correlation function.

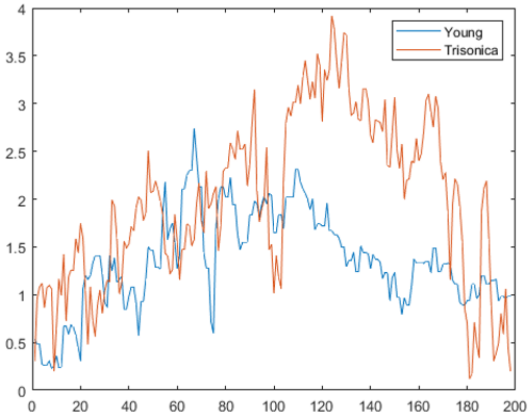

Figure 95: Gust Selected

Below is the the cross correlation of the two sensors. From the graph it be observed that the peak is shifted slightly to the left and the largest spike occurs at the lag value match exactly (-3).

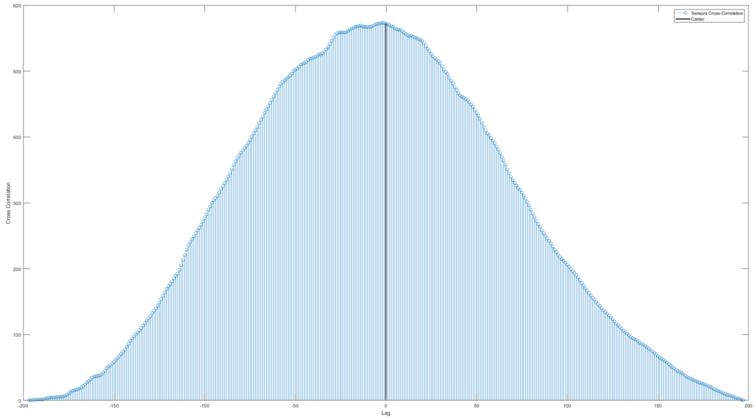

Figure 96: Cross Correlation

One method for checking the quality of a system's velocity measurements is to check if the results follow the Kolmogorov's -5/3 power law. The law is based around atmospheric turbulence having a frequency decay of -5/3.

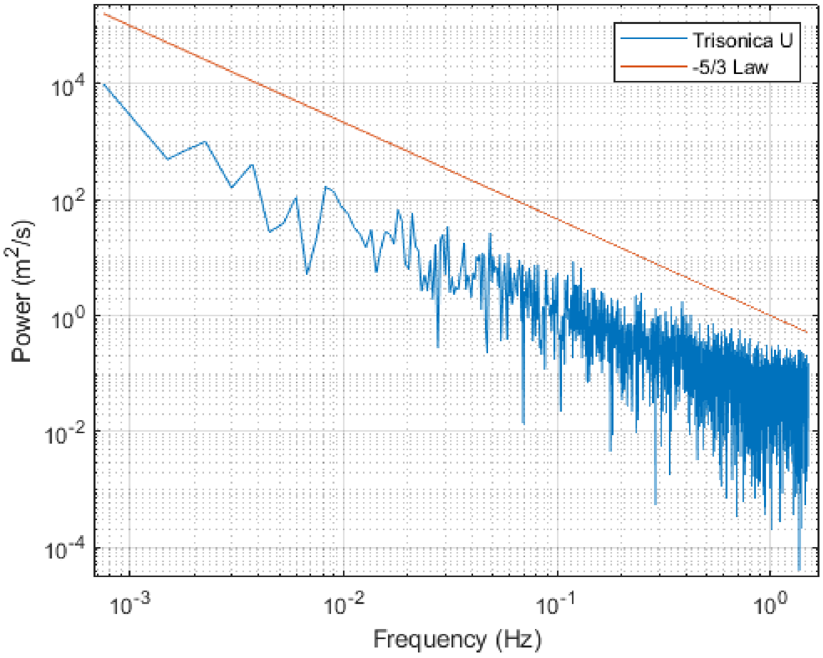

Figure 97: Spectral Power Density with -5/3 Law

The graph above show the power spectral density of the middle 24in test as this position performed the best. The blue is the power spectral density of the trisonica data acquired on top of the SKB-1000. The frequency decay of the data show that the results follow the -5/3 law.

4.4 Demonstration Flight Campaigns

To test capabilities of the SKB-1000 system flight campaigns were conducted at Oklahoma State University along with two other UASs. The flight took place on May third 2021 at the Oklahoma State University Unmanned Aircraft Flight Station, East of Stillwater Oklahoma. The SKB-1000 was outfitted iMET-XQ2 and the Trisoinca allowing it to capture the temperature, pressure humidity and wind speed and direction. The SKB-1000 was also flown in tandem with two other UAS system, the nano-talon a small fixed-wing UAV and the nimbus a VTOL fixed-wing UAV. Both systems were equipped with 3d-printed 5-Hole probes and temperature, pressure and humidity sensor suite. The goal of the flight demonstration was to acquire weather data and compare the data gathered from each system.

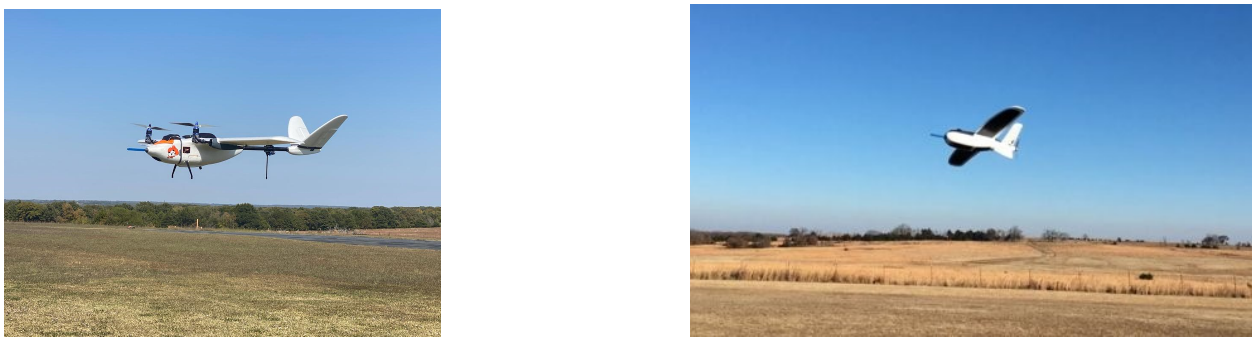
(a) VTOL Nimbus

(b) Nano Talon

Figure 98: Fixed-Wing UAVs

On the day of the flight demonstration a front moved through the Payne county area. The SKB-1000 was flown in QLoiter mode that hold altitude and position. While the nimbus and nano-talon were flown in autonomous mode. Each system had a dedicated flight pattern that each flown close proximity to each other. The SKB-1000 flew a vertical profile starting from takeoff climbing altitude in sync with the other fixed-wing systems. The nano-talon flew circular orbits around the SKB-1000 and nimbus flew box pattern around the two. The UASs started together at 500ft and climbed in 500ft increments for five test points (500, 1000, 1500, 2000, 3000)ft. Once each system had reached the test point altitude the hold altitude and perform their respective flight patterns for several minutes. Below is a sounding created from each system recorded during their flights.

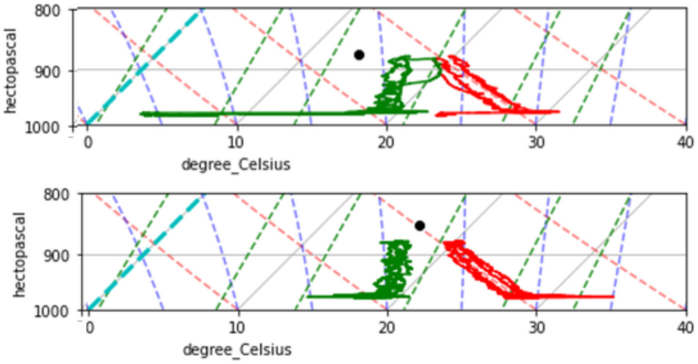

Figure 99: UAV Sounding: Top - SKB, Bottom - Nimbus

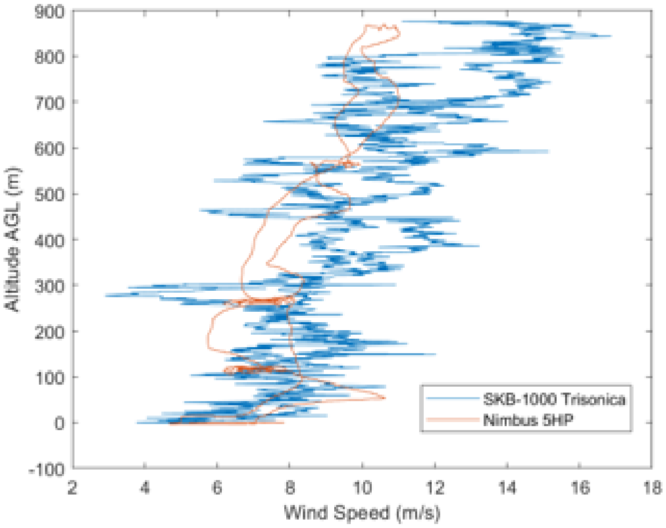

Figure 100: SKB-1000 and Nimbus Windspeed Vs. Alt.

The windspeed recorded from the SKB-1000 are shown in the figure above and will be compared to the windspeeds captured to the other systems.While during the hover phases of the flight mission the SKB-1000 recorded accurate wind data as this what the system was calibrated for, but there was a dramatic increase of wind-speed recorded on the Trisonica during the ascent phases of the quad-copter. This increase of wind speed could be due two things either the increase of rotor RPM during the ascension or the vertical movement of the SKB-1000 through the air. To determine which hypothesis was correct an ground experiment was performed. On the ground the SKB-1000 was secured to platform located 8 ft above the ground to keep it out of any rotor wash. Then the SKB-1000 and the trisonica was turned and the SKB-1000 throttle up 100 perecent several times. Below the graph shows the throttle output and windspeed recorded during the test.

Figure 101: Quad-copter Thrust Stand

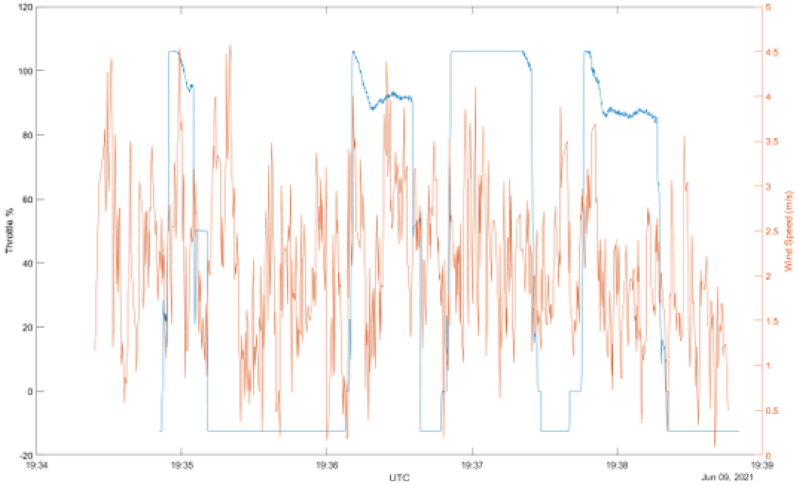

Figure 102: Quad-copter Throttle Output and Windspeed

A t-test analysis was performed to determine if there a statistical difference between throttle on and off. The the results from test are shown in the tables below.

Table 13: Multi-rotor Max RPM Average an Variance

Result	Throttle on	Throttle off
Mean (m/s)	1.85	1.63
Variance (m/s)	0.36	0.74

Table 14: Multi-rotor Max RPM T-Test Results

Result	Result
df	236
t Stat	-2.48
P(T¡=t) two-tail	0.01
t Critical two-tail	1.97

From the graph and t-test shown above there is no indication of huge increase in wind speed from the trisonica. There for it is proposed to that increase of wind speed comes from the vertical movement of the quad-copter. This increase of wind speed during vertical ascension should be calibrated out in the future but for now the SKB-1000 has an operational limitation of gathering wind data only during a hover position.

CHAPTER V

CONCLUSION

Starting with the PIV experiment, several main trends were observed from the testing. The inflow velocity increases consistently closer to center of the rotor hub and decreases as it the moves further away from the rotor hubs. In addition, the flow shifts in correlation with the angle of the rotors. The vertical velocity of the inflow also stays in relatively the same position in cross-stream. Additionally, the quad-rotor system showed roughly the same velocity magnitude as the dual rotor system, although the size of the inflow region increased from the added two rotors, the magnitudes of velocity stay the same throughout the all of the tests. There are also several dead-regions that can be observed from the tests. Most of these regions are located either above the rotor hubs or are in-between the rotors of the multi-rotor system. The tips positions consistently showed the lowest velocities then the hubs.

Moving onto the single rotor experiment in the ambient chamber again, the same trends from the PIV experiment is observed as the inflow velocity increases the closer to center of the rotor hub. From this experiment the hypothesis of moving the sensor farther away from the rotor plane will show a decrease in inflow velocity. The highest velocity recorded was 1.2m/s at closest distance tested of 20cm. Moving the sensor 8cm away from the sensor show a steep decrease in velocity of around 0.4 m/s. Following the first 8cm increment velocity deceases at a smaller linear rate of 0.2 m/s. Finally the limit of the resolution of the sensor was approached at around 48cm, roughly 1.15 x of the diameter of the propeller used.

Finally, the tower comparison tests show that placing the sensor in the center of the multi-rotor at least 24in will provide the best results. The tests consistently showed that multi-rotor mounted anemometer displaying higher velocities the tower mounted anemometer. The front and back position showed similar results for all mounted heights, showing that than flow is relatively symmetrically around the rotors. The tests showed the multi-rotor mounted sensor is capable of a root mean squared error of less than 0.8m/s in wind speeds of up to 5m/s. The tests also showed wind gusts up to 8m/s during the testing. During gusts, the difference in error of the sensors increased compared to when the wind was steady. The results showed that as the wind averaged speed increased the error on the multi-rotor mounted sensor increased also. Overall the 24in mount height had the highest correlation between the two anemometer sensors for all positions. Roughly 1.1x of the diameter of the propeller used. Overall the middle 24in position performed the best with the highest correlation coefficient 0.70 and root mean squared error of 0.54m/s. The second best, position was the back 24in position, with a correlation coefficient of 0.70 and root mean squared error of 0.84 m/s. The third best performing position was the middle 20in. with correlation coefficient of 0.45 and root mean squared error of 0.90 m/s. The performance of the middle 24in position could be done to the much higher wind speeds during testing of 5m/s compared to the 1m/s of the back position testing.

In conclusion, the experiments from this thesis show that inflow velocity increases the closer to the center of the rotor. Therefor the best location in the horizontal plane for any wind sensor should be as far away from the center of the rotors as possible. This concludes that the center of the a multi-rotor would be the optimal location for most multi-rotor configurations. Additionally, this has the benefit of the sensor in line with the center of gravity of the multi-rotor making the dynamics easier for balancing out in post processing. In the vertical plane, the exact position is a little more unclear from these the tests. The majority of sensors should be placed at least one rotor diameter away from the rotor plane to reduce the inflow velocity to a more minimal level. Below there are examples of the flow diagram contours of a quad-rotor system that demonstrates regions of contamination. These graphs were derived from the results gained from this research. The first graph shows the contamination regions from the top-view and the levels of contamination for each region. The highest level of contamination occurs over the rotor disks and decreases further away, with the lowest level of contamination occurring at the center.

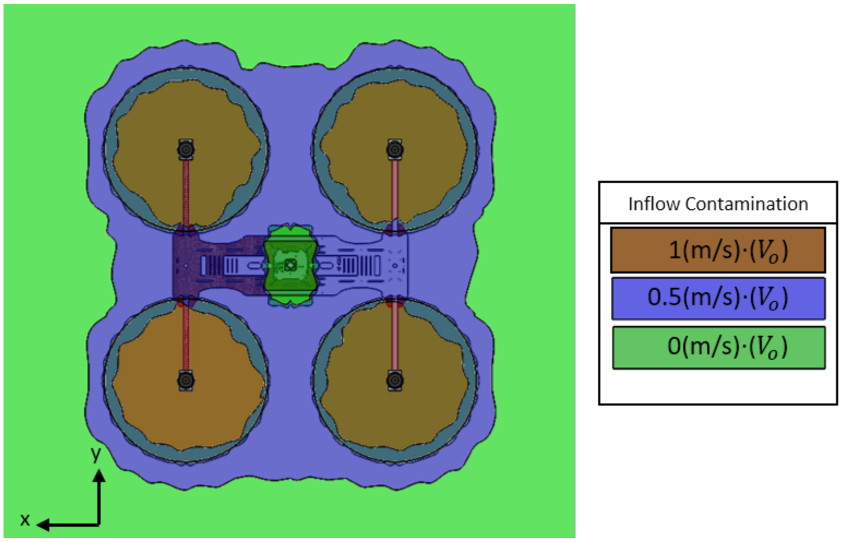

Figure 103: Multi-Rotor Flow-Field Top-View

Below is the same contour graph shown from the side-view. Showing the highest level of contamination above the rotor disks decreasing the further away in the vertical axis, in a triangle shape pattern, similar to the results acquired in single rotor experiment. The region in between the two rotors disk will have medium contamination until 24in above the rotor-plane and there the region will have the lowest contamination. As the region below the rotor plane is the down-wash will have high contamination throughout the region.

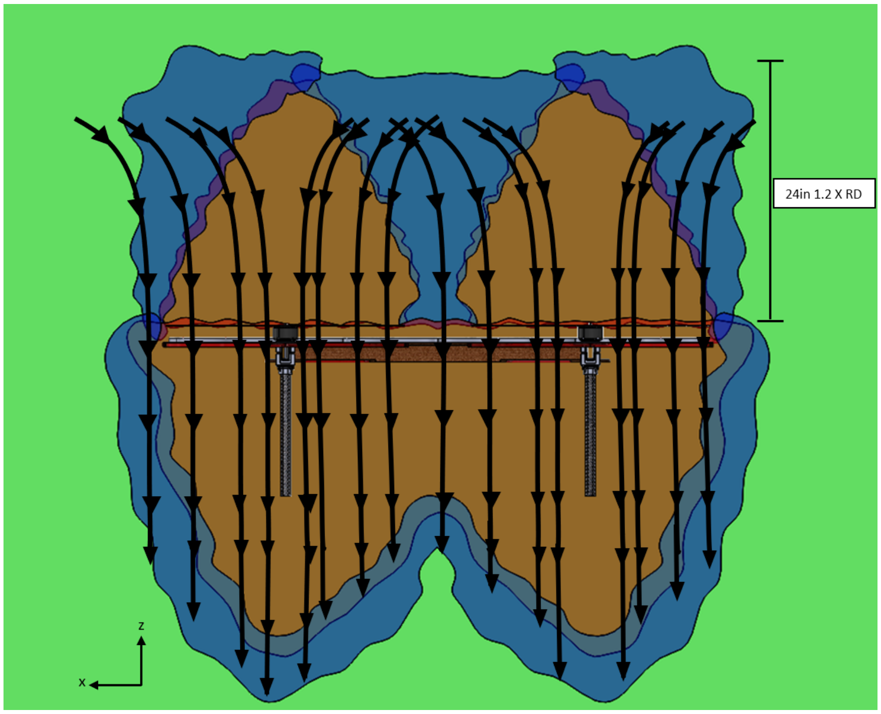

Figure 104: Multi-Rotor Flow-Field Mid-Plane Hover and Ambient

The next graph shows the flow-field of a multi-rotor when it is moving forward through the air with a incoming cross-flow. This graph was derived from the PIV results with the water tunnel on and the rotor angle at 30 degrees. The incoming cross-flow will get pulled into the inflow of the rotors, while the cross-flow that is about 1 rotor diameter above the rotors will pass over unaffected. While these flow-fields give a idea of the what the flow-field around a multi-rotor will look like it is not exact and more studies should be done to reinforce these graphs.

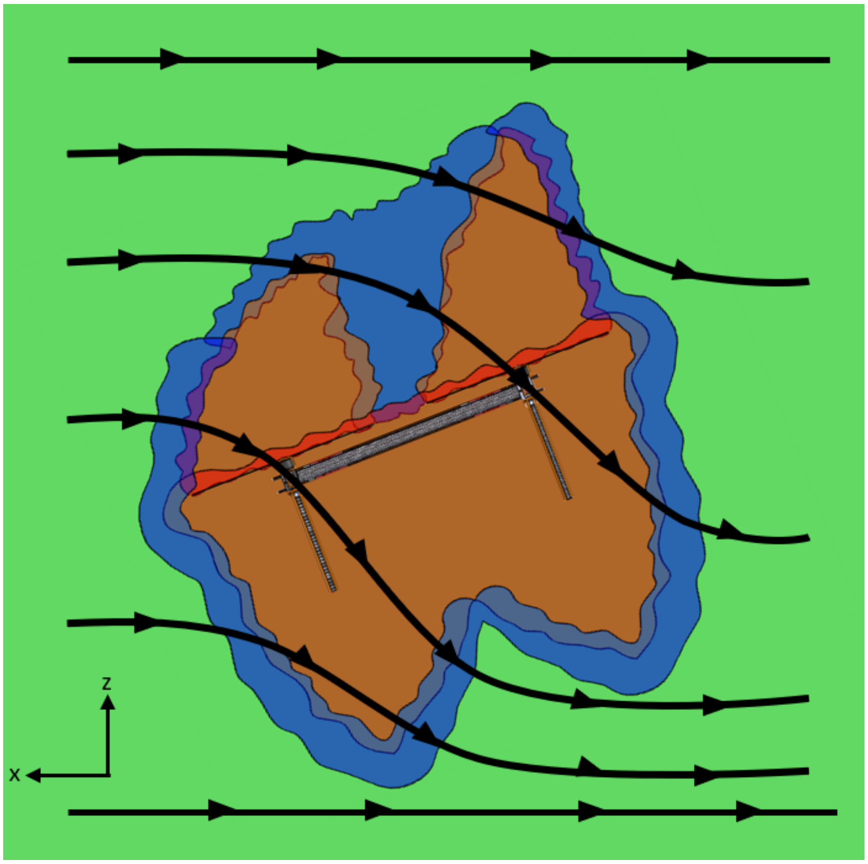

Figure 105: Multi-Rotor Flow-Field Mid-Plane Cross-Flow and Forward Angle

Future Work

For future endeavors there are several items that can be expanded upon. First, there should be additionally flight tests on the SKB system and the data compared to more accurate sensors such a meteorological towers. Additionally, these tests should be conducted in higher speeds to observe the limitations of the system. As well as testing different quadcopter platforms of varying sizes to solidify the one rotor diameter relationship. If available, more wind gusts should be observed to see the accuracy of the system during fast wind gusts. Also the effect of the vertical ascension should be calibrated out of the system so accurate data can be gathered while the SKB-1000 system is climbing. Overall the system should be refined with its own dedicated PCB data acquisition system instead using a breadboard. The gimbal system can also be improved with better motors to allow for a faster response time and smoother balancing. Aircraft dynamics could also be backed out and the sensor data could be corrected for this. The researcher recommends comparing non-gimbal data with aircraft dynamics corrected with post processing and a gimbal version to see which system acquires more accurate data. Finally, the PIV experiments should be repeated in a CFD a simulation to compare and evaluate the results of the PIV data.

REFERENCES

[1] Kevin A Adkins, Christopher J Swinford, Peter D Wambolt, and Gordon Bease, *Development of a sensor suite for atmospheric boundary layer measurement with a small multirotor unmanned aerial system*, International Journal of Aviation, Aeronautics, and Aerospace **7** (2020), no. 1, 4.

[2] Leon Battista Alberti, *The anemometer*, 2007.

[3] Stephen K Ammann, *Ultrasonic anemometer*, September 6 1994, US Patent 5,343,744.

[4] Alyssa Avery, Seabrook Whyte, James Brenner, Victoria Natalie, and Jamey Jacob, *Experimental measurement of flow field around a rotary wing unmanned aircraft for evaluation of onboard anemometer placement*, APS (2019), B17–004.

[5] Solmoz Kathleen Azartash-Namin, *Evaluation of low-cost multi-hole probes for atmospheric boundary layer investigation*, Ph.D. thesis, 2017.

[6] Gualtiero Badin and Fulvio Crisciani, *Variational formulation of fluid and geophysical fluid dynamics*, Springer, 2018.

[7] Boldmethod, *How a propeller generates thrust*, boldmethod.com (2019).

[8] John Brandt and Michael Selig, *Propeller performance data at low reynolds numbers*, 49th AIAA Aerospace Sciences Meeting including the New Horizons Forum and Aerospace Exposition, 2011, p. 1255.

[9] PAOLO Bruschi, MASSIMO Piotto, F Dell'Agnello, J Ware, and N Roy, *Wind speed and direction detection by means of solid-state anemometers embedded on small quadcopters*, Procedia Engineering **168** (2016), 802–805.

[10] Genevieve Comte-Bellot, *Hot-wire anemometry*, Annual review of fluid mechanics **8** (1976), no. 1, 209–231.

[11] HC Curtiss Jr and RM Mckillip Jr, *Studies of a flat wake rotor theory*, (1992).

[12] Geoffrey W Donnell, Jordan A Feight, Nate Lannan, and Jamey D Jacob, *Wind characterization using onboard imu of suas*, 2018 Atmospheric Flight Mechanics Conference, 2018, p. 2986.

[13] Fernando Carbajo Fuertes, Lionel Wilhelm, and Fernando Porté-Agel, *Multirotor uav-based platform for the measurement of atmospheric turbulence: Validation and signature detection of tip vortices of wind turbine blades*, Journal of Atmospheric and Oceanic Technology **36** (2019), no. 6, 941–955.

[14] Benjamin L Hemingway, Amy E Frazier, Brian R Elbing, and Jamey D Jacob, *Vertical sampling scales for atmospheric boundary layer measurements from small unmanned aircraft systems (suas)*, Atmosphere **8** (2017), no. 9, 176.

[15] Wayne Johnson, *Helicopter theory*, Courier Corporation, 2012.

[16] J Gordon Leishman, *A history of helicopter flight*, sl: University of Maryland, Available in: http://terpconnect. umd. edu/˜ leishman/Aero/history. html (2000).

[17] S Martin, J Bange, and F Beyrich, *Meteorological profiling of the lower troposphere using the research uav" m2av carolo"*, Atmospheric Measurement Techniques **4** (2011), no. 4, 705.

[18] William Edgar Knowles Middleton and Athelstan F Spilhaus, *Meteorological instruments*, University of Toronto Press, 2019.

[19] Robert Niemiec and Farhan Gandhi, *A comparison between quadrotor flight configurations*, (2016).

[20] Gordana Ostojić, Stevan Stankovski, Branislav Tejić, Nikola ukić, and Sran Tegeltija, *Design, control and application of quadcopter*, International Journal of Industrial Engineering and Management **6** (2015), no. 1, 43–48.

[21] Ross T Palomaki, Nathan T Rose, Michael van den Bossche, Thomas J Sherman, and Stephan FJ De Wekker, *Wind estimation in the lower atmosphere using multirotor aircraft*, Journal of Atmospheric and Oceanic Technology **34** (2017), no. 5, 1183–1191.

[22] Parag Parihar, Priyanshu Bhawsar, and Piyush Hargod, *Design & development analysis of quadcopter*, Compusoft **5** (2016), no. 6, 2128.

[23] Santiago Pindado, Javier Pérez, and Sergio Avila-Sanchez, *On cup anemometer rotor aerodynamics*, Sensors **12** (2012), no. 5, 6198–6217.

[24] Gerrit Anke Rau, *Two new technologies to measure the turbulent wind vector aboard small research uav*, Ph.D. thesis, 2016.

[25] Nikolaus Rott, *Note on the history of the reynolds number*, Annual review of fluid mechanics **22** (1990), no. 1, 1–12.

[26] Hermann Schlichting and Klaus Gersten, *Boundary-layer theory*, Springer, 2016.

[27] Roland B Stull, *Mean boundary layer characteristics*, An Introduction to Boundary Layer Meteorology, Springer, 1988, pp. 1–27.

[28] Y Tan, J Chen, T Norton, Jie Wang, X Liu, S Yang, and Y Zheng, *The computational fluid dynamic modeling of downwash flow field for a six-rotor uav*, Frontiers of Agricultural Science and Engineering **5** (2018), no. 2.

[29] Mark A Taylor, *Performance of a propeller-vane compared to two cup anemometers.*

[30] Ryan L Thorpe, Matthew McCrink, and James W Gregory, *Measurement of unsteady gusts in an urban wind field using a uav-based anemometer*, 2018 Applied Aerodynamics Conference, 2018, p. 4218.

[31] Drone Versus, *Compare drones by speed*, droneversus.com (2019).

[32] Quentin R Wald, *The aerodynamics of propellers*, Progress in Aerospace Sciences **42** (2006), no. 2, 85–128.

[33] Qiang Wang, *The current research status and prospect of multi-rotor uav*, Journal of Mechanical and Civil Engineering **14** (2017), no. 4, 31–35.

[34] Seabrook Whyte and Jamey Jacob, *Experimental measurement of flow field around a rotary wing unmanned aircraft*, Bulletin of the American Physical Society **63** (2018).

[35] S Yoon and PV Diaz, *High-fidelity computational aerodynamics of multi-rotor unmanned aerial vehicles*, AIAA SciTech (2018), 2018–1266.

APPENDICES

Flow-Field Averaged Velocity Fields

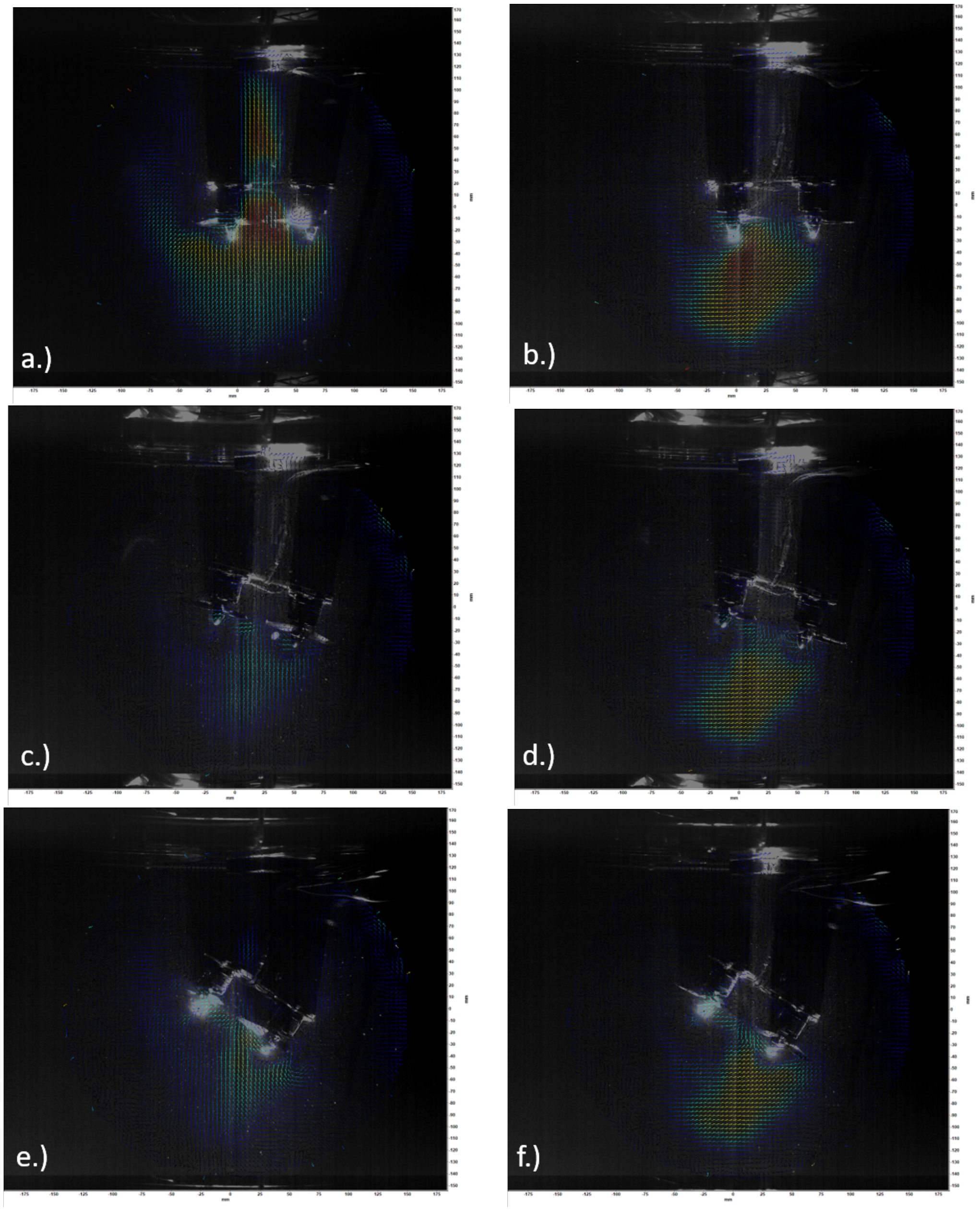

Figure 106: Quad X Hub: a.) (0m/s, 0°), b.) (0.5m/s, 0°), c.) (0m/s, 15°), d.) (0.5m/s, 15°), e.) (0m/s, 30°), f.) (0.5m/s, 30°)

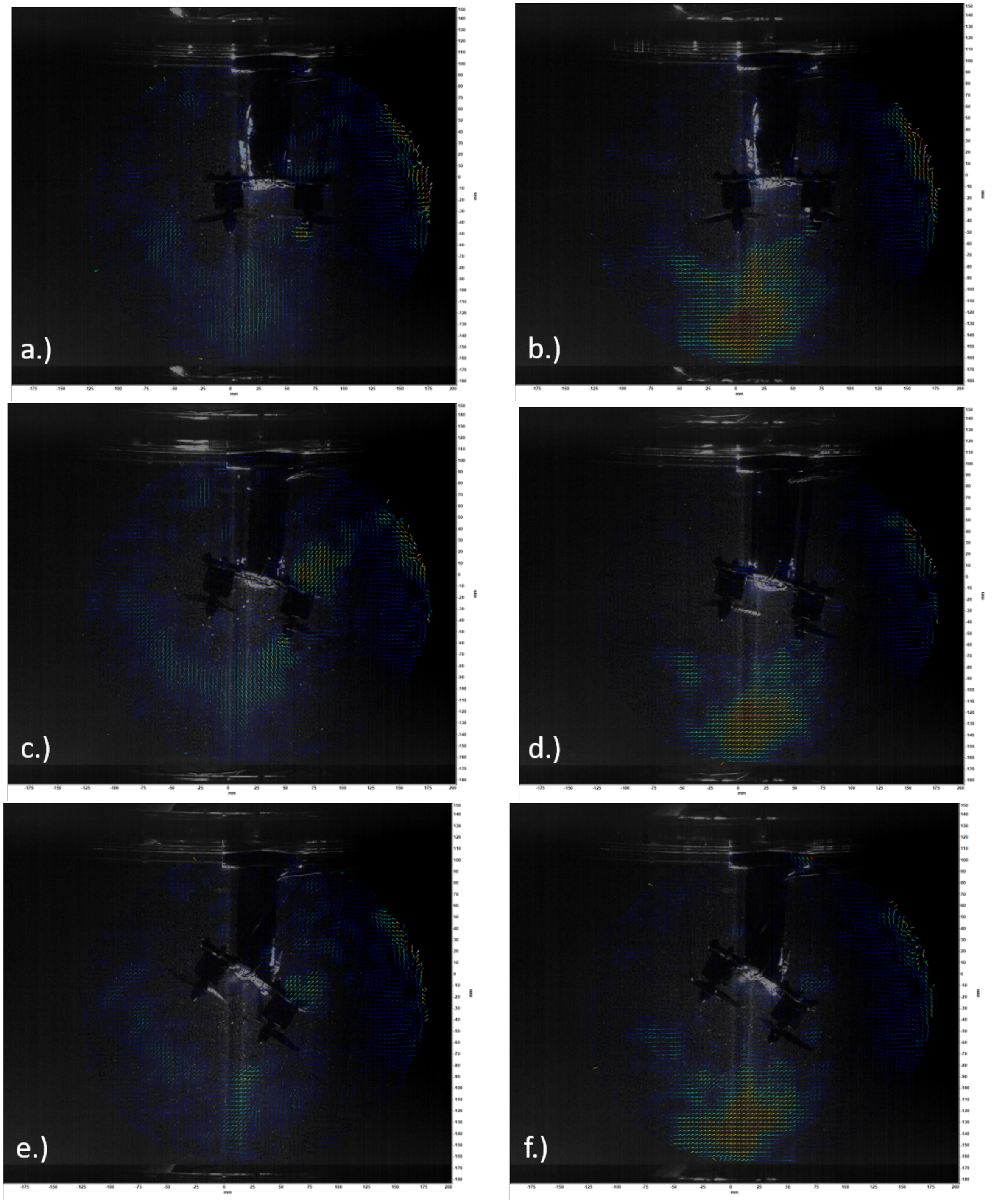

Figure 107: Quad X Mid-plane: a.) (0m/s, 0°), b.) (0.5m/s, 0°), c.) (0m/s, 15°), d.) (0.5m/s, 15°), e.) (0m/s, 30°), f.) (0.5m/s, 30°)

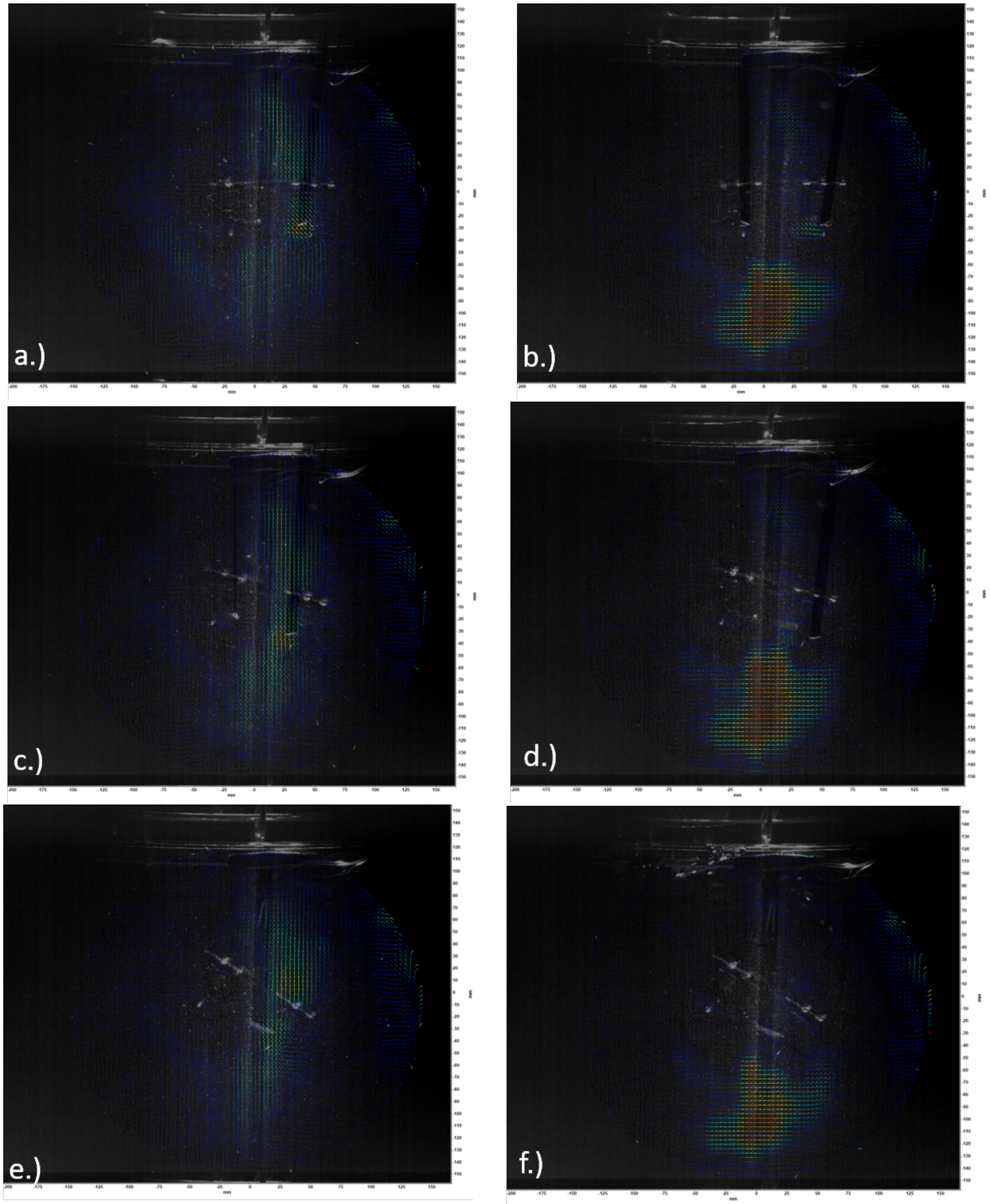

Figure 108: Quad X Tip: a.) (0m/s, 0°), b.) (0.5m/s, 0°), c.) (0m/s, 15°), d.) (0.5m/s, 15°), e.) (0m/s, 30°), f.) (0.5m/s, 30°

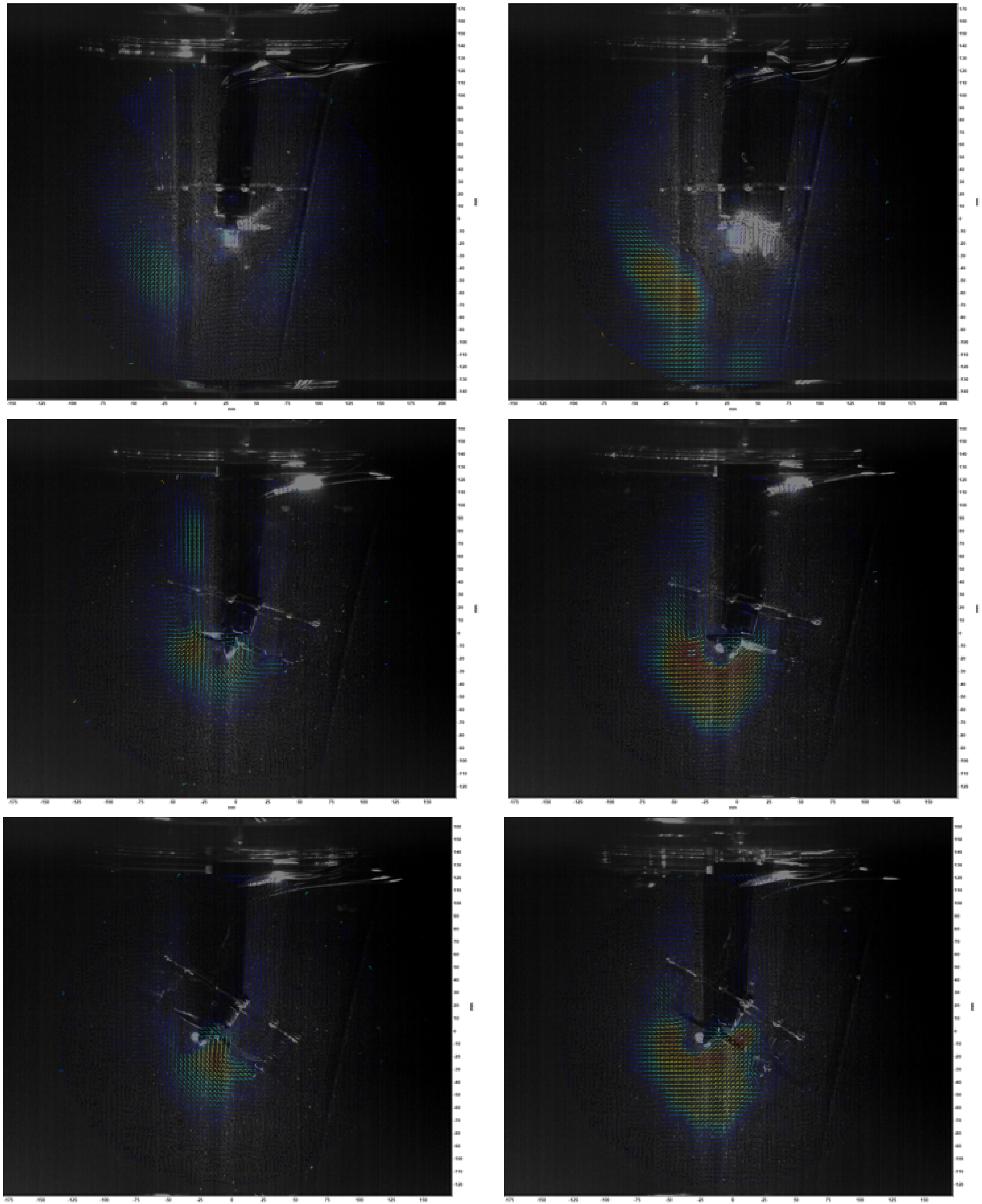

Figure 109: Quad + Hub: a.) (0m/s, 0°), b.) (0.5m/s, 0°), c.) (0m/s, 15°), d.) (0.5m/s, 15°), e.) (0m/s, 30°), f.) (0.5m/s, 30°

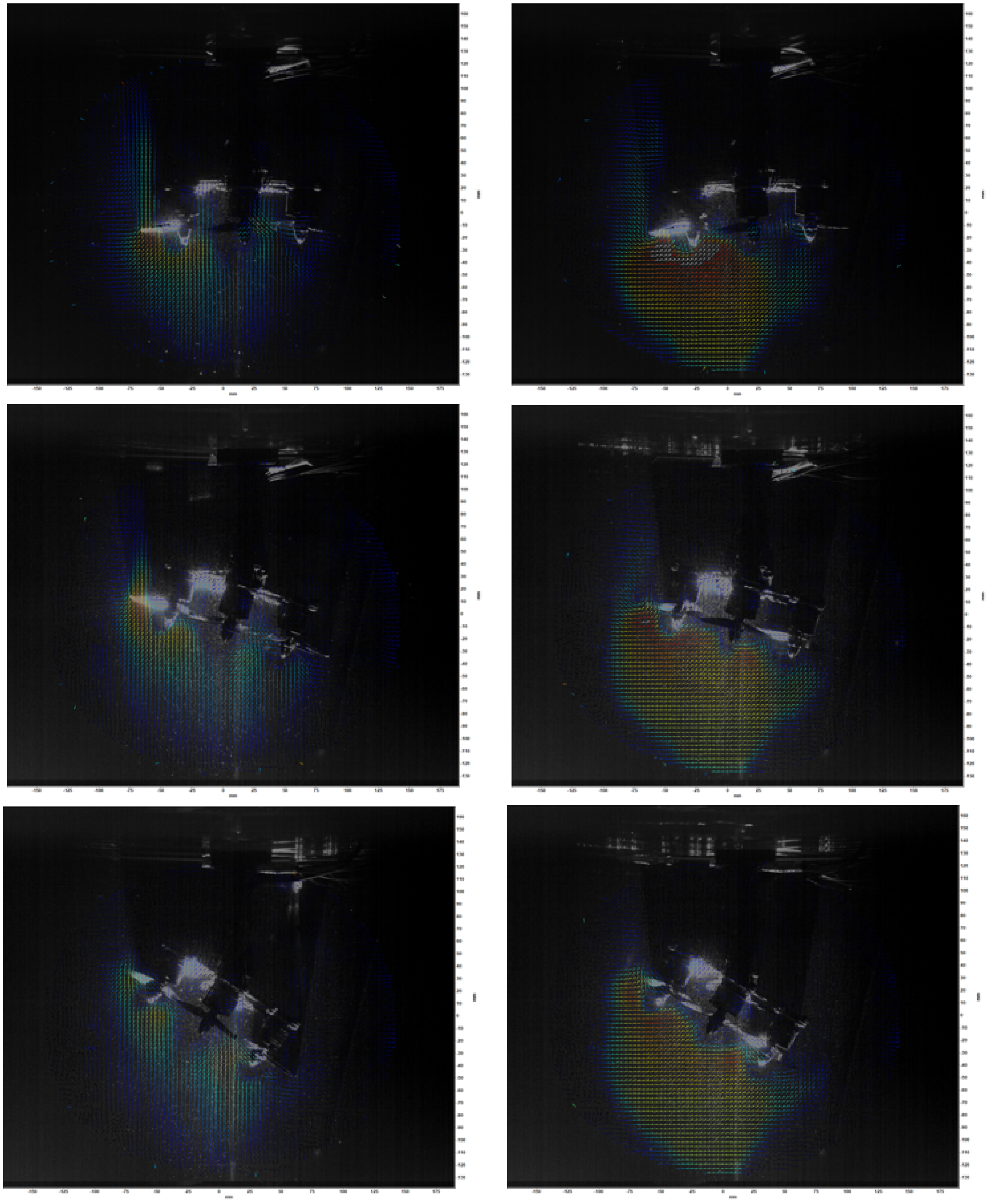

Figure 110: Quad + Mid-plane: a.) (0m/s, 0°), b.) (0.5m/s, 0°), c.) (0m/s, 15°), d.) (0.5m/s, 15°), e.) (0m/s, 30°), f.) (0.5m/s, 30°

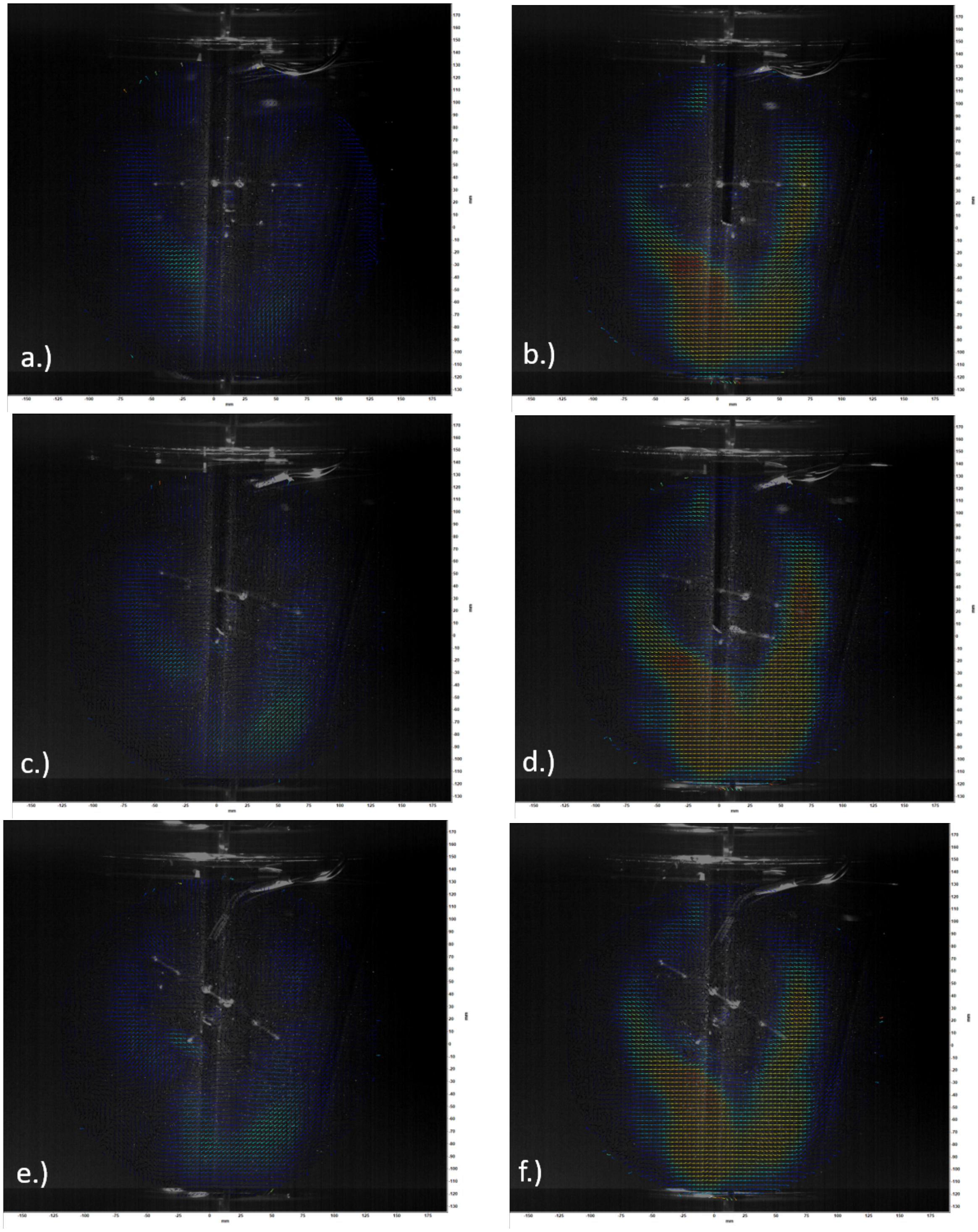

Figure 111: Quad X Tip: a.) (0m/s, 0°), b.) (0.5m/s, 0°), c.) (0m/s, 15°), d.) (0.5m/s, 15°), e.) (0m/s, 30°), f.) (0.5m/s, 30°

Vorticity

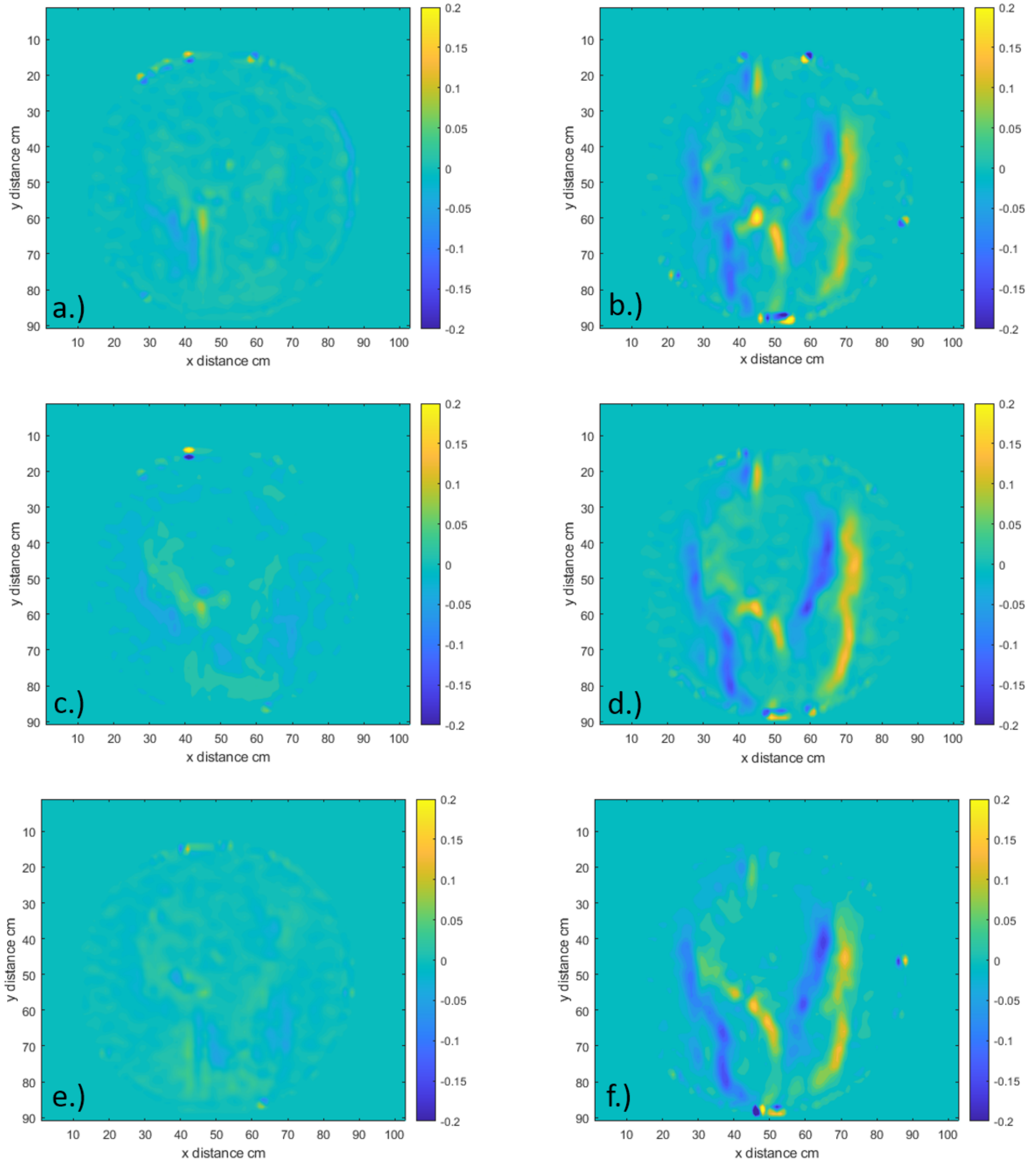

Figure 112: Vorticity Profile Quad + Tip: a.) (0m/s, 0°), b.) (0.5m/s, 0°), c.) (0m/s, 15°), d.) (0.5m/s, 15°), e.) (0m/s, 30°), f.) (0.5m/s, 30°)

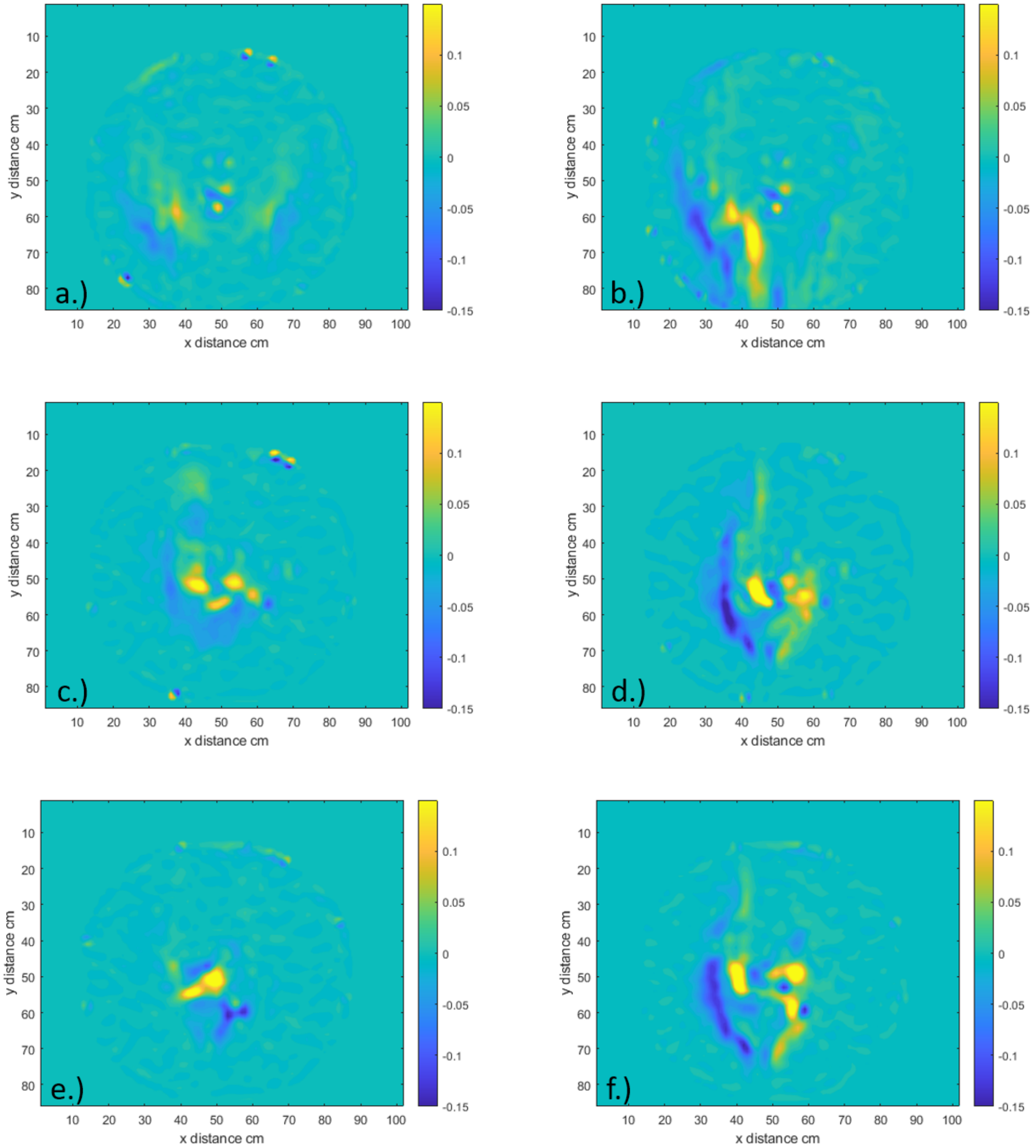

Figure 113: Vorticity Profile Quad + Hub: a.) (0m/s, 0°), b.) (0.5m/s, 0°), c.) (0m/s, 15°), d.) (0.5m/s, 15°), e.) (0m/s, 30°), f.) (0.5m/s, 30°)

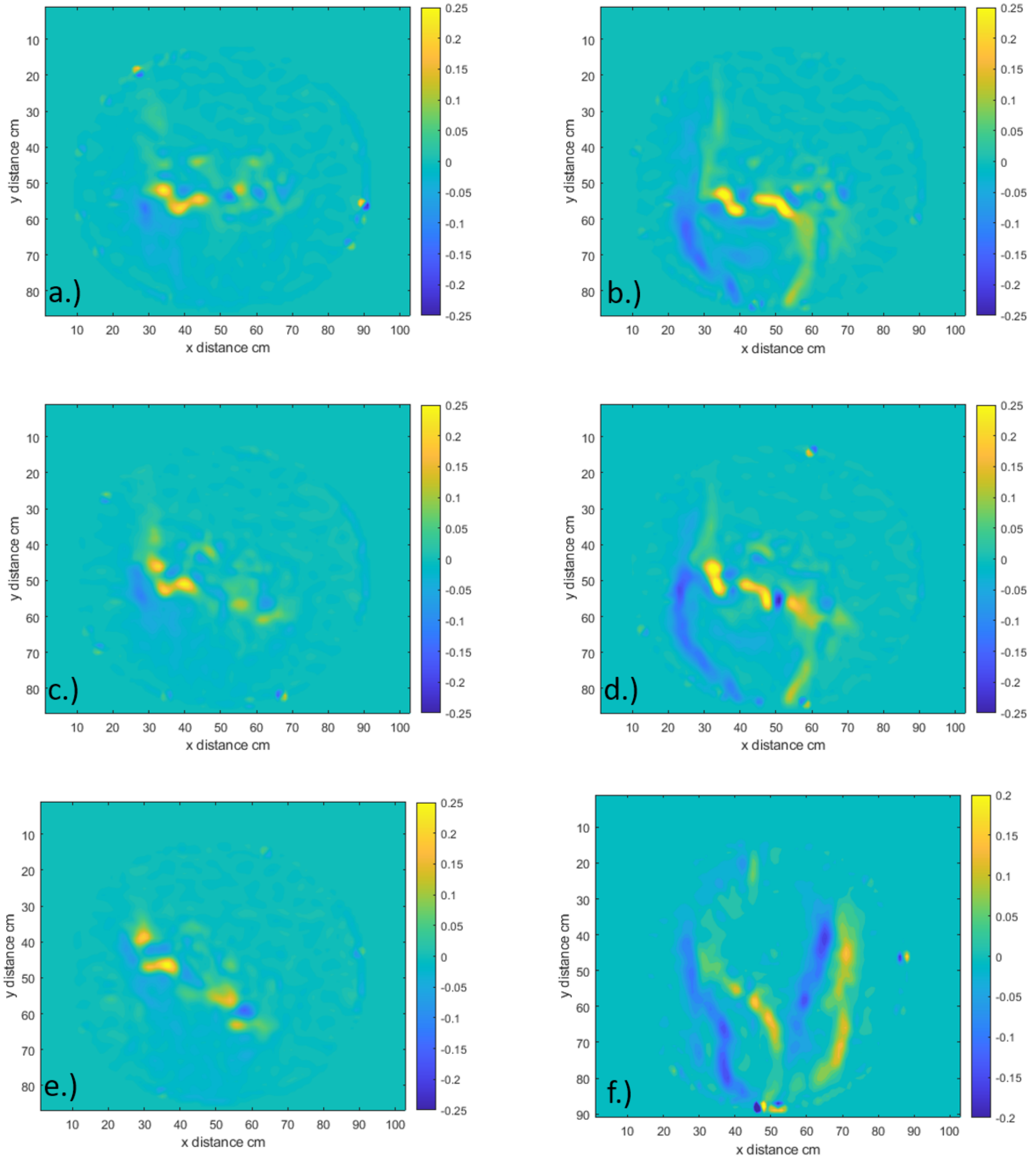

Figure 114: Vorticity Profile Quad + Mid-plane: a.) (0m/s, 0°), b.) (0.5m/s, 0°), c.) (0m/s, 15°), d.) (0.5m/s, 15°), e.) (0m/s, 30°), f.) (0.5m/s, 30°)

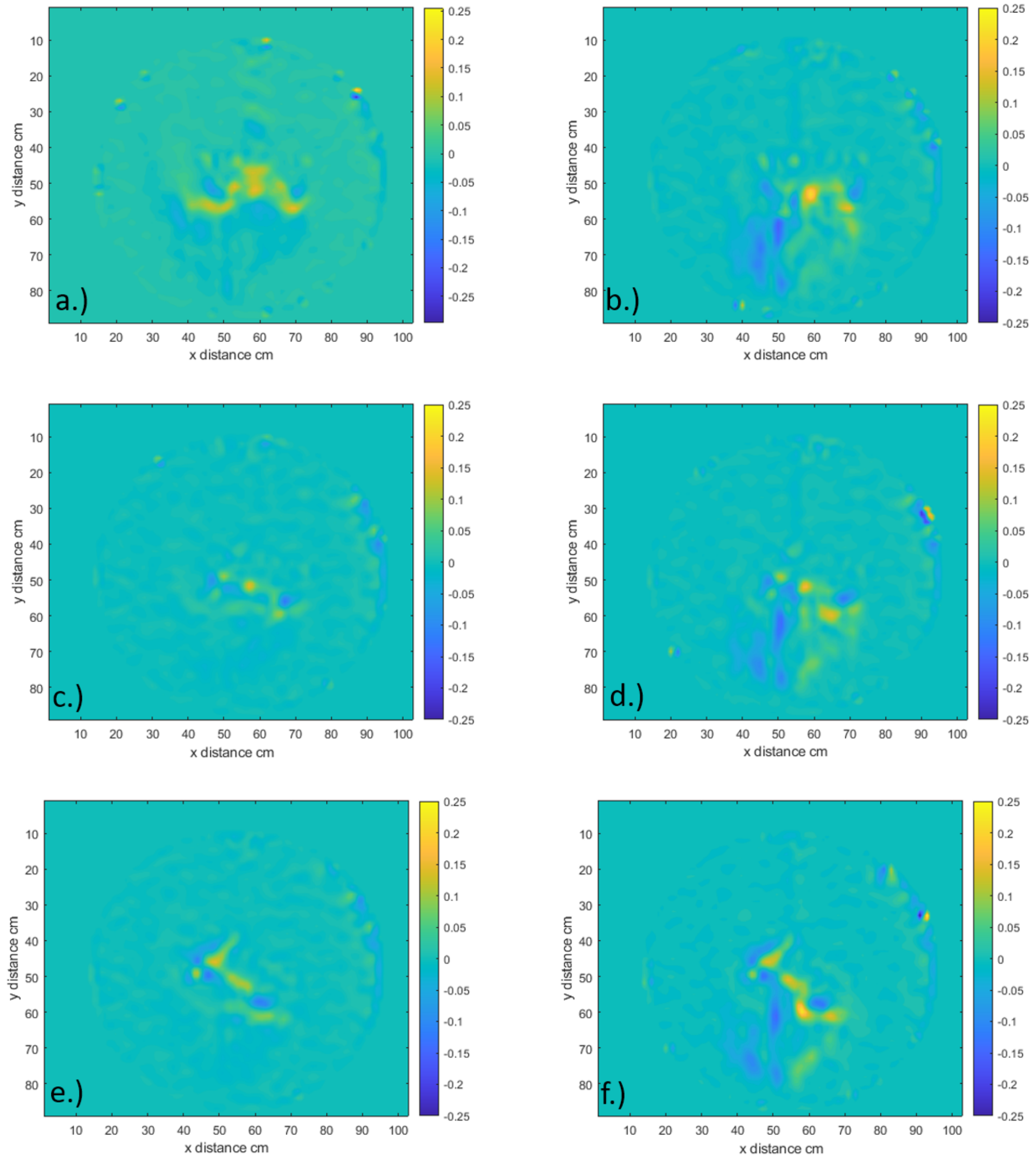

Figure 115: Vorticity Profile Quad X Hub: a.) (0m/s, 0°), b.) (0.5m/s, 0°), c.) (0m/s, 15°), d.) (0.5m/s, 15°), e.) (0m/s, 30°), f.) (0.5m/s, 30°)

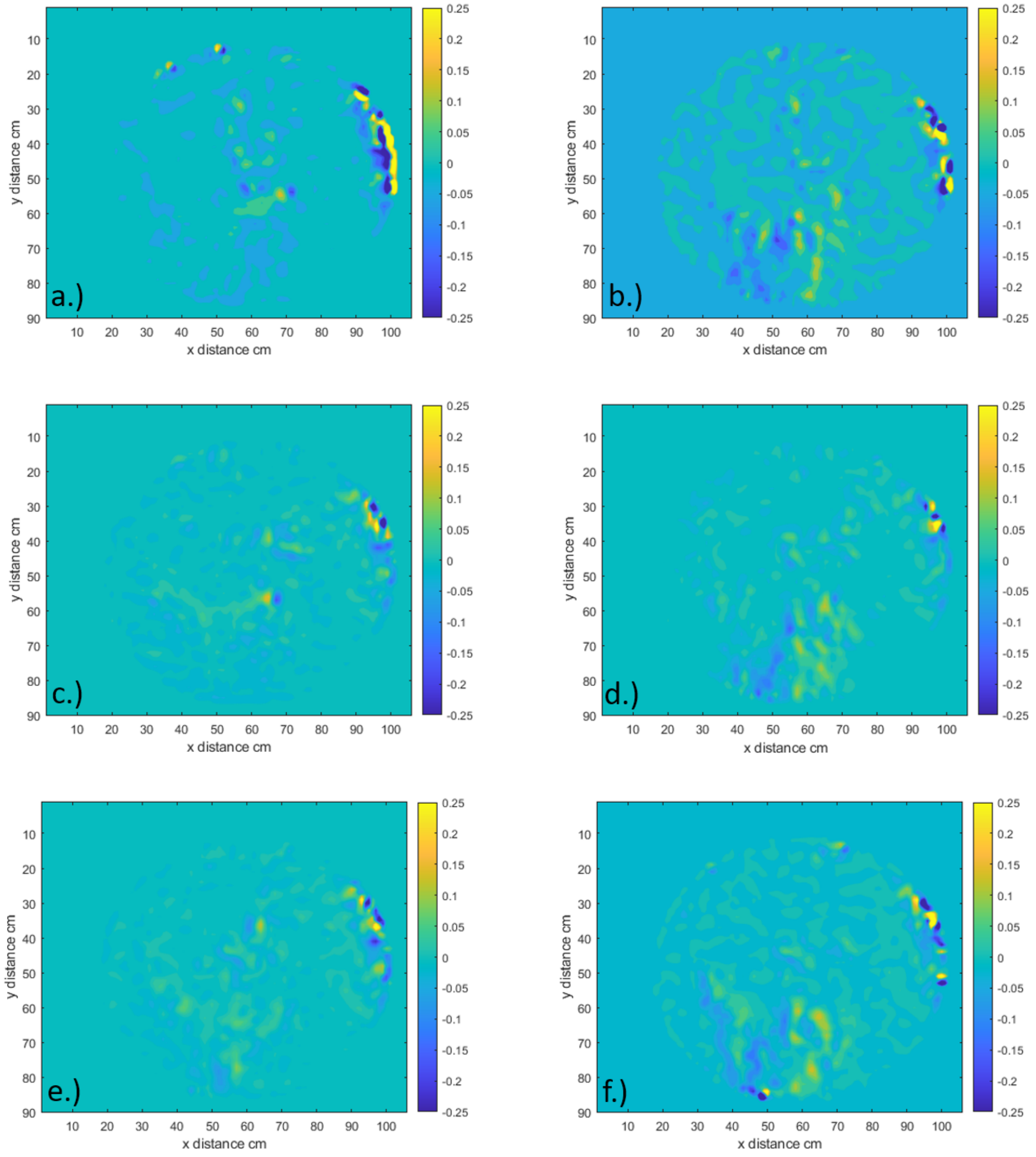

Figure 116: Vorticity Profile Quad X Mid-plane: a.) (0m/s, 0°), b.) (0.5m/s, 0°), c.) (0m/s, 15°), d.) (0.5m/s, 15°), e.) (0m/s, 30°), f.) (0.5m/s, 30°)

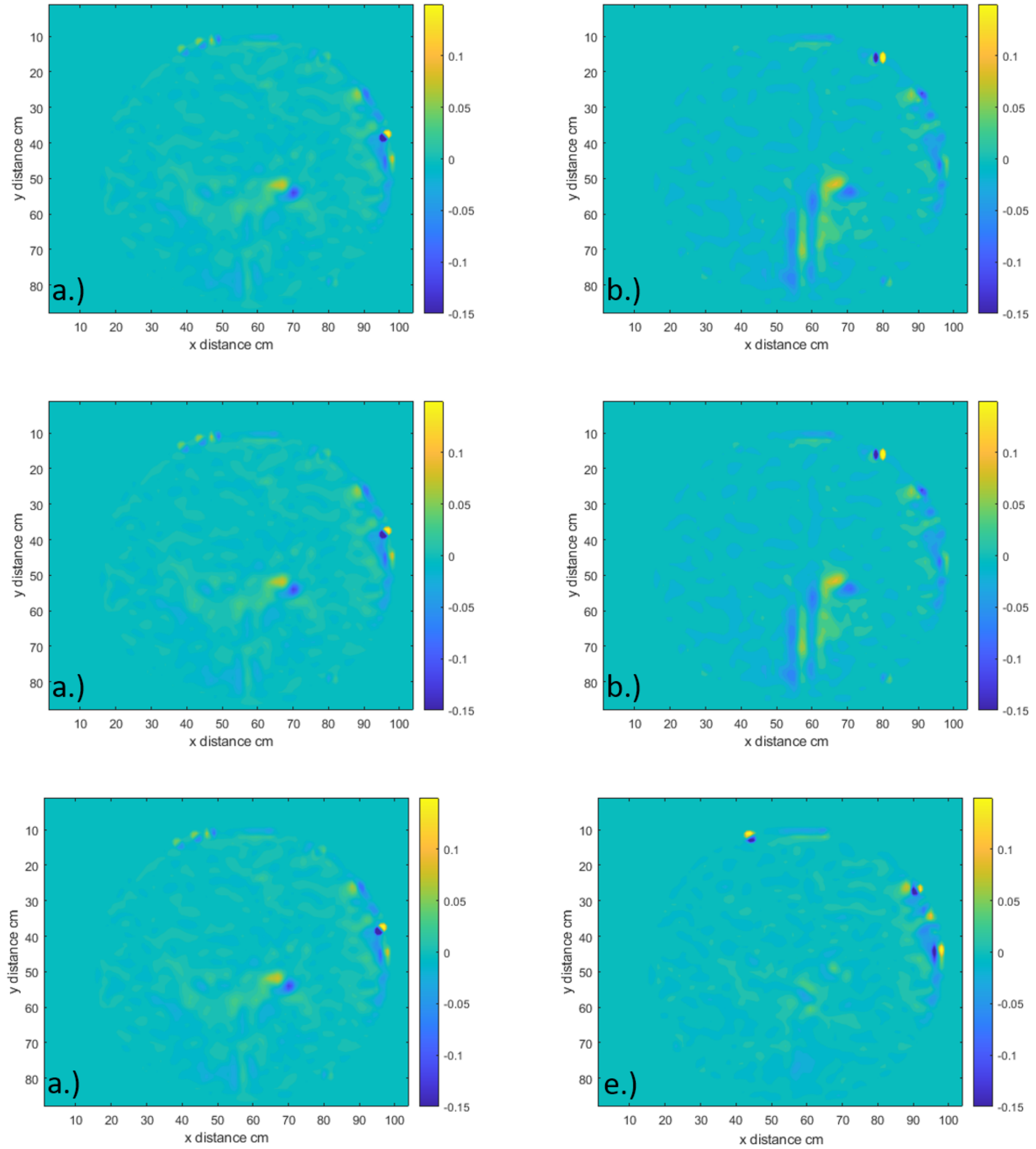

Figure 117: Vorticity Profile Quad X Mid-plane: a.) (0m/s, 0°), b.) (0.5m/s, 0°), c.) (0m/s, 15°), d.) (0.5m/s, 15°), e.) (0m/s, 30°), f.) (0.5m/s, 30°)

Correlation Coefficient

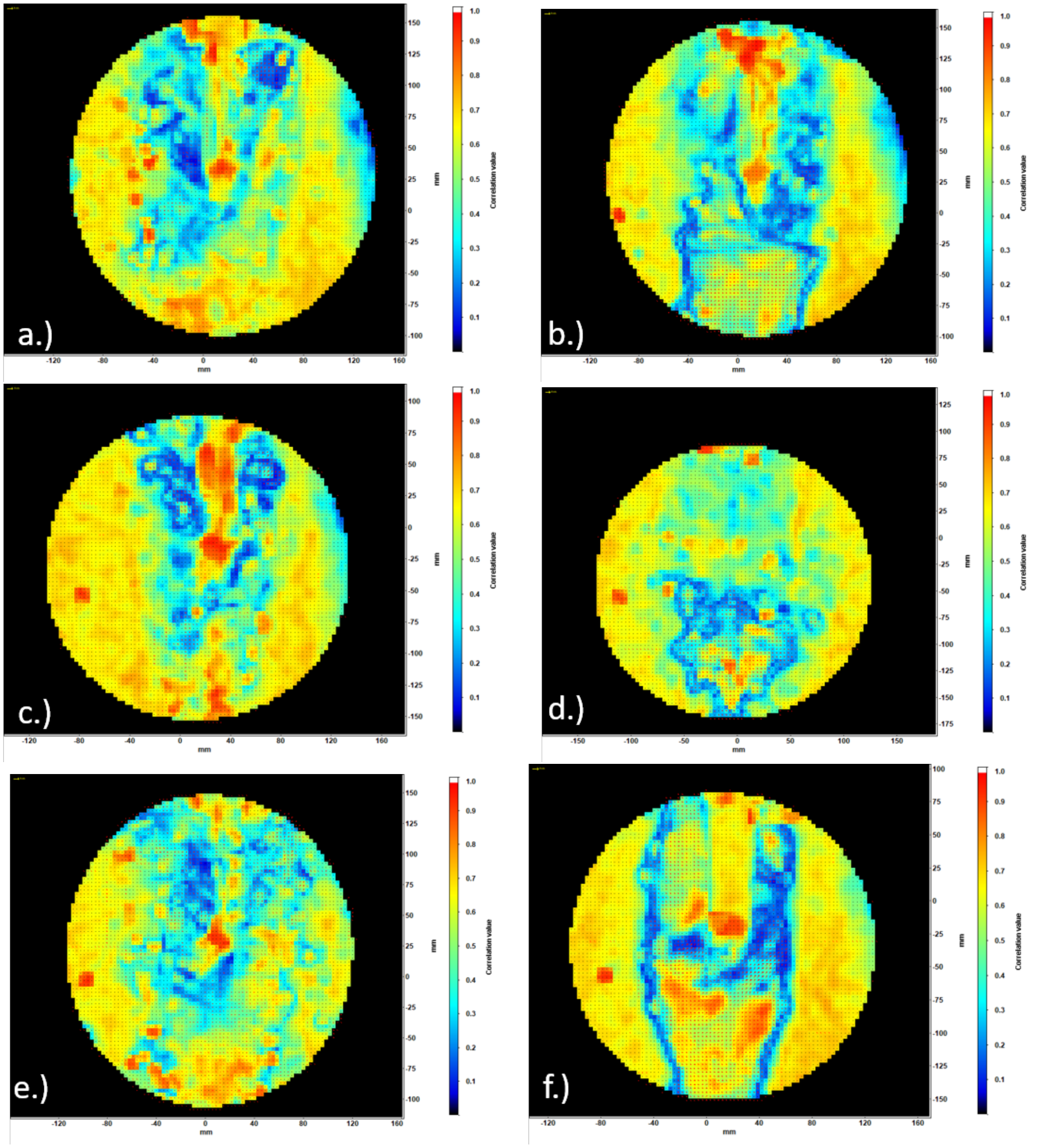

Figure 118: Correlation Coefficient Dual Perp Mid-plane: a.) (0m/s, 0°), b.) (0.5m/s, 0°), c.) (0m/s, 15°), d.) (0.5m/s, 15°), e.) (0m/s, 30°), f.) (0.5m/s, 30°)

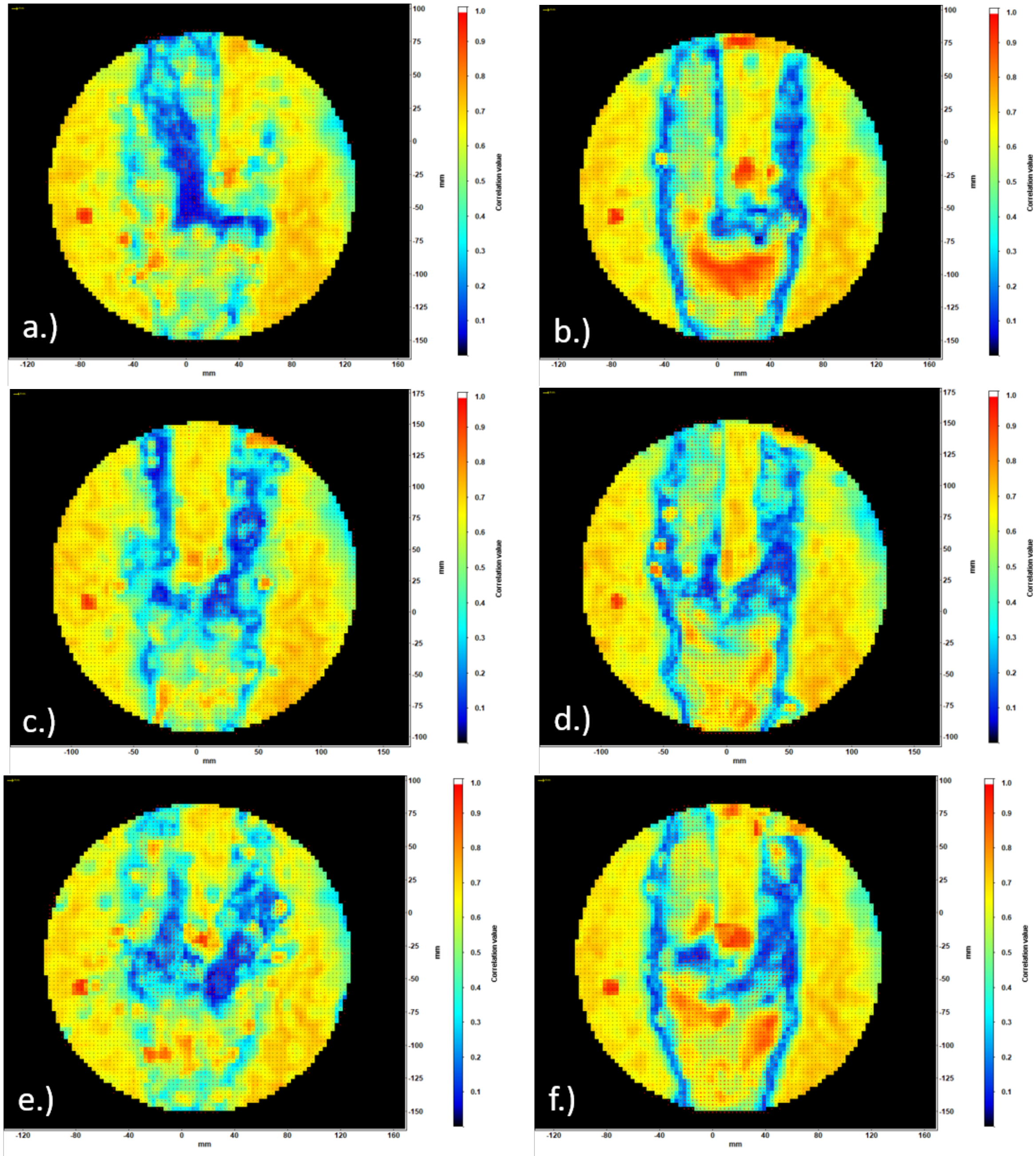

Figure 119: Correlation Coefficient Dual Perp Hub: a.) (0m/s, 0°), b.) (0.5m/s, 0°), c.) (0m/s, 15°), d.) (0.5m/s, 15°), e.) (0m/s, 30°), f.) (0.5m/s, 30°)

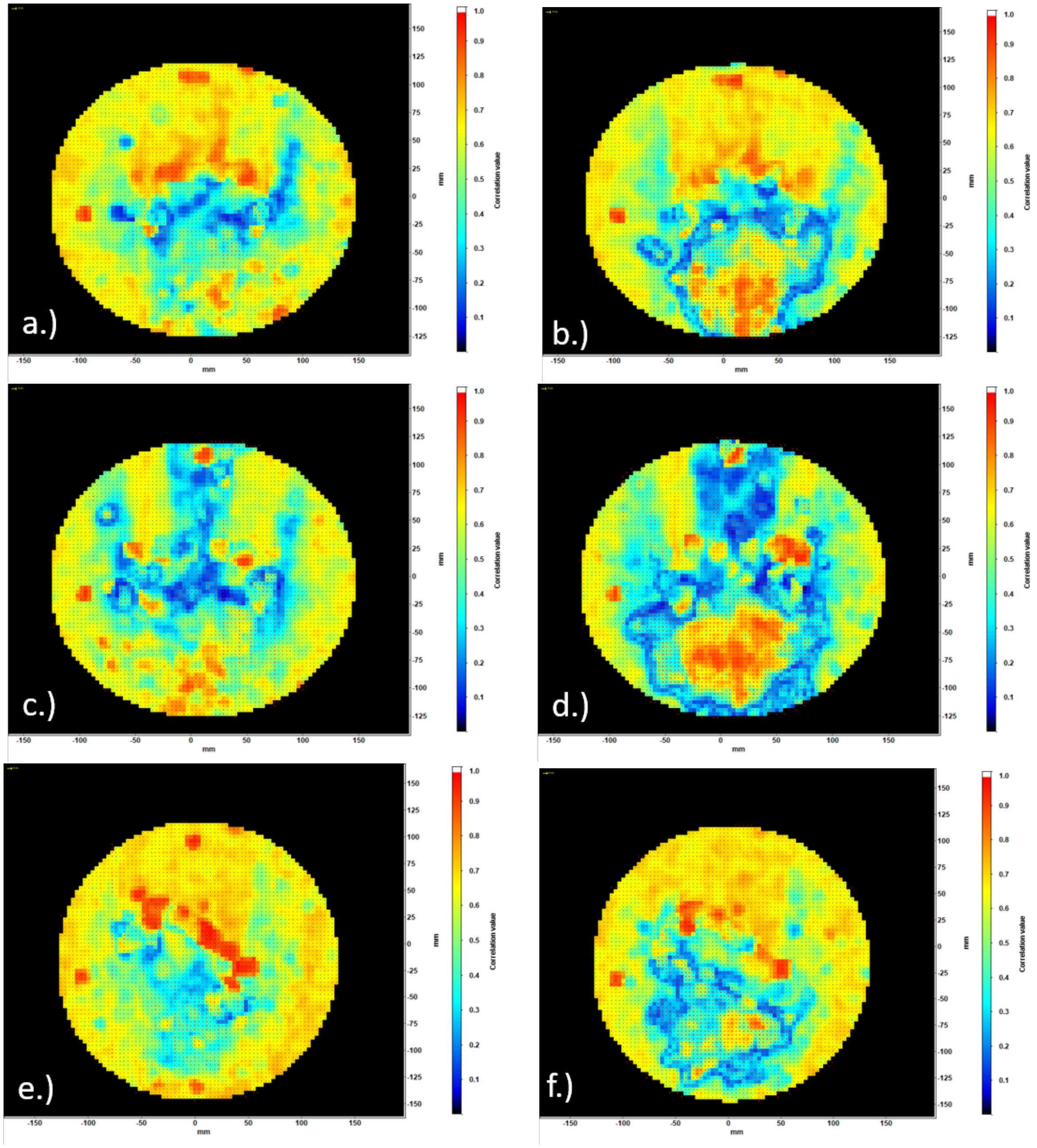

Figure 120: Correlation Coefficient Dual Para Hub: a.) (0m/s, 0°), b.) (0.5m/s, 0°), c.) (0m/s, 15°), d.) (0.5m/s, 15°), e.) (0m/s, 30°), f.) (0.5m/s, 30°)

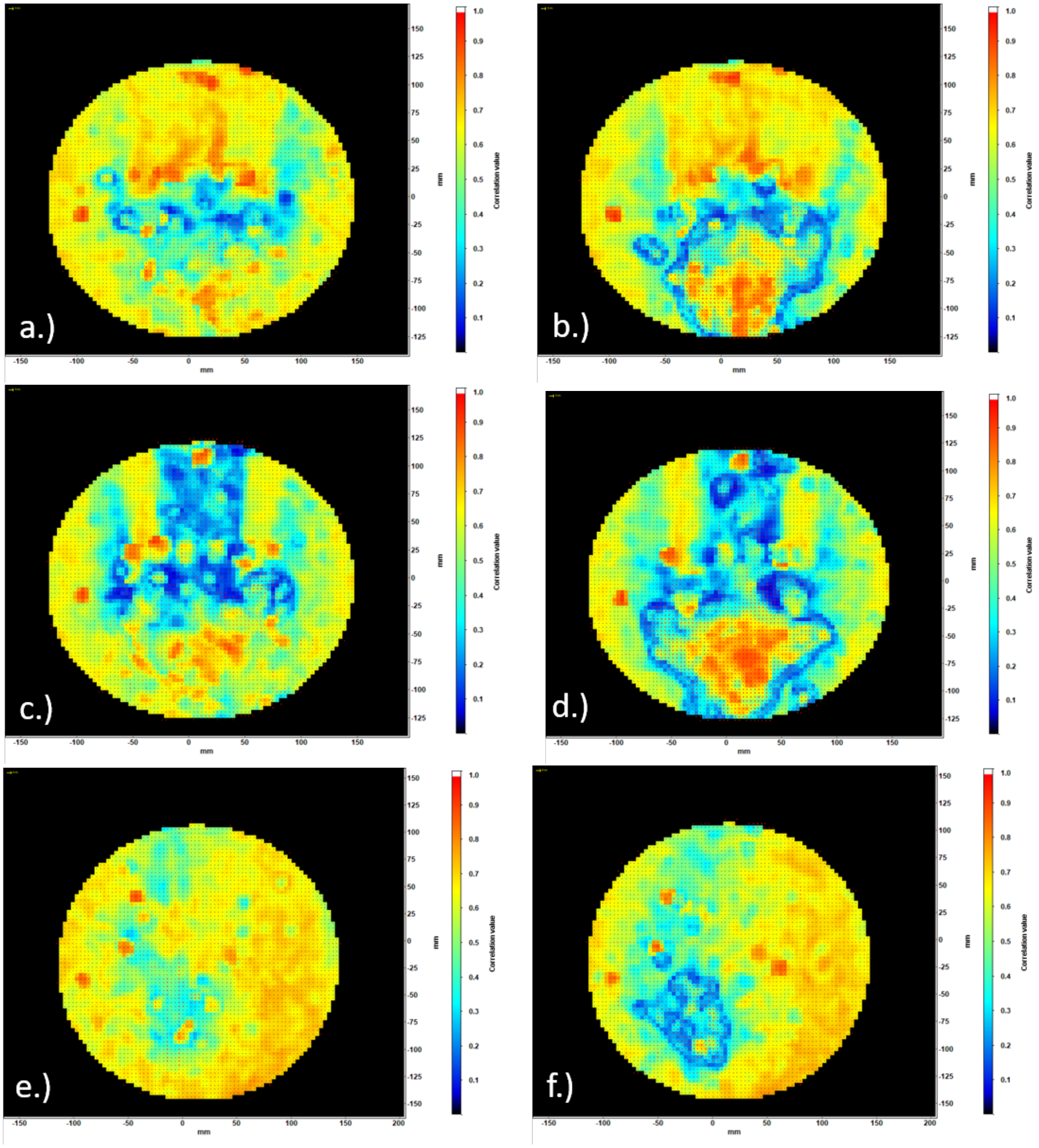

Figure 121: Correlation Coefficient Dual Para Tip: a.) (0m/s, 0°), b.) (0.5m/s, 0°), c.) (0m/s, 15°), d.) (0.5m/s, 15°), e.) (0m/s, 30°), f.) (0.5m/s, 30°)

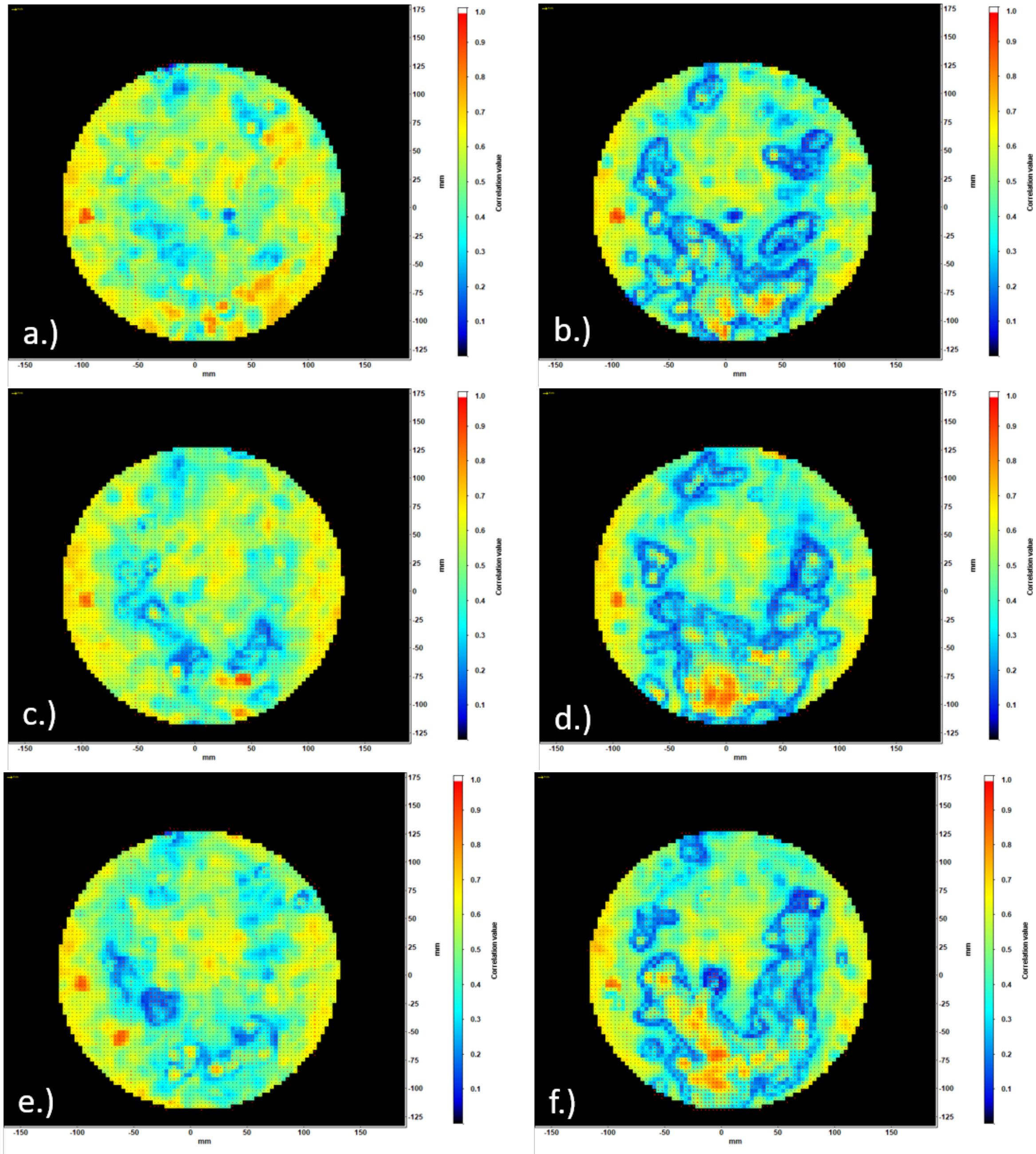

Figure 122: Correlation Coefficient Quad Plus Tip: a.) (0m/s, 0°), b.) (0.5m/s, 0°), c.) (0m/s, 15°), d.) (0.5m/s, 15°), e.) (0m/s, 30°), f.) (0.5m/s, 30°)

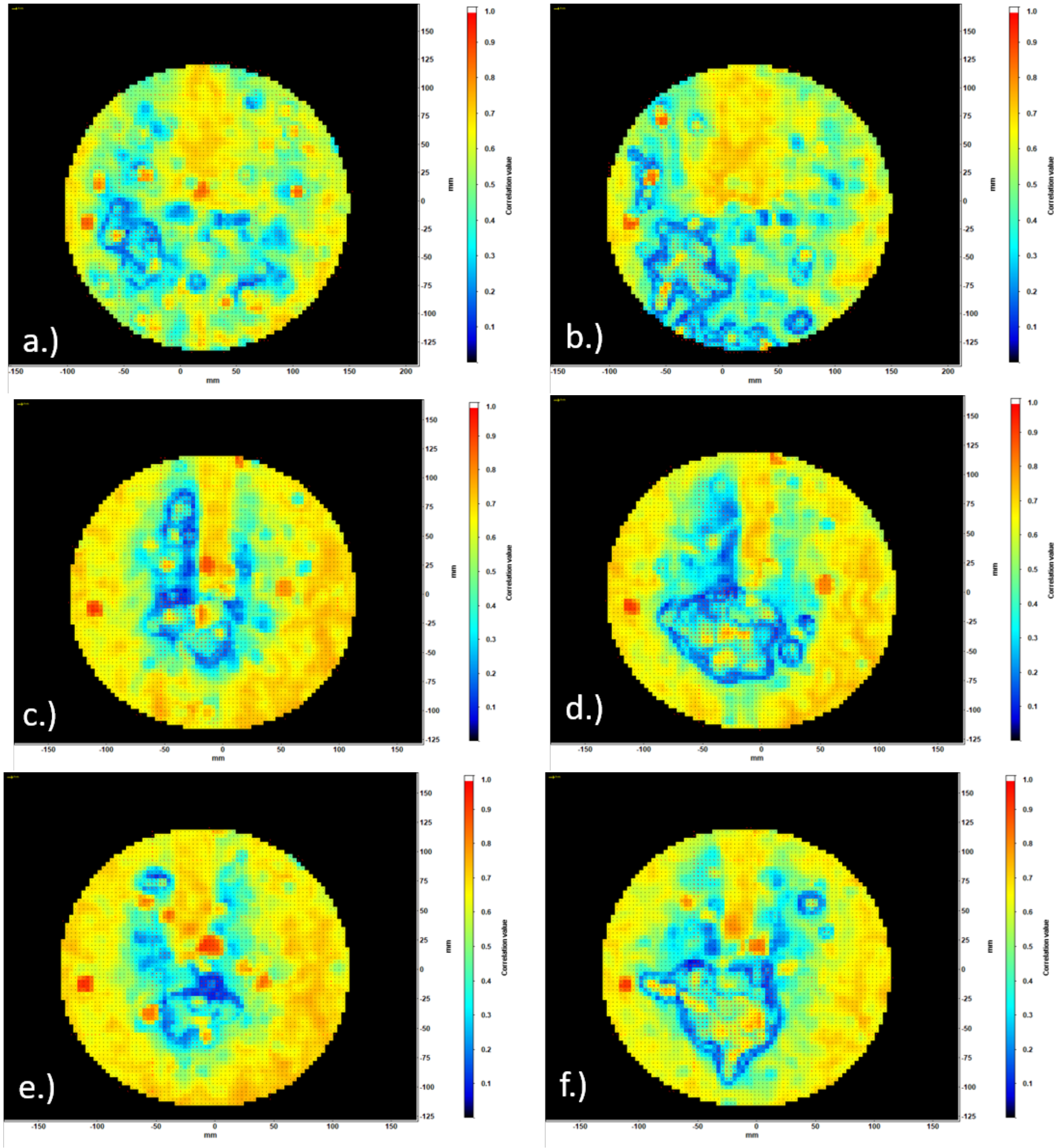

Figure 123: Correlation Coefficient Quad Plus Hub: a.) (0m/s, 0°), b.) (0.5m/s, 0°), c.) (0m/s, 15°), d.) (0.5m/s, 15°), e.) (0m/s, 30°), f.) (0.5m/s, 30°)

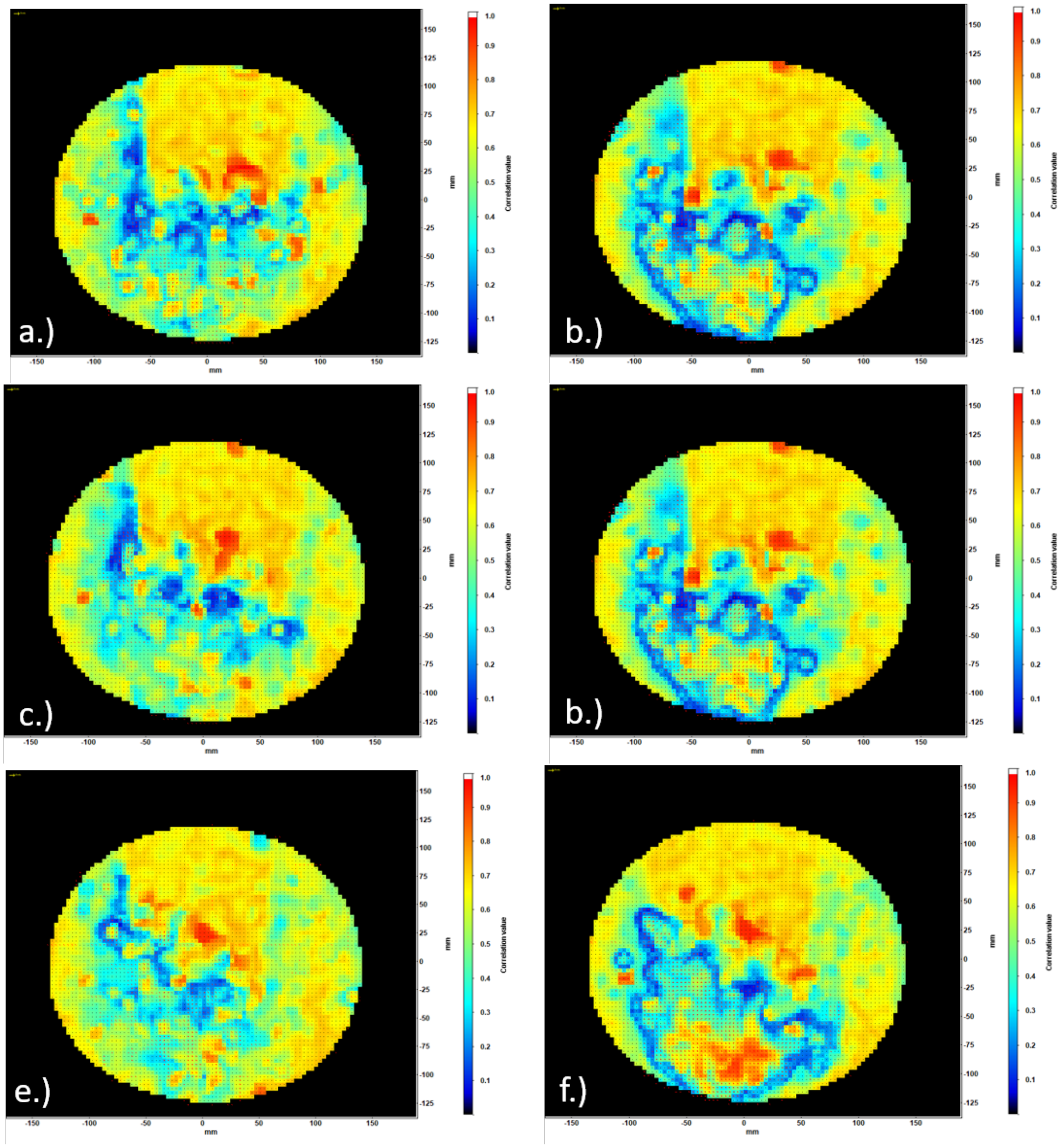

Figure 124: Correlation Coefficient Quad Plus Mid-plane: a.) (0m/s, 0°), b.) (0.5m/s, 0°), c.) (0m/s, 15°), d.) (0.5m/s, 15°), e.) (0m/s, 30°), f.) (0.5m/s, 30°)

Anemometer Sensor Code

```
clc
clear
close␣all
[file,␣path]␣=␣uigetfile(’*.*’,␣’Select␣Trisonica␣Log␣File’);␣%SKB␣Data␣File␣to␣parse
filename␣=fullfile(path,␣file);
data␣=␣readmatrix(filename);
nrows␣=␣length((data(:,1)));
i␣=␣1:nrows;
[file1,␣path1]␣=␣uigetfile(’*.*’,␣’Select␣Tower␣File’);␣%Tower␣Data␣File␣to␣parse
filename1␣=fullfile(path1,␣file1);
data1␣=␣readmatrix(filename1);
nrows1␣=␣length((data1(:,1)));
j␣=␣1:nrows1;
Tri_2D␣=␣(data(i,1));
Tri_BT␣=␣(data(i,2));
Tri_Time␣=␣(data(i,3));
Young_2D␣=␣(data1(j,1));
Young_Time␣=␣(data1(j,2));
Young_BT␣=␣(data1(j,3));
%Applies␣to␣both␣sets
data(isnan(data))␣=␣-1;
nrows␣=␣length(data(:,1));
data1(isnan(data1))␣=␣-1;
nrows1␣=␣length(data1(:,1));
%%Trisonica
%Do␣the␣following␣for␣each␣set
```

```
Interpcount=0;
␣␣for␣i=1:nrows
␣␣␣␣␣␣␣␣ZuluTime␣=␣data(i,3);
␣␣␣␣␣␣␣␣time␣=␣data(i,2);
␣␣␣␣if(ZuluTime~=-1)
␣␣␣␣␣␣␣␣Interpcount=Interpcount+1;
␣␣␣␣␣␣␣␣InterpData(Interpcount,1)=time;␣␣␣%␣Sensor␣board␣time
␣␣␣␣␣␣␣␣InterpData(Interpcount,2)=ZuluTime;␣␣%␣␣(ZULU)
␣␣␣␣end
␣␣end
␣for␣j␣=␣1:nrows
␣␣␣␣if(data(j,3)␣==␣-1)
␣␣␣␣␣␣␣␣␣␣␣newZulu␣=␣round(interp1(InterpData(:,1),InterpData(:,2),data(j,2)),0);
␣␣␣␣␣␣␣␣␣␣␣data(j,3)␣=␣newZulu;
␣␣␣␣␣␣end
␣end
␣␣␣for␣k=1:length(data(:,1))
if(data(k,1)~=-1)
subset1(k,:)=data(k,:);
end
end
%%␣Young␣Set
clear␣Interpcount
clear␣InterpData
clear␣newZulu
Interpcount=0;
␣␣for␣i=1:nrows1
```

```
␣␣␣␣␣␣␣␣ZuluTime␣=␣data1(i,3);
␣␣␣␣␣␣␣␣time␣=␣data1(i,2);
␣␣␣␣if(ZuluTime~=-1)
␣␣␣␣␣␣␣␣Interpcount=Interpcount+1;
␣␣␣␣␣␣␣␣InterpData(Interpcount,1)=time;␣␣␣%␣Sensor␣board␣time
␣␣␣␣␣␣␣␣InterpData(Interpcount,2)=ZuluTime;␣␣%␣␣(ZULU)
␣␣␣␣end
␣␣end
␣for␣j␣=␣1:nrows1
␣␣␣␣if(data1(j,3)␣==␣-1)
␣␣␣␣␣␣␣␣␣␣␣newZulu␣=␣round(interp1(InterpData(:,1),InterpData(:,2),data1(j,2)),0);
␣␣␣␣␣␣␣␣␣␣␣data1(j,3)␣=␣newZulu;
␣␣␣␣␣␣end
␣␣␣end
```

Davis Processing Code

```
clear

clc

close␣all

%%if␣you␣want␣to␣use␣this␣as␣a␣function,␣uncomment␣and␣edit␣these␣lines

%function␣lavispiv

%pivrun(1,'B00500')

%return

%function␣pivrun(nur,run)

title_name␣=␣input('Please␣Enter␣The␣File␣Name:␣','s');

nmax=1;

for␣jj=1:nmax

path=''

run='001'

%run=int2str(run);

%datafile=strcat(path,run,'/',run,'.txt')

datafile=strcat(path,'B00',run,'.txt')

dx=0.025;␣%pixels/cm␣conversion

%

%␣Change␣for␣txt␣files␣nx␣is␣the␣#␣of␣cells␣in␣a␣cycle

%ny␣is␣#␣of␣cycles␣in␣first␣cell

nx=87;

ny=103;

%␣p1=zeros(nx,ny);

[dumx,dumy,dumu,dumv]=textread(datafile,'%n%n%n%n','headerlines',1);

k=1;

for␣i=1:nx
```

```
␣␣␣␣for␣j=1:ny
␣␣␣␣␣␣␣␣px(i,j)=dumx(k,1);
␣␣␣␣␣␣␣␣py(i,j)=dumy(k,1);
␣␣␣␣␣␣␣␣u(i,j)=dumu(k,1);
␣␣␣␣␣␣␣␣v(i,j)=dumv(k,1);
␣␣␣␣␣␣␣␣k=k+1;
␣␣␣␣end
end
%calculate␣velocities
%caclulate␣vorticity
vor=zeros(nx,ny);
vorc=zeros(nx,ny);
ddx=1;
for␣i=2:nx-1
␣␣␣␣for␣j=2:ny-1
␣␣␣␣␣␣␣␣vorc(i,j)=-(u(i,j+1)-u(i,j-1)-(v(i+1,j)-v(i-1,j)))/ddx;
␣␣␣␣␣␣␣␣vor1␣=␣u(i-1,j-1)+u(i,j-1)+u(i,j-1)+u(i+1,j-1);
vor2␣=␣u(i+1,j+1)+u(i,j+1)+u(i,j+1)+u(i-1,j+1);
vor3␣=␣v(i+1,j-1)+v(i+1,j)+v(i+1,j)+v(i+1,j+1);
vor4␣=␣v(i-1,j+1)+v(i-1,j)+v(i-1,j)+v(i-1,j-1);
vor(i,j)␣=␣(vor1␣-␣vor2␣+␣vor3␣-␣vor4)/(8.*ddx);
␣␣␣␣end
end
gamma_vor=0;␣gamma_vel=0;
%circulation␣via␣vorticity
gamma_vor=sum(sum(vor))*dx^2;
%circulation␣via␣velocity
```

```
for␣i=1:nx
␣␣␣␣gamma_vel=u(i,ny)+gamma_vel;
␣␣␣␣gamma_vel=-u(i,1)+gamma_vel;
end
for␣j=1:ny
␣␣␣␣gamma_vel=v(1,j)+gamma_vel;
␣␣␣␣gamma_vel=-v(nx,j)+gamma_vel;
end
gamma_vel=-gamma_vel*ddx;
gamma1(i)=gamma_vor;
gamma2(i)=gamma_vel;
x=px.*dx;
y=py.*dx;
mag=(u.^2+v.^2).^(0.5);
U_V_Vel=figure(1);
quiver(u,v,2),axis␣equal,axis␣ij%,axis([0␣30␣0␣20])
title(’U␣&␣V␣Velocities␣’);
xlabel(’U␣m/s’);
ylabel(’V␣m/s’);
%␣saveas(U_V_Vel,title_name+"U_V_Vel",’png’)
%␣saveas(U_V_Vel,title_name+"U_V_Vel",’fig’)
%Contour␣Velocity␣Magnitude
Vel_Mag=figure(2);
contourf(mag,50,’edgecolor’,’none’),axis␣equal,␣axis␣ij,shading␣interp
title(’Contour␣Velocity␣Magnitude␣’);
colorbar
%␣saveas(Vel_Mag,title_name+"Vel_Mag",’png’)
```

```
%␣saveas(Vel_Mag,title_name+"Vel_Mag",'fig')
%Vorticity
Vort=figure(3);
contourf(vor,50,'edgecolor','none'),axis␣equal,␣axis␣ij,shading␣interp
title(['Vorticity␣',␣title_name]);
xlabel('x␣distance'␣);
ylabel('y␣distance');
colorbar
caxis([-.2␣.25])
%␣saveas(Vort,title_name+"Vort",'png')
%␣saveas(Vort,title_name+"Vort",'fig')
%U␣Velocity␣Profile
U_Profile=figure(4);
plot(u(:,30))
hold␣on
plot(u(:,40))
plot(u(:,50))
plot(u(:,60))
hold␣off
title('U␣Velocity␣Profile␣');
ylabel('U␣m/s');
%␣saveas(U_Profile,title_name+"U_Profile",'png')
%␣saveas(U_Profile,title_name+"U_Profile",'fig')
%V␣Velocity␣Profile
V_Profile=figure(5);
plot(v(30,:))
hold␣on
```

```
plot(v(40,:))
plot(v(50,:))
plot(v(60,:))
hold␣off
title('V␣Velocity␣Profile'␣);
ylabel('V␣m/s');
%␣saveas(V_Profile,title_name+"V_Profile",'png')
%␣saveas(V_Profile,title_name+"V_Profile",'fig')
end
%Saving␣all␣the␣things
saveas(U_V_Vel,title_name+"U_V_Vel.png")
saveas(U_V_Vel,title_name+"U_V_Vel.fig")
saveas(Vel_Mag,title_name+"Vel_Mag.png")
saveas(Vel_Mag,title_name+"Vel_Mag.fig")
saveas(Vort,title_name+"Vort.png")
saveas(Vort,title_name+"Vort.fig")
saveas(U_Profile,title_name+"U_Profile.png")
saveas(U_Profile,title_name+"U_Profile.fig")
saveas(V_Profile,title_name+"V_Profile.png")
saveas(V_Profile,title_name+"V_Profile.fig")
␣save(title_name+".mat")
```

Flow-Field Velocity Code

```
clc
clear
close␣all
title_name␣=␣input('Please␣Enter␣The␣File␣Name:␣','s');
%title_name␣=␣input('Please␣Enter␣The␣File␣Name:␣','s');
files␣=␣uigetfile('*.*',␣␣'All␣Files␣(*.*)','MultiSelect','on');
%files␣=␣{'Dual␣Perp␣0␣Degree␣0ms␣Hub.mat','Dual␣Perp␣0␣Degree␣0ms␣Tip.mat','Dual␣Perp␣0
%S␣=␣load(files{1});
S␣=␣load(files{1},'u',␣'v');
for␣m␣=␣2:numel(files)
␣␣␣␣%S(m,1)␣=␣load(files{m});
␣␣␣␣S(m,1)␣=␣load(files{m},'u'␣,'v');
end
C␣=␣struct2cell(S)';
%Dual␣Perp␣Hub␣U
Hub_u␣=␣C(1,1);
Midplane_u␣=␣C(2,1);
Tip_u␣=␣C(3,1);
%Dual␣Perp␣Hub␣V
Hub_v␣=␣C(1,2);
Midplane_v␣=␣C(2,2);
Tip_v␣=␣C(3,2);
Hub_u␣=␣cell2mat(Hub_u);
Midplane_u␣=␣cell2mat(Midplane_u);
Tip_u␣=␣cell2mat(Tip_u);
Hub_v␣=␣cell2mat(Hub_v);
```

```
Midplane_v␣=␣cell2mat(Midplane_v);

Tip_v␣=␣cell2mat(Tip_v);
```

Anemomter Logger Code

```
//␣Code␣for␣Young␣81000␣or␣Trisonica␣Anemometer␣Data␣logging␣on␣TEENSY␣4.1
//Kyle␣Hickman␣kthickm@okstate.edu
//␣2_4_2021
/////////␣DO␣NOT␣EDIT␣BEYOND␣THIS␣POINT␣//////////
#define␣Pixhawk␣true␣//␣true␣for␣MavLink␣message␣parsing
#define␣Trisonica␣true␣//␣true␣if␣trisonica␣is␣the␣anemometer
#define␣Y92000␣false␣//␣true␣if␣y92000␣is␣the␣anemometer
//␣Standardized␣libraries␣for␣basic␣operation
#include␣<mavlink.h>␣␣//␣Allows␣for␣connection␣with␣Pixhawk-type␣autopilot
#include␣<TimeLib.h>␣␣//␣Required␣for␣datetime␣conversions
#include␣<SPI.h>␣␣␣␣␣␣//␣Required␣for␣all␣SD␣card␣operations␣of␣Teensy
//␣Check␣what␣version␣of␣Teensy␣is␣being␣used,␣and␣grab␣correpsonding␣library␣versions
#ifdef␣ARDUINO_TEENSY41
#include␣<Wire.h>␣␣//␣Teensy␣4.X-specific␣wire␣library
#include␣"SdFat-4.1.h"␣␣//␣Modified␣SdFat␣library␣for␣Teensy␣4.1
#include␣"sdios.h"␣␣␣␣␣␣//␣Extra␣file␣for␣SdFat
#include␣<Adafruit_ADS1015-4.1.h>␣␣//␣ADC␣library␣for␣tempAnemerature␣breakout␣boards,␣s
#define␣SD_CS_PIN␣=␣SS;␣␣//␣Built-in␣SD␣card␣pin
#define␣SD_CONFIG␣SdioConfig(FIFO_SDIO)␣␣//␣Set␣configuration␣type␣for␣SD␣setup
SdFat␣sd;␣␣//␣Define␣SD␣card␣variable␣name
File␣file;␣␣//␣Define␣file␣variable␣used␣to␣save␣data␣into␣the␣filename
#else
#include␣<Adafruit_ADS1015-3.6.h>␣␣//␣ADC␣library␣for␣tempAnemerature␣breakout␣boards,␣s
#include␣<i2c_t3.h>␣//␣I2C␣library␣for␣Teensy␣3.X␣boards
#include␣"SdFat-3.6.h"␣␣//␣Based␣SdFat␣library␣for␣Teensy␣3.X␣boards
#include␣"sdios.h"␣␣//␣Extra␣file␣for␣SdFat
```

```
SdFatSdio␣sd;␣␣//␣Define␣SD␣card␣variable␣name

SdFile␣file;␣␣//␣Define␣file␣variable␣used␣to␣save␣data␣into␣the␣filename

const␣uint8_t␣SD_CHIP_SELECT␣=␣SS;

#define␣SD_CS␣=␣BUILTIN_SDCARD;

#endif

char␣filename[12];␣//␣make␣it␣long␣enough␣to␣hold␣your␣longest␣file␣name,␣plus␣a␣null␣te

#if␣Pixhawk␣==␣true

#define␣HWSERIAL

#endif

//␣Anemometer

const␣byte␣numChars␣=␣450;

char␣from_Anemo[numChars];

boolean␣newData␣=␣false;

int␣prevTime␣=␣0;

int␣loopTime␣=␣0;

float␣oldPixTime␣=␣0;

uint32_t␣GPS_stat[1]␣=␣{0};

uint32_t␣PixTime[2]␣=␣{0,␣0};

elapsedMillis␣oldTime;

unsigned␣char␣i;

unsigned␣char␣j;

unsigned␣char␣k;

unsigned␣char␣s;

unsigned␣char␣e;

char␣tDspeed[6];

char␣wind_ang[6];

char␣wind_ele[6];
```

```
char␣SoS[6];
char␣tempAnem[5];
const␣int␣led␣=␣13;
uint16_t␣Year␣=␣0000;
uint8_t␣Month␣=␣00;
uint8_t␣Day␣=␣00;
uint8_t␣Hour␣=␣00;
uint8_t␣Minute␣=␣00;
uint8_t␣Second␣=␣00;
void␣setup()␣{
␣␣//␣put␣your␣setup␣code␣here,␣to␣run␣once:
␣␣Serial.begin(115200);
#if␣Pixhawk␣==␣true
␣␣Serial1.begin(115200);
#endif
#if␣Trisonica␣==␣true
␣␣Serial2.begin(115200,␣SERIAL_8N1);␣//␣Young␣81000␣signal␣will␣be␣on␣rx␣pin␣7␣(for␣TEEN
␣␣pinMode(led,␣OUTPUT);
#endif
#if␣Y92000␣==␣true
␣␣Serial2.begin(38400,␣SERIAL_8N1);␣//␣Young␣81000␣signal␣will␣be␣on␣rx␣pin␣7␣(for␣TEENS
␣␣pinMode(led,␣OUTPUT);
#endif
␣␣//␣Initialize␣at␣the␣highest␣speed␣supported␣by␣the␣board␣that␣is
␣␣//␣not␣over␣50␣MHz.␣Try␣a␣lower␣speed␣if␣SPI␣errors␣occur.
#ifdef␣ARDUINO_TEENSY41
␣␣if␣(!sd.begin(SdioConfig(FIFO_SDIO)))␣{
```

```
␣␣␣␣//␣don’t␣do␣anything␣more:
␣␣␣␣while␣(1)␣{
␣␣␣␣␣␣digitalWrite(led,␣!digitalRead(led));
␣␣␣␣␣␣Serial.println("Teensy␣4.1␣SD␣fail.␣Reset␣card␣and␣try␣again.");
␣␣␣␣␣␣delay(2000);
␣␣␣␣}
␣␣}
#else
␣␣if␣(!sd.begin())␣{
␣␣␣␣//␣don’t␣do␣anything␣more:
␣␣␣␣while␣(1)␣{
␣␣␣␣␣␣Serial.println("Teensy␣3.6␣SD␣fail.␣Reset␣card␣and␣try␣again.");
␣␣␣␣␣␣digitalWrite(led,␣!digitalRead(led));
␣␣␣␣␣␣delay(2000);
␣␣␣␣}
␣␣}
#endif
#if␣Pixhawk␣==␣true
␣␣oldTime␣=␣0;
␣␣while␣(GPS_stat[0]␣<␣3)␣{
␣␣␣␣Serial.println("Waiting␣for␣GPS␣lock");
␣␣␣␣GPS_receive();
␣␣␣␣if␣(oldTime␣>=␣1000)␣{
␣␣␣␣␣␣digitalWrite(led,␣!digitalRead(led));
␣␣␣␣␣␣oldTime␣=␣oldTime␣-␣1000;
␣␣␣␣}
␣␣}
```

```
␣␣oldTime␣=␣0;
␣␣while␣(PixTime[0]␣<␣5)␣{
␣␣␣␣Serial.println("Waiting␣for␣time␣sync");
␣␣␣␣MavLink_receive();
␣␣␣␣if␣(oldTime␣>=␣500)␣{
␣␣␣␣␣␣digitalWrite(led,␣!digitalRead(led));
␣␣␣␣␣␣oldTime␣=␣oldTime␣-␣500;
␣␣␣␣}
␣␣␣␣delay(10);
␣␣}
␣␣delay(2000);
␣␣MavLink_receive();
#endif
␣␣int␣n␣=␣0;
␣␣snprintf(filename,␣sizeof(filename),␣"WTUN%03d.csv",␣n);␣//␣includes␣a␣three-digit␣seq
␣␣while␣(sd.exists(filename))␣{
␣␣␣␣n++;
␣␣␣␣snprintf(filename,␣sizeof(filename),␣"WTUN%03d.csv",␣n);
␣␣}
␣␣if␣(Serial)␣{
␣␣␣␣Serial.println(n);
␣␣␣␣Serial.println(filename);
␣␣}
␣␣Year␣=␣2001;
␣␣Month␣=␣01;
␣␣Day␣=␣01;
␣␣Hour␣=␣01;
```

```
␣␣Minute␣=␣01;
␣␣Second␣=␣01;

␣␣//␣set␣creation␣date␣time
␣␣//␣␣if␣(!file.timestamp(T_CREATE,␣Year,␣Month,␣Day,␣Hour,␣Minute,␣Second))␣{
␣␣//␣␣␣␣if␣(Serial)␣{
␣␣//␣␣␣␣␣␣Serial.println("Error␣creating␣timestamp");
␣␣//␣␣␣␣}
␣␣//␣␣␣␣while␣(1)␣{
␣␣//␣␣␣␣␣␣digitalWrite(led,␣!digitalRead(led));
␣␣//␣␣␣␣␣␣delay(2000);
␣␣//␣␣␣␣}
␣␣//␣␣}
␣␣//␣␣//␣set␣write/modification␣date␣time
␣␣//␣␣if␣(!file.timestamp(T_WRITE,␣Year,␣Month,␣Day,␣Hour,␣Minute,␣Second))␣{
␣␣//␣␣␣␣if␣(Serial)␣{
␣␣//␣␣␣␣␣␣Serial.println("Error␣writing␣timestamp");
␣␣//␣␣␣␣}
␣␣//␣␣␣␣while␣(1)␣{
␣␣//␣␣␣␣␣␣digitalWrite(led,␣!digitalRead(led));
␣␣//␣␣␣␣␣␣delay(2000);
␣␣//␣␣␣␣}
␣␣//␣␣}
␣␣//␣␣//␣set␣access␣date
␣␣//␣␣if␣(!file.timestamp(T_ACCESS,␣Year,␣Month,␣Day,␣Hour,␣Minute,␣Second))␣{
␣␣//␣␣␣␣if␣(Serial)␣{
␣␣//␣␣␣␣␣␣Serial.println("Error␣setting␣access␣timestamp");
```

```
␣␣//␣␣␣␣}
␣␣//␣␣␣␣while␣(1)␣{
␣␣//␣␣␣␣␣␣digitalWrite(led,␣!digitalRead(led));
␣␣//␣␣␣␣␣␣delay(2000);
␣␣//␣␣␣␣}
␣␣//␣␣}
␣␣if␣(Serial)␣{
␣␣␣␣Serial.println("File␣written␣successfully");
␣␣}
␣␣file.close();
␣␣delay(50);
␣␣file.open(filename,␣FILE_WRITE);
␣␣file.println("Board␣Time␣(ms),␣Anemometer␣Data,␣Unix␣Time␣(sec),␣Pix␣Boot␣Time␣(ms)");
␣␣file.close();
␣␣delay(1000);
}
void␣loop()␣{
␣␣file.open(filename,␣FILE_WRITE);
␣␣digitalWrite(led,␣!digitalRead(led));
␣␣loopTime␣=␣millis();
␣␣file.print(loopTime␣+␣String(’,’));
␣␣if␣((loopTime␣-␣prevTime)␣>␣1000)␣{
␣␣␣␣digitalWrite(led,␣!digitalRead(led));
␣␣␣␣Serial.println(loopTime);
␣␣␣␣prevTime␣=␣loopTime;
␣␣}
␣␣static␣boolean␣recvInProgress␣=␣false;
```

```
␣␣static␣byte␣index␣=␣0;
␣␣char␣startMarker␣=␣(char)83;
␣␣char␣endMarker␣=␣(char)13;
␣␣newData␣=␣false;
␣␣char␣rc;
␣␣while␣(Serial2.available()␣>␣0␣&&␣newData␣==␣false)
␣␣{
␣␣␣␣rc␣=␣Serial2.read();
␣␣␣␣if␣(recvInProgress␣==␣true)
␣␣␣␣{
␣␣␣␣␣␣if␣(rc␣!=␣endMarker␣&&␣rc␣!=␣’\0’)
␣␣␣␣␣␣{
␣␣␣␣␣␣␣␣from_Anemo[index]␣=␣rc;
␣␣␣␣␣␣␣␣index++;
␣␣␣␣␣␣␣␣if␣(index␣>=␣numChars)
␣␣␣␣␣␣␣␣{
␣␣␣␣␣␣␣␣␣␣index␣=␣numChars␣-␣1;
␣␣␣␣␣␣␣␣}
␣␣␣␣␣␣}
␣␣␣␣␣␣else␣if␣(rc␣==␣endMarker)
␣␣␣␣␣␣{
␣␣␣␣␣␣␣␣if(index<numChars)
␣␣␣␣␣␣␣␣{
␣␣␣␣␣␣␣␣␣␣for␣(i=index;␣i<numChars;␣i++){
␣␣␣␣␣␣␣␣␣␣␣␣from_Anemo[i]␣=␣(char)0;
␣␣␣␣␣␣␣␣␣␣}
␣␣␣␣␣␣␣␣␣␣index␣=␣i;
```

```
␣␣␣␣␣␣␣␣}
␣␣␣␣␣␣␣␣from_Anemo[index]␣=␣’\0’;␣//␣terminate␣the␣string
␣␣␣␣␣␣␣␣recvInProgress␣=␣false;

␣␣␣␣␣␣␣␣index␣=␣0;
␣␣␣␣␣␣␣␣newData␣=␣true;
␣␣␣␣␣␣}
␣␣␣␣}
␣␣␣␣else␣if␣(rc␣==␣startMarker)
␣␣␣␣{
␣␣␣␣␣␣recvInProgress␣=␣true;
␣␣␣␣}
␣␣}
␣␣if␣(newData␣==␣true)
␣␣{
␣␣␣␣i␣=␣0;
␣␣␣␣j␣=␣0;
␣␣␣␣s␣=␣0;
␣␣␣␣k␣=␣0;
␣␣␣␣e␣=␣0;
␣␣␣␣newData␣=␣false;
␣␣␣␣Serial.print("from_Anemo:␣");
␣␣␣␣Serial.println(from_Anemo);
//␣␣␣␣for␣(int␣i␣=␣0;␣i␣<␣sizeof(from_Anemo)␣-␣1;␣i++)
//␣␣␣␣{
//␣␣␣␣␣␣if␣(i␣==␣0)
//␣␣␣␣␣␣{
```

```
//␣␣␣␣␣␣␣␣for␣(␣int␣j=0;␣j<sizeof(tDspeed);␣j++){
//␣␣␣␣␣␣␣␣tDspeed[j]␣=␣from_Anemo[j+i];
//␣␣␣␣␣␣␣␣}
//␣␣␣␣␣␣}
//␣␣␣␣␣␣if␣(i␣==␣8){
//␣␣␣␣␣␣␣␣for␣(␣int␣j=0;␣j<sizeof(wind_ang);␣j++){
//␣␣␣␣␣␣␣␣wind_ang[j]␣=␣from_Anemo[j+i];
//␣␣␣␣␣␣␣␣}
//␣␣␣␣␣␣}
//␣␣␣␣␣␣if␣(i␣==␣13){
//␣␣␣␣␣␣␣␣for␣(␣int␣j=0;␣j<sizeof(wind_ele);␣j++){
//␣␣␣␣␣␣␣␣wind_ele[j]␣=␣from_Anemo[j+i];
//␣␣␣␣␣␣␣␣}
//␣␣␣␣␣␣}
//␣␣␣␣␣␣if␣(i␣==␣19){
//␣␣␣␣␣␣␣␣for␣(␣int␣j=0;␣j<sizeof(SoS);␣j++){
//␣␣␣␣␣␣␣␣SoS[j]␣=␣from_Anemo[j+i];
//␣␣␣␣␣␣␣␣}
//␣␣␣␣␣␣}
//␣␣␣␣␣␣if␣(i␣==␣26){
//␣␣␣␣␣␣␣␣for␣(␣int␣j=0;␣j<sizeof(tempAnem)-1;␣j++){
//␣␣␣␣␣␣␣␣tempAnem[j]␣=␣from_Anemo[j+i];
//␣␣␣␣␣␣␣␣if␣(j␣==␣sizeof(tempAnem)){
//␣␣␣␣␣␣␣␣␣␣tempAnem[j]␣=␣'\0';
//␣␣␣␣␣␣␣␣␣␣break;
//␣␣␣␣␣␣␣␣}
//␣␣␣␣␣␣␣␣}
```

```
//␣␣␣␣␣␣}
//
//␣␣␣␣Serial.print(String("␣|␣"));
//␣␣␣␣Serial.print(String("Wind␣Speed:␣")␣+␣tDspeed␣+␣String("␣|␣"));
//␣␣␣␣Serial.print(String("Angle:␣")␣+␣wind_ang␣+␣String("␣|␣"));
//␣␣␣␣Serial.print(String("elevation:␣␣")␣+␣wind_ele␣+␣String("␣|␣"));
//␣␣␣␣Serial.print(String("Speed␣of␣Sound:␣")␣+␣SoS␣+␣String("␣|␣"));
//␣␣␣␣Serial.println(String("tempAnemerature:␣"␣)␣+␣tempAnem␣+␣String("␣|␣"));

␣␣␣␣file.print(from_Anemo␣+␣String(’,’));
␣␣␣␣}
␣␣else␣{
␣␣␣␣file.print(String(’␣’)␣+␣String(’,’));
␣␣}

#if␣Pixhawk␣==␣true
␣␣MavLink_receive();

␣␣if␣(PixTime[1]␣>␣oldPixTime)␣{
␣␣␣␣file.print(PixTime[0]);
␣␣␣␣file.print(’,’);
␣␣␣␣file.print(PixTime[1]);
␣␣␣␣file.print(’,’);
␣␣␣␣oldPixTime␣=␣PixTime[1];
␣␣}
␣␣else␣{
␣␣␣␣file.print((String)’␣’␣+␣’,’␣+␣’␣’␣+␣’,’);
```

```
␣␣}

#else
␣␣file.print((String)'␣'␣+␣','␣+␣'␣'␣+␣',');
#endif

␣␣file.println();
␣␣file.close();

}

//function␣called␣by␣arduino␣to␣read␣any␣MAVlink␣messages␣sent␣by␣serial␣communication␣f
uint32_t*␣GPS_receive()
{
␣␣mavlink_message_t␣msg;
␣␣mavlink_status_t␣status;

␣␣while␣(Serial1.available())
␣␣{
␣␣␣␣uint8_t␣c␣=␣Serial1.read();

␣␣␣␣//Get␣new␣message
␣␣␣␣if␣(mavlink_parse_char(MAVLINK_COMM_0,␣c,␣&msg,␣&status))
␣␣␣␣{

␣␣␣␣␣␣//Handle␣new␣message␣from␣autopilot
␣␣␣␣␣␣switch␣(msg.msgid)
```

```
␣␣␣␣␣␣{

␣␣␣␣␣␣␣␣case␣MAVLINK_MSG_ID_GPS_RAW_INT:␣␣//␣#27:␣RAW_IMU
␣␣␣␣␣␣␣␣␣␣{
␣␣␣␣␣␣␣␣␣␣␣␣/*␣Message␣decoding:␣PRIMITIVE
␣␣␣␣␣␣␣␣␣␣␣␣␣␣␣␣␣␣static␣inline␣void␣mavlink_msg_raw_imu_decode(const␣mavlink_message_t*
␣␣␣␣␣␣␣␣␣␣␣␣*/
␣␣␣␣␣␣␣␣␣␣␣␣mavlink_gps_raw_int_t␣gps_raw_int;
␣␣␣␣␣␣␣␣␣␣␣␣mavlink_msg_gps_raw_int_decode(&msg,␣&gps_raw_int);

␣␣␣␣␣␣␣␣␣␣␣␣GPS_stat[0]␣=␣gps_raw_int.fix_type;

␣␣␣␣␣␣␣␣␣␣␣␣return␣GPS_stat;



␣␣␣␣␣␣␣␣␣␣}
␣␣␣␣␣␣␣␣␣␣break;
␣␣␣␣␣␣}
␣␣␣␣}
␣␣}
}

//function␣called␣by␣arduino␣to␣read␣any␣MAVlink␣messages␣sent␣by␣serial␣communication␣f
uint32_t*␣MavLink_receive()
{
␣␣mavlink_message_t␣msg;
␣␣mavlink_status_t␣status;
```

```
␣␣while␣(Serial1.available())
␣␣{
␣␣␣␣uint8_t␣c␣=␣Serial1.read();

␣␣␣␣//Get␣new␣message
␣␣␣␣if␣(mavlink_parse_char(MAVLINK_COMM_0,␣c,␣&msg,␣&status))
␣␣␣␣{

␣␣␣␣␣␣//Handle␣new␣message␣from␣autopilot
␣␣␣␣␣␣switch␣(msg.msgid)
␣␣␣␣␣␣{

␣␣␣␣␣␣␣␣case␣MAVLINK_MSG_ID_SYSTEM_TIME:␣␣//␣#27:␣RAW_IMU
␣␣␣␣␣␣␣␣␣␣{
␣␣␣␣␣␣␣␣␣␣␣␣/*␣Message␣decoding:␣PRIMITIVE
␣␣␣␣␣␣␣␣␣␣␣␣␣␣␣␣␣␣static␣inline␣void␣mavlink_msg_raw_imu_decode(const␣mavlink_message_t*
␣␣␣␣␣␣␣␣␣␣␣␣*/
␣␣␣␣␣␣␣␣␣␣␣␣mavlink_system_time_t␣system_time;
␣␣␣␣␣␣␣␣␣␣␣␣mavlink_msg_system_time_decode(&msg,␣&system_time);

␣␣␣␣␣␣␣␣␣␣␣␣uint64_t␣Ptime␣=␣system_time.time_unix_usec;
␣␣␣␣␣␣␣␣␣␣␣␣PixTime[0]␣=␣Ptime␣/␣1000000;
␣␣␣␣␣␣␣␣␣␣␣␣PixTime[1]␣=␣system_time.time_boot_ms;

␣␣␣␣␣␣␣␣␣␣␣␣return␣PixTime;
```

```
␣␣␣␣␣␣␣␣␣␣}
␣␣␣␣␣␣␣␣␣␣break;
␣␣␣␣␣␣}
␣␣␣␣}
␣␣}
}
```

Correlation Coefficient

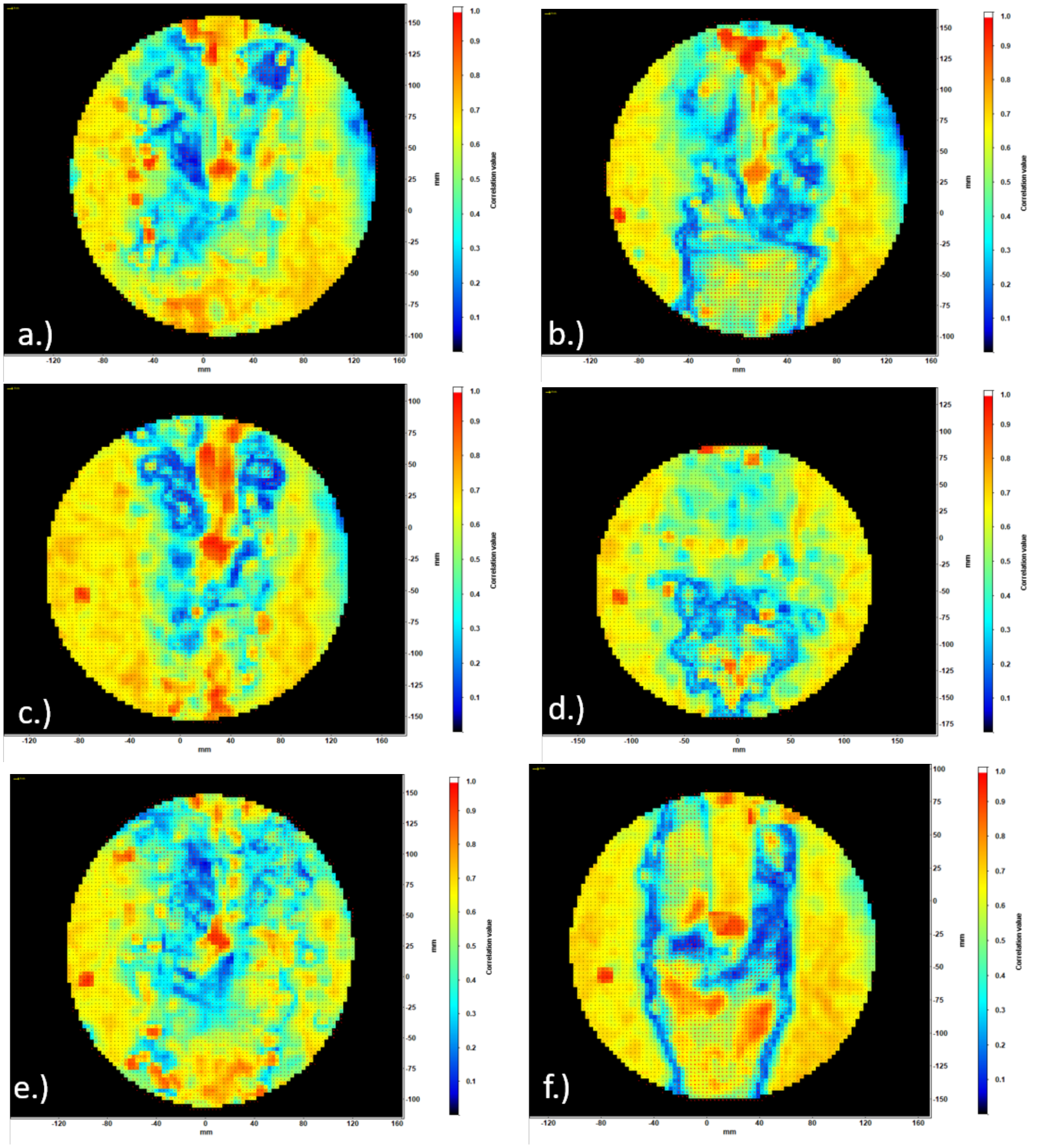

Figure 125: Correlation Coefficient Dual Perp Mid-plane: a.) (0m/s, 0°), b.) (0.5m/s, 0°), c.) (0m/s, 15°), d.) (0.5m/s, 15°), e.) (0m/s, 30°), f.) (0.5m/s, 30°)

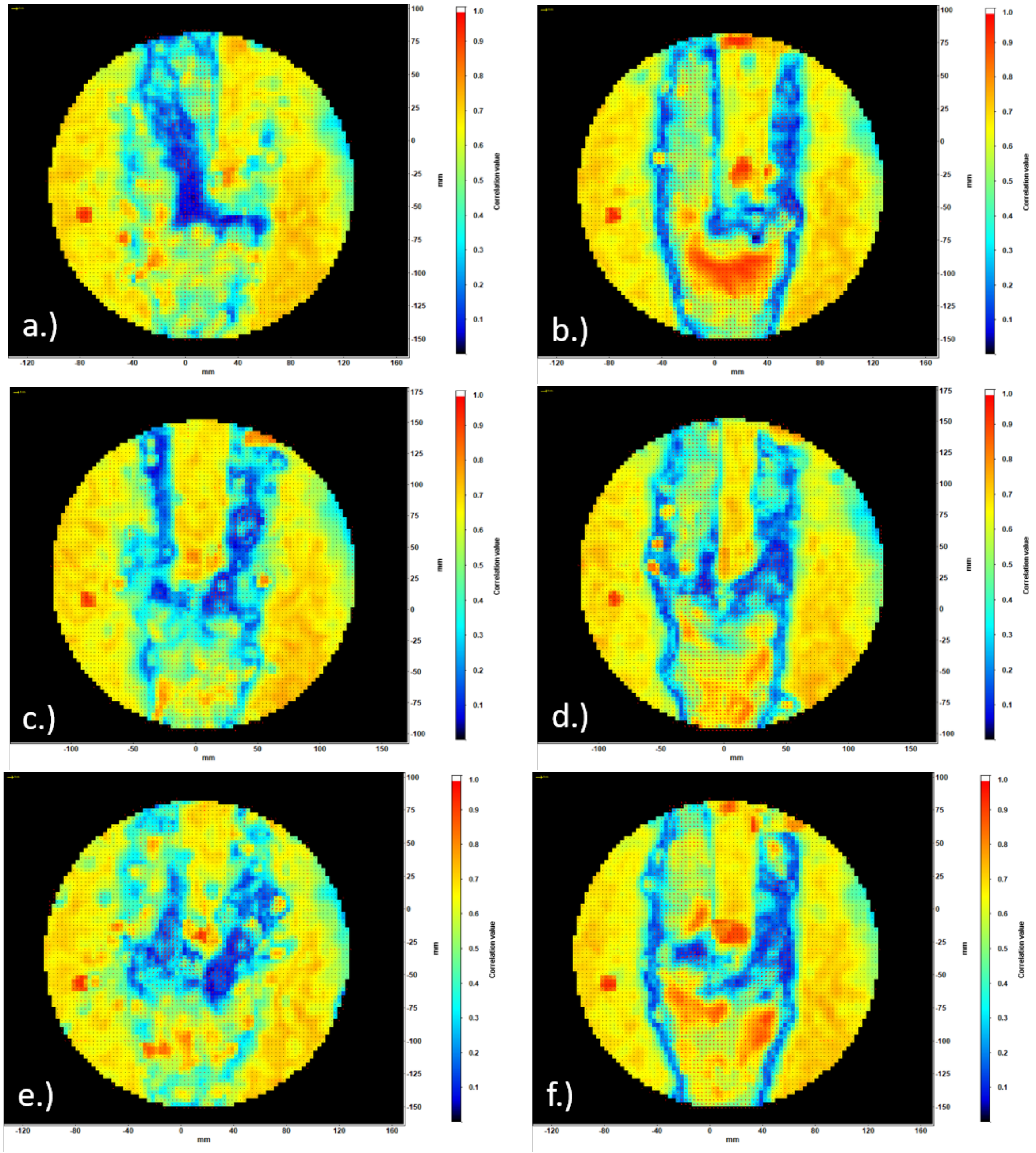

Figure 126: Correlation Coefficient Dual Perp Hub: a.) (0m/s, 0°), b.) (0.5m/s, 0°), c.) (0m/s, 15°), d.) (0.5m/s, 15°), e.) (0m/s, 30°), f.) (0.5m/s, 30°)

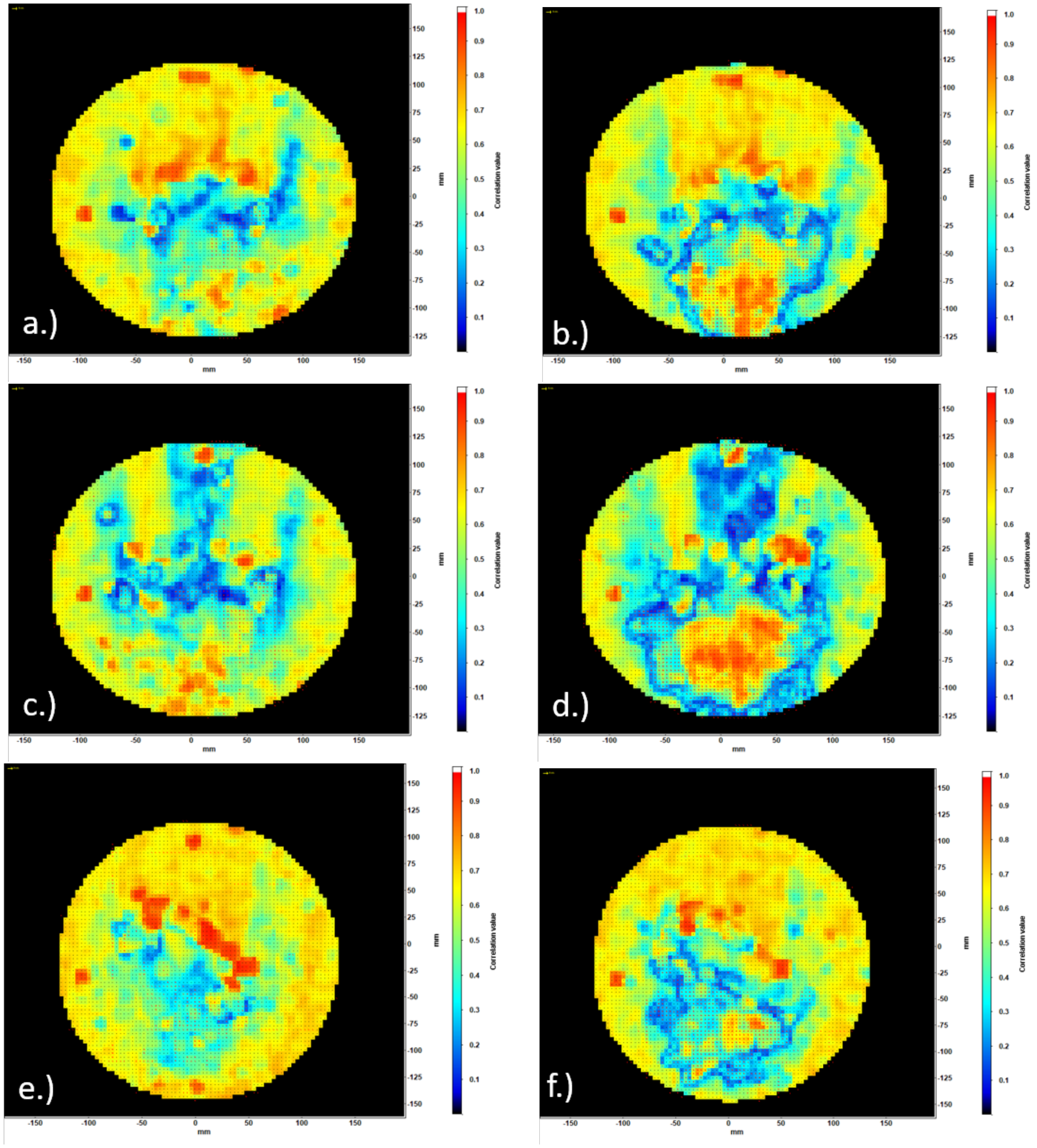

Figure 127: Correlation Coefficient Dual Para Hub: a.) (0m/s, 0°), b.) (0.5m/s, 0°), c.) (0m/s, 15°), d.) (0.5m/s, 15°), e.) (0m/s, 30°), f.) (0.5m/s, 30°)

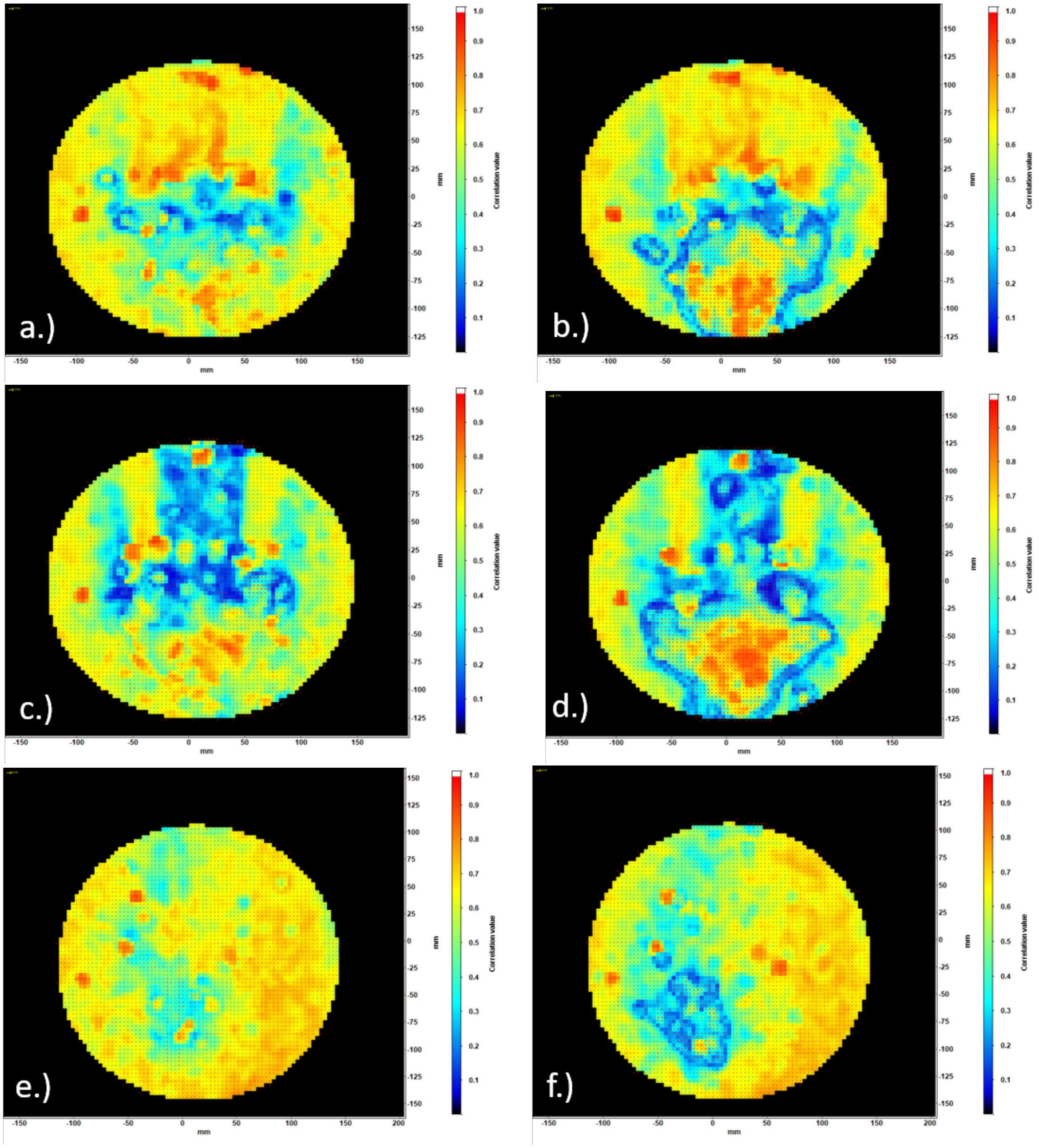

Figure 128: Correlation Coefficient Dual Para Tip: a.) (0m/s, 0°), b.) (0.5m/s, 0°), c.) (0m/s, 15°), d.) (0.5m/s, 15°), e.) (0m/s, 30°), f.) (0.5m/s, 30°)

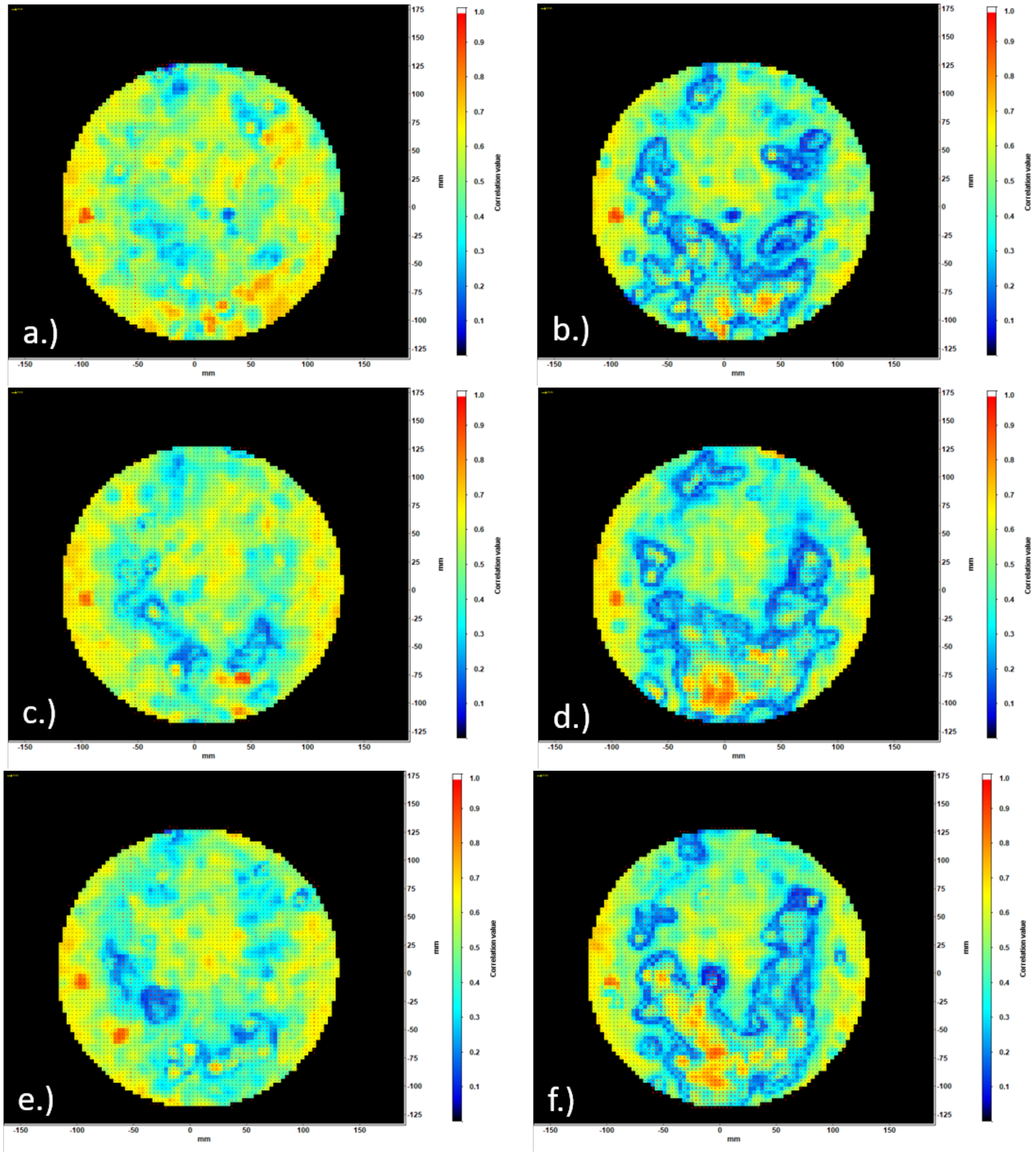

Figure 129: Correlation Coefficient Quad Plus Tip: a.) (0m/s, 0°), b.) (0.5m/s, 0°), c.) (0m/s, 15°), d.) (0.5m/s, 15°), e.) (0m/s, 30°), f.) (0.5m/s, 30°)

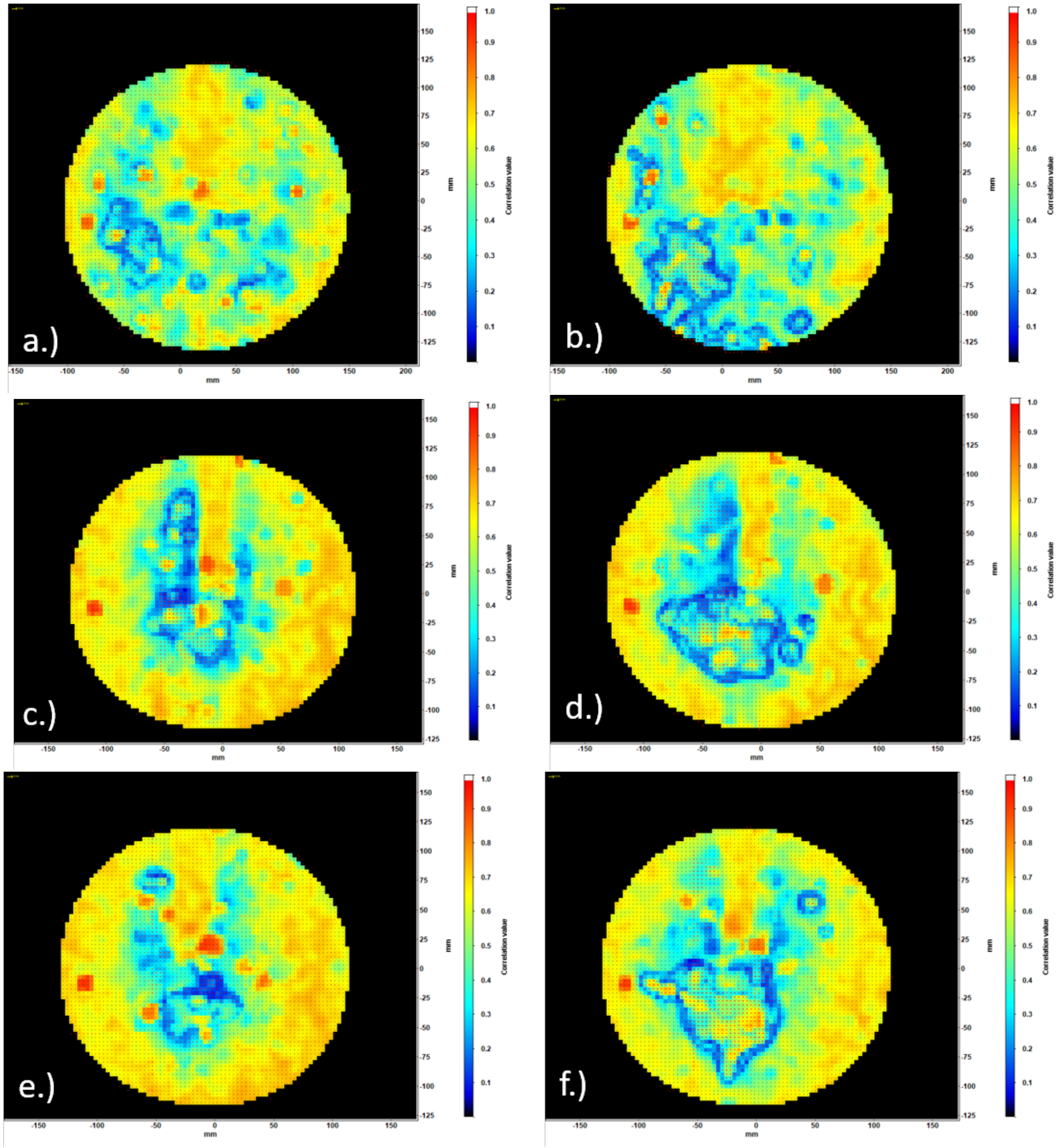

Figure 130: Correlation Coefficient Quad Plus Hub: a.) (0m/s, 0°), b.) (0.5m/s, 0°), c.) (0m/s, 15°), d.) (0.5m/s, 15°), e.) (0m/s, 30°), f.) (0.5m/s, 30°)

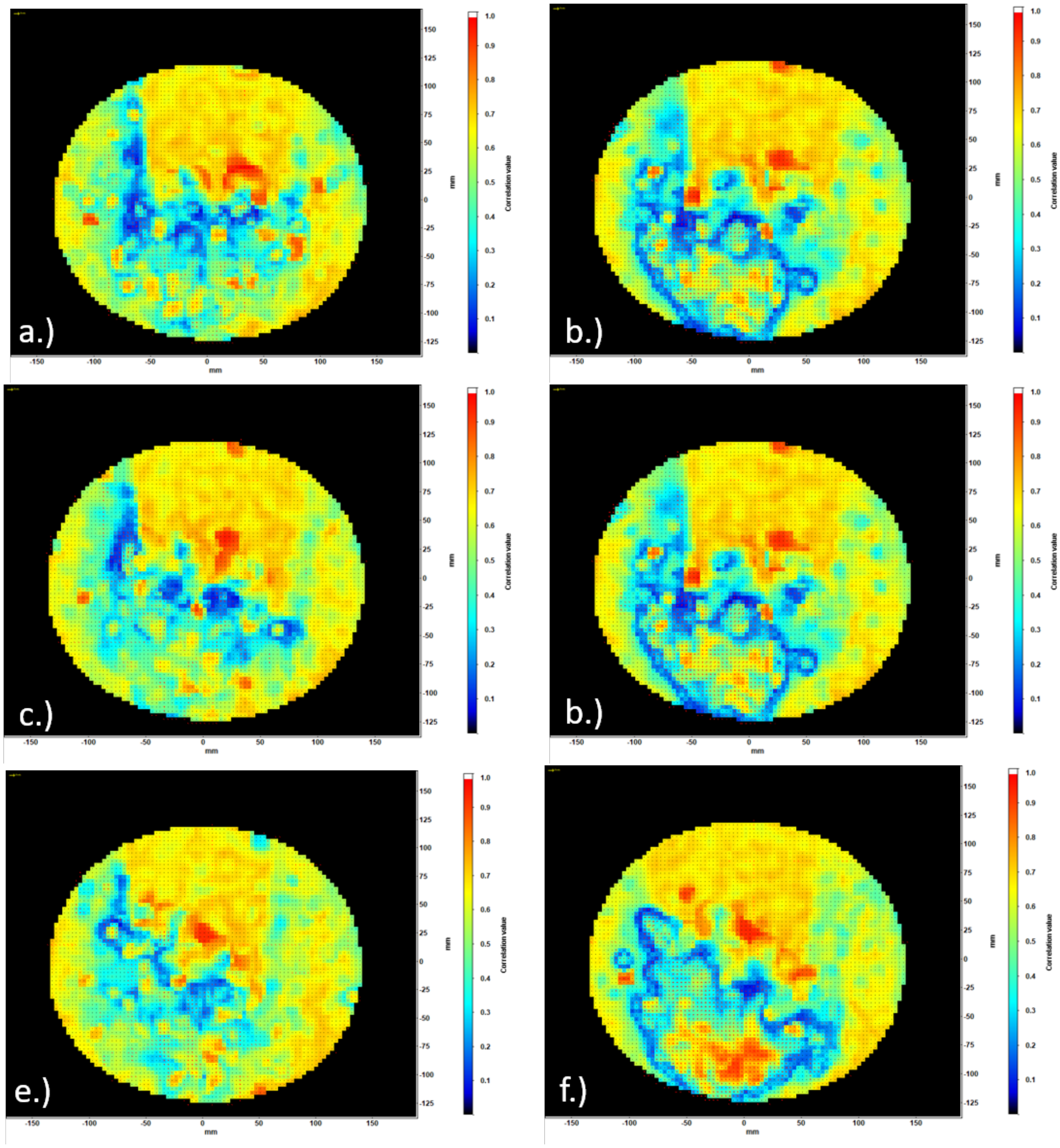

Figure 131: Correlation Coefficient Quad Plus Mid-plane: a.) (0m/s, 0°), b.) (0.5m/s, 0°), c.) (0m/s, 15°), d.) (0.5m/s, 15°), e.) (0m/s, 30°), f.) (0.5m/s, 30°)

VITA

James Brenner

Candidate for the Degree of

Master of Science

Thesis: INFLOW ANALYSIS FOR MULTI-ROTORS AND THE IMPACT ON SENSOR PLACEMENT

Major Field: Mechanical and Aerospace Engineering

Biographical:

Education:

Completed the requirements for the Master of Science in Mechanical and Aerospace Engineering at Oklahoma State University, Stillwater, Oklahoma in July, 2021.

Completed the requirements for the Bachelor of Science in Aerospace Engineering at Oklahoma State University, Stillwater, Oklahoma in 2019.

Completed the requirements for the Bachelor of Science in Mechanical Engineering at Oklahoma State University, Stillwater, Oklahoma in 2019.

Professional Memberships:

American Model Association, American Institute of Aeronautics and Astronautics, American Physical Society